Department of Precision and Microsystems Engineering

Active metamaterials: unit cells for tunable damping

D.D.Thomas

Report no : 2020.048
Coach : Dr.ir.A.Hunt
Professor : Dr.ir.H.HosseinNia
Specialisation : Mechatronic System Design
Type of report : Master of Science Thesis
Date : 30-10-2020

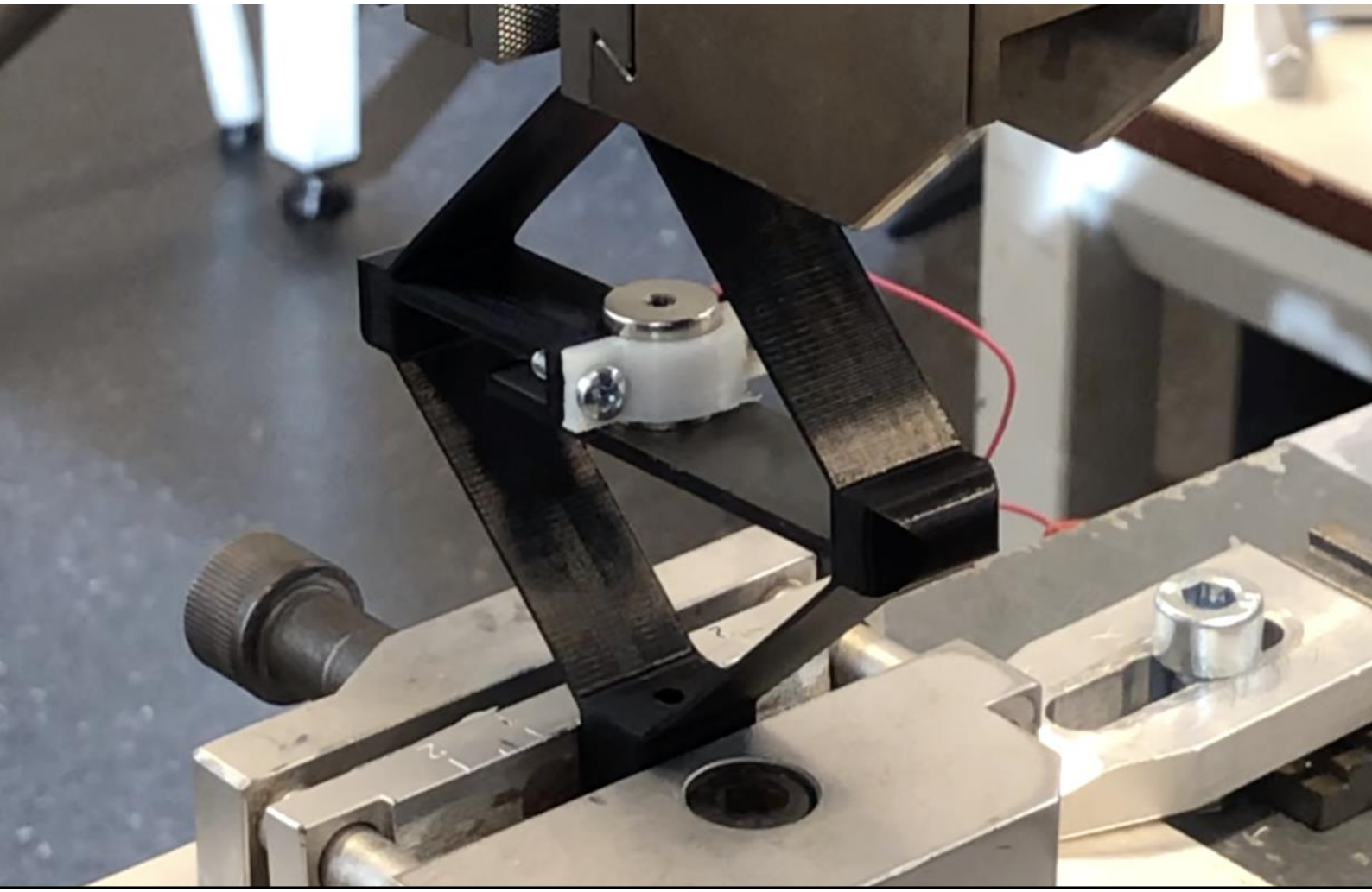

TU Delft Delft University of Technology

Challenge the future

Active metamaterials: unit cells for tunable damping

by

D.D. Thomas

to obtain the degree of Master of Science

at the Delft University of Technology,

to be defended publicly on Monday November 16, 2020 at 10:45 AM.

Student number:	4236068	
Project duration:	November 1, 2019 – November 16, 2020	
Thesis committee:	Dr. ir. A. Hunt,	TU Delft, daily supervisor
	Dr. ir. H. HosseinNia,	TU Delft, supervisor
	Dr. ir. M. Tichem,	TU Delft

TU Delft

Preface

From the start of primary school, I had an affinity with mechanics and the stunning K'nex toys could keep me occupied for days. Thereafter, during secondary school I was always fascinated by engineering and could not wait till the next issue of Kijk dropped on the doormat. Also, I joined a group created by my physics teacher and we fabricated our own laser-tag game, including a variety of self-made laser-guns and corresponding suits. This inspired me greatly to start my study mechanical engineering at the TU Delft. My expectations were met from the start and I was impressed by the variety of topics and the many hands-on experiences during the years. I feel very privileged to have received this excellent opportunity of learning and discovering the wonderful world of engineering. Now, the finish is coming close and I am thrilled having been involved in a fascinating and challenging research thesis on metamaterials.

This project would not be possible without the help of people close to me and therefore I would like to thank them with all my heart. First of all, I would like to thank Andres Hunt and Hassan HosseinNia for their outstanding guidance during the project. Especially I am grateful to Andres Hunt for his untiring daily supervision. Without his sharp feedbacks, stimulating discussions and literally always-positive approach I would not have made it.

I like to thank my father for this wonderful support. At times he became my tutor when sharing his own experience in overcoming complicated projects. Above all, his loving care will always be warmly remembered.

I like to mention my grandpa who often was my cheerful guide in sharing academic insights and experience. He volunteered to be my thesis editor and did so with professional dedication and enthusiasm.

Lastly, I would also like to express my appreciation to everybody else that contributed to my thesis and my great time as a student in Delft.

D.D. Thomas
Amsterdam, November 2020

Abstract

Mechanical metamaterials belong to the family of metamaterials. The concept of a metamaterial has been extended from electromagnetics and acoustics to the field of mechanics. Metamaterials have their material properties related to the unit cell structure instead of the composition. Therefore, artificial metamaterial structures can achieve exotic properties. Metamaterials are constrained in that the mechanical properties are precisely defined and fixed; alteration between these mentioned properties simply is not feasible. However, when activated, metamaterials can be controlled and mechanical properties can be influenced.

In this work, the current state of subcentimeter-scale electromagnetic actuators and miniaturisation efforts is reviewed. And further, a novel active metamaterial unit cell design for controlled damping is introduced. Centimeter-scale electromagnetic actuators are integrated as activators in an elastic mechanical metamaterial structure. Tuning of the integrated electromagnets allows ranging material damping from near-perfect elastic till damped behaviour.

In order to benefit from their adequate properties when scaled in centimeter-scale region an analysis regarding scaling effects in electromagnetic actuators has been conducted. The actuators are described in terms of design parameters that are associated with the practical materials. A scaling factor then is substituted in their configuration. Identifying scaling effects in the smaller scale region has given insights in actuator comparison and performance.

The core of this work will investigate an active metamaterial unit cell design that effectively exploits the way in which the reluctance actuator functions in order to create Coulomb damping. For that purpose a unit cell design has been developed that possesses the required metamaterial stiffness profile as well as damping capabilities. Then, a proof-of-principle unit cell demonstrator of 90mm and 45mm in length, have been made.

First the individual behaviour of the passive lattice structure and electromagnetic actuators have been studied with quasi-static deformations. Thereafter, the electrically controlled damping behaviour of the active unit cell has been validated for cyclic loading deformations of $2.5 - 5$mm.

The results of the force-displacement curve of the 90mm unit cell indicate that for a friction force F_r of 0.59N the dissipated energy is 1.2e-2J. The 45mm unit cell can achieve up to 4.1e-3J of damping for a friction force of 0.27N. Consequently, the damping ratio, which equals damped over stored energy, results in a damping range from 3% and 20% up to 34% and 132% respectively.

Contents

1

Introduction

1.1. Motivation

The interdisciplinary field of metamaterials consists of material engineered in such a way to have a property that is not found in conventional materials. Metamaterials derive their properties not from the properties of the composite, but from their artificial meso-scale geometry as well as from their unit cell structure. Their tailored shape, geometry, volume, orientation and arrangement give them properties to achieve benefits that exceed what is possible with conventional materials. Potential applications of metamaterials are boundless and contrary to conventional material, the response to electric and magnetic fields, or to sonic waves is determined by their structure. This, therefore, affects them in a way that cannot be observed in conventional (bulk) material. The concept of a metamaterial has been extended towards the field of mechanics. These mechanical metamaterials use different parameters to achieve tailored properties in materials that are not based on sound waves or electromagnetic waves. Such as negative Poisson's ratio, negative compressibility or vanishing shear. The greatest limitation of metamaterials is that their mechanical properties are precisely defined and fixed; alteration simply is not feasible. However, when extended to active metamaterials, they can be controlled and mechanical properties can be influenced additionally. Active metamaterials with properties like tunable damping, flexible stiffness as well as lightweight structures do enable a host of novel applications. High-tech, automotive and aerospace industries could greatly benefit from tunable mechanical properties in applications. Since mechanical metamaterials play a central role in this research project, a brief introduction to that concept is presented.

1.2. Background

In order to understand how mechanical metamaterials differ from conventional materials, we need to look into the typical mechanical properties of bulk materials. The material properties, stiffness, rigidity and compressibility are important to define the resistance of deflection of a metamaterial. The material properties of these structures correspond to the four elastic constants [10]. When an elastic mechanical metamaterial structure is subjected to stress a proportionate amount of strain will be produced. The ratio of it is known as the elastic constant and represents the elastic behaviour of a structure and therefore also defines a metamaterial structure. The four elastic constants consist of the Poisson's ratio ν, and three constants that describe the stiffness, rigidity and compressibility of a structural component called Young's modulus E, bulk modulus K and shear modulus G.

The Young's modulus E is the constant ratio of applied (uni-axial) stress σ to strain ϵ that is subjected to a material structure according to Hooke's law. When tensile stress or compressive stress is applied, this is directly proportional to the strain within the elastic boundaries of the structure. This behaviour is illustrated in C of figure 1.1 and can be defined as:

$$E = \frac{\sigma}{\epsilon} \tag{1.1}$$

The bulk modulus K is related to volume change and is the constant ratio of mutually applied stresses dP over the volumetric strain dV with an initial volume V_0. It, therefore, is also a measurement about the resistance of that object to compression, as can be seen in C of figure 1.1 and its equation is presented as:

$$K = -V_0 \frac{dP}{dV} \tag{1.2}$$

The shear modulus G, also called the rigidity modulus, describes the material response to the shear stress τ, as can be seen in figure 1.1. The material response is a change of the structure given with shear strain γ. The corresponding ratio is given as:

$$G = \frac{\tau}{\gamma} \tag{1.3}$$

The Poisson's ratio ν is defined as the ratio of the lateral contractile strain $d_{\epsilon y}$ in the y-direction to the longitudinal tensile strain $d_{\eta x}$ in the x-direction for a tension that is applied along the longitudinal axis of the material structure [2] and can be seen as:

$$\nu = \frac{d_{\epsilon y}}{d_{\eta x}} \tag{1.4}$$

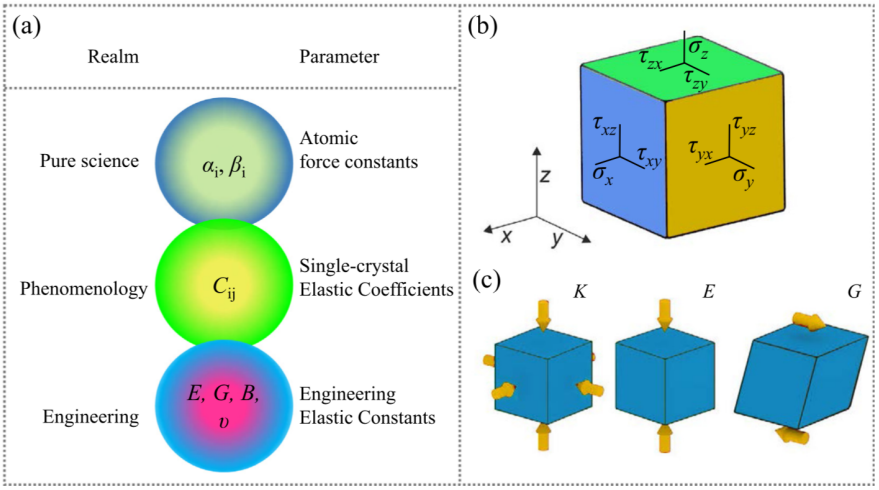

Figure 1.1: (A) Schematic interconnectivity of elastic parameters of solids (B) Scheme of an elemental elastic body (C) Schemes of measuring the bulk modulus K (left), the Young's modulus E (middle) and the shear modulus G (right) [10]

Novel design principles of artificial metamaterial structures exhibit exotic mechanical properties. These tailored properties either cannot be achieved with bulk materials or are very difficult if not impossible to achieve with their mixes. The classification of the mechanical metamaterials according to [10] is given in the schematic diagram of figure 1.2 and the groups are divided according to the modification of one or more elastic constants.

Mechanical metamaterials do not exhibit bulk stiffness at the meso-scale surface because of the micro-scale structure. Therefore the stiffness can be presented with an effective Young's modulus. The ratio of this modulus is the value of the average stress to the average strain that results in the structure when it is subject to

pure shear or pure compression on its meso-scale surface [11]. It, therefore, is representative of the stiffness of the metamaterial. The structures of mechanical metamaterials structures, when tailored to modify their stiffness, are presented in the first group of classifications in figure 1.2.

Mechanical metamaterials, which utilise shear and bulk moduli, are presented in the second classification group of figure 1.2. Exotic materials such as in pentamode structures [4], [1], exhibit hardly any resistance during shear strain. Actually, they exhibit mechanical properties comparable to that of fluids and have a very high bulk K modulus and a very low shear modulus G. In addition to negative compressibility [7] these materials exhibit a negative bulk modulus $-K$. Therefore, when the applied pressure dP is increased, the volume dV also increases.

The third group of classifications given in figure 1.2 belongs to materials which utilise the Poisson's ratio. Mechanical metamaterial structures such as auxetic materials have a negative Poisson's ratio. These are artificial materials indicating an expansion in the lateral direction $d_{\epsilon y}$ when subjected to tension. That is applied to the longitudinal direction (x-direction) of the material structure. They possess enhanced toughness, shear resistance, and efficient vibration absorption [2].

Trade-offs, related to the elastic constants are an important aspect of either finding the limits or exceeding the boundaries of properties as found in conventional bulk materials. The most commonly used trade-off is between Young's modulus and the density and it can be seen as $\frac{E}{\rho}$. This specific modulus is used to determine materials with the minimum structural weight of which deflection or physical deformations are seen as main design limitations. This specific modulus is commonly used in the design of auxetic metamaterial structures.

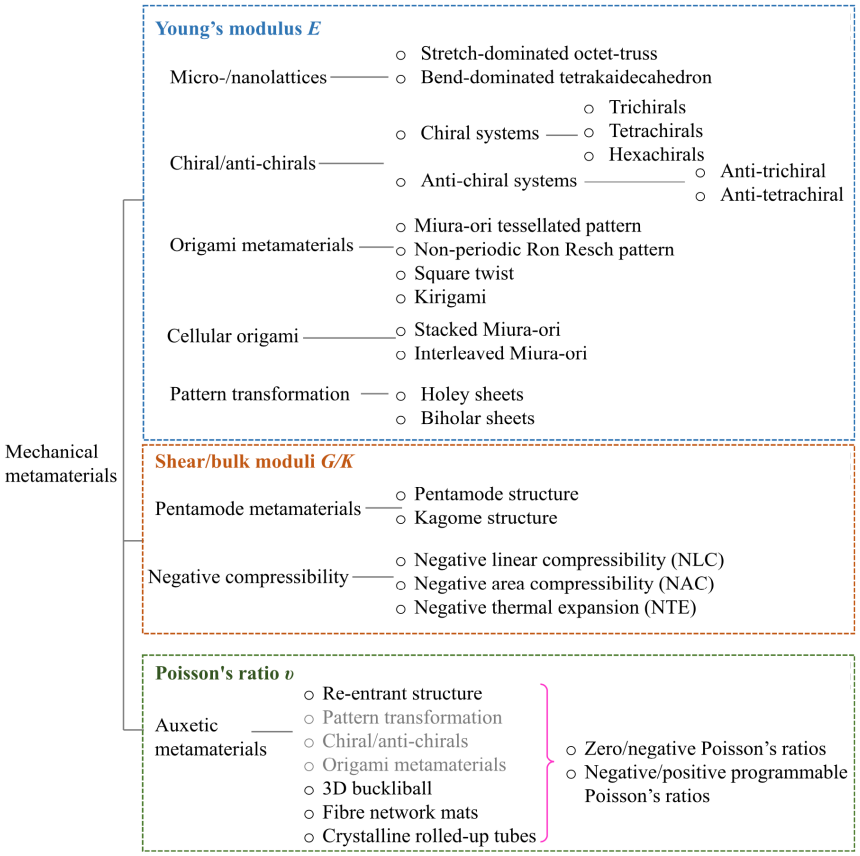

Figure 1.2: Classification of mechanical metamaterial structures [10]

By using tailored properties one may overcome trade-off limits of mechanical properties. However, these metamaterials are constrained in that the mechanical properties are tailored, yet fixed. Active control of these parameters can generate such properties which are desirable for applications with large strain capabilities, lightweight structures, a wide range of damping and stiffness [5]. High-tech, automotive and aerospace industries could greatly benefit from tunable mechanical properties in morphing, dynamic and vibrational isolation applications. However, in order to realise promising concepts, integrated activators in structures of metamaterials are indispensable.

Efforts towards active metamaterials are limited in the current literature. Poon et al. [9] investigated achievable tunable stiffness properties with phase-changing unit cells as illustrated in *A* of figure 1.3. These unit cells consist of silicone rubber spheres with integrated gallium cores. Multiple unit cells form a cubic lattice at meso-scale level. Heating the core and thereby melting the gallium creates a stiffness reduction in the lattice of the cubic structure. They successfully demonstrated a concept design with a stress-strain behaviour consisting of a rate of 3.7 times increasing stiffness at 7% strain. But such active metamaterials have a limited response time due to liquefaction and solidification limits.

Numerous studies on self-folding origami structures can be classified as efforts towards making active metamaterial structures. Overvelde et al. [8] studied mechanical metamaterials whose shape, volume and stiffness can be controlled with the use of pressurized air-pockets in the hinges of the metamaterial unit cell structure, which is presented in *B* of figure 1.3. They connected unit cells in order to form a periodic structure, which generates an extruded cube. Different stress-strain behaviour for different orientations during uni-axial compression was found by them. They, also, reported limitations concerning activation reported and tunability of the unit cells. Other activation principles in origami structures have been studied by Li et al. [6]. They investigated morphing and stiffness variation in active origami metamaterials unit cells, as seen in *C* of figure 1.3. They created five different unit cell configurations each with an effective stiffness characteristic. These different configurations are the result of the relationship between the internal fluid volume and the structure deformation of kinematic folding techniques. They realised an adaptive fluidic origami demonstrator concept but reported limited performance in variable stiffness and the unit cells structures were too complex for scaling.

Hagpanah et al. [3] investigated damping in mechanical metamaterial structures. They demonstrated a concept design based on locking-mechanisms - as seen in *D* of figure 1.3 - consisting of electromagnets and screw pins. They achieved a gradual stress drop of 3KPa, which then lead to constant force behaviour with a resolution of 0.1KPa. Their prototypes suffered from performance degradation during miniaturisation, as well as from difficult to control continuous behaviour.

A promising way to stimulate the development of active metamaterials in the future is the use of so-called smart material transducers. These active composites convert energy between electrical and mechanical domains and can be divided into two categories according to Kornbluh et al. [5]. The first group is using the material in structures as active components. These are intrinsically adaptive materials and react to external stimuli to change their molecular and microscopic structures; these include shape memory alloys, thermal elastomers and various ionic gels. The second group consists of materials that act as energy transducers in order to modulate material properties. The most widely used active materials are ceramic composites such as piezoelectric ceramics, magnetostrictive ceramics and ferromagnetic shape memory alloys. Figure 1.4 illustrates the range of Young's modulus as well as strain in intrinsic and active composites. The application of these materials to activate metamaterials has, as yet, not been explored in literature. The reason may lay with difficult realisation, as well as limited performance of their robustness, specific 'placement' and complex actuation principles.

1.3. Research approach

To recapitulate the state-of-the-art of metamaterials, classification of elastic mechanical metamaterials is based on four elastic constants. Metamaterials possess material properties, which are linked with their unit

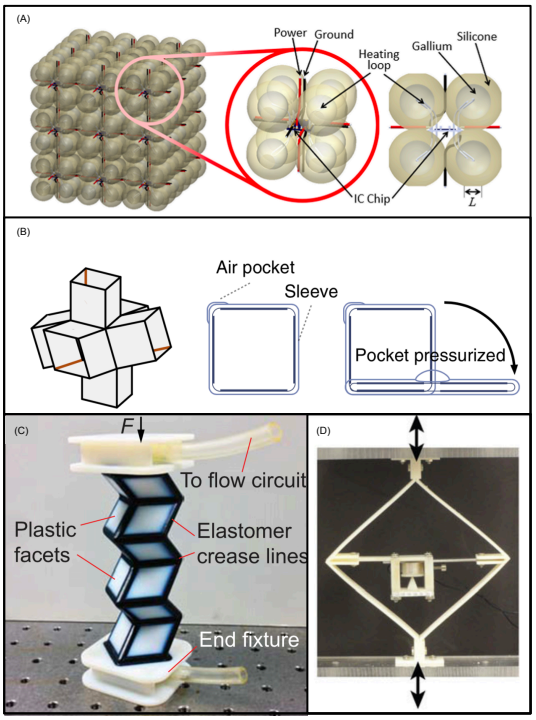

Figure 1.3: Active metamaterial unit cells. (A) phase-changing unit cells activated with core heating [9], (B) Unit cell activated with pressurized air-pockets [8], (C) Origami unit cell based on activation with fluidic control, (D) Unit cell based on electromagnetic locking-mechanisms [3]

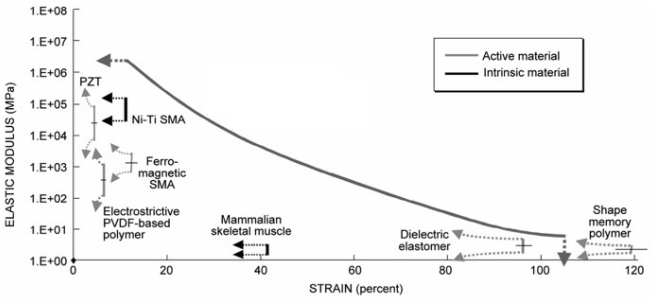

Figure 1.4: Stiffness range as a function of strain for intrinsically adaptive, active materials [5]

cell structure rather than their composition. Therefore, artificial metamaterial structures can achieve tailored properties. The greatest limitation of elastic metamaterials is the fixation of their mechanical properties. In order to tune these properties, activators are required. Current active metamaterials have complex design structures, require difficult actuation principles and therefore do not satisfy the desired characteristics. Adaptive composites show promising features as active components, but, as yet, are not suitable for implementation in mechanical metamaterials.

While smart materials mature, this work proposes to explore exploiting the conventional transducers to make active metamaterials possible and to investigate their design, properties and limitations. Conventional electromagnetic actuators are a well-known option for macro-scale applications due to their robustness, efficiency and high force densities. They are also often used in applications, which require precise controlled and fast response. Electromagnetic actuators are less adopted in the centimeter-scale region. However, they still exhibit long-range force, large deflection and low power consumption. Therefore, electromagnetic actuators with a volume in the centimeter-scale region offer potential solutions as activators in mechanical metamaterials.

In this study, utilisation of centimeter-scale electromagnetic actuators is investigated in order to activate metamaterials. The most immediate challenge in such a concept is downscaling of the electromagnetic actuators. Therefore, a thorough investigation of efforts towards making miniature electromagnetic actuators, and of know-how of their downscaling is conducted. This shows that downscaling is investigated in very small amounts and that electromagnetic actuators are hardly available as actuators in the centimeter-scale region. To be able to benefit from electromagnetic actuators and their adequate properties when scaled in these volume ranges remains a major challenge. Therefore, I next investigate the scaling effects of electromagnetic actuators analytically. Further, I choose to develop a proof-of-principle metamaterial cell for active damping by utilising reluctance actuator as tunable Coulomb dampers that can be electrically regulated to change the magnitude of dissipated energy. I will use a commercially available actuator in order to focus on exploiting the electromagnetic force and avoid implementation details on the actuator. In order to assemble our unit cells, additive manufacturing is chosen for practical efficiency. Thereafter the demonstrator will be analysed and validated regarding performance behaviour, tunability and miniaturisation.

1.4. Thesis layout

This thesis is divided into 3 separately chapters based on the research overview explained in section 1.3. Each chapter is written in an IEEE scientific format. The first paper elaborates reported efforts towards miniaturisation of electromagnetic actuators in a literature review. Thereafter, an analytical evaluation of scaling effects in electromagnetic actuators has been conducted. Lastly, an active metamaterials unit cell is developed with electromagnetic actuators as coulomb dampers.

1.4.1. Miniaturisation of electromagnetic actuators - Literature review

In this study, utilisation of centimeter-scale electromagnetic actuators is investigated and the major challenge in such a concept is the miniaturisation of the electromagnetic actuators. Therefore, an overview of the available literature is presented in chapter 2 to address which scaling laws are present and how they are used in applications with conventional electromagnetic actuators. Firstly, the fundamentals of electromagnetic actuation systems are explained. The different forces of these actuators are elaborated and two major actuation principles are selected for further research. These two actuators address the majority of electromagnetic actuation components. Thereafter, general scaling laws are presented, which are related to fundamental principles that are used in electromagnetic actuators. Rather than developing general miniaturisation of electromagnetic actuators, researchers mostly have used design specific cases. We looked explicitly into these design specific cases of the actuation principles in the centimeter-scale region but concluded that this remains an unexplored scientific area. Therefore, a more elaborate explanation is given with respect to the utilisation of electromagnetic actuators in these small-scale applications. Our conclusion has been that the amount of research regarding the scaling of electromagnets in the centimeter-scale region, regarding performance behaviour and also a comparison of the actuation principles is limited. Electromagnetic actuators in centimeter-scale region till now have largely remained an unexplored scientific area. However, the utilisation of electromagnetic actuators, as has been seen in a limited group of applications, possesses valuable properties that may remove hurdles which currently hamper the use of the Lorentz force and reluctance force actuators in centimeter scale applications.

1.4.2. Evaluation of scaling effects in electromagnetic actuators - Analytical study

My literature study on the miniaturisation of electromagnetic actuators did show that this phenomenon hardly has been examined in the centimeter-scale and less. I, therefore, analytically examined miniaturisation effects of electromagnetic actuators in centimeter-scale region in chapter 3. This analysis consists of a methodology to study scaling effects in two fixed actuator configurations that use Lorentz or reluctance forces. First, their behaviour is described in terms of parameters. Thereafter, a scaling factor is substituted in their configuration to limit complexity while evaluating the actuators during scaling. Moreover, an analysis is given, which elaborates the consequences of miniaturisation. Aspects discussed include actuator force, mechanical work and heat dissipation during scaling of actuator volume, current changes and varying stroke deformations. The results show the performance of the examined actuators in volume regions up to cubic millimeters. In this way, much insight could be gained with respect to the feasibility. Therefore in advance

decisions regarding finite element analyses and experimental verification can be made, which otherwise are very time-consuming.

1.4.3. Activating metamaterials with electromagnetic actuators - Main paper

In chapter 4, a proof-of-principle metamaterial cell is developed. It shows that active damping, by utilising conventional electromagnetic actuators that can be electrically regulated, is well feasible. The literature study in chapter 2 showed that utilisation of electromagnetic actuators, as has been seen in a small group of applications, possesses valuable properties that can be exploited when integrated into metamaterials. Thereafter, the analysis regarding scaling effects in electromagnetic actuators in chapter 3 showed the feasibility of performance of the examined conventional actuators in volume regions up to the cubic millimeter. The objective of chapter 4 is to design, fabricate and validate an active metamaterial unit cell demonstrator. Based on the theory, the unit cell demonstrator of elastic material behaves like a spring component, while the utilisation of reluctance force actuators must indicate Coulomb damping. This Coulomb damping can be seen as a dissipated energy component. In this way, the mechanical metamaterial has been modified by applying conventional transducers. Control over the electromagnetic actuators has resulted in obtaining a tunable damping coefficient, of which the outcomes are defined as a tunable damping ratio between dissipated and stored energy.

2

Paper 1: Miniaturisation of electromagnetic actuators

Miniaturisation of electromagnetic actuators

Dexter Thomas
Departement of Precision and Microsystems Engineering
Delft University of Technology
Mekelweg 2, 2628CD, Delft, the Netherlands

***Abstract*— In this research project, an exploration of scaling in the context of miniaturisation has been conducted. Promising insights into the phenomenon of scaling are found in the literature. However, current research is limited and scaling has not been investigated in a uniform matter. This paper researches the field of miniaturisation of electromagnetic actuation units in the centimeter-scale region. It summarizes the information gathered from scientific papers, textbooks and theses. Research is conducted of the electromagnetic forces present in various electromagnetic actuation units. Examples of units are solenoids, motors and relays. Exotic materials are excluded and deformations, fringing and eddy currents are not taken into account. Variables examined include densities such as force-, energy- and magnetic density. Variables are subjected to a scaling variable to get insight into performance variations during miniaturisation. To establish a more coherent research, a distinction is introduced between two actuator topologies with a dominant electromagnetic force. The research starts with a Lorentz force actuator and followed by a reluctance force actuator. Literature concludes that miniaturisation based on design-specific cases occur more frequently than based on general scaling methods. Therefore, performance behaviour and comparative analysis of electromagnetic actuator performance in centimeter-scale region have largely remained an unexplored scientific area.**

NOMENCLATURE

λ	Spatial scaling factor [-]
μ	Permeability [H/m]
Φ	Magnetic flux [Wb]
ϕ	Temporal scaling factor [-]
$\Re$	Reluctance [H^{-1}]
ρ	Material density [kg/m^3]
A_w	Cross-section air-gap [m^2]
A_w	Cross-section wire [m^2]
B	Magnetic field density [T]
c_D	Compression factor [-]
D	Displacement field [C/m^{-2}]
d	Radial distance from the current i [m]
D_t	Aperture diameter [m]
E	Electric field [V/m]
e	Electric field strength scaling factor [-]
E_y	Young's modulus [N/m^2]
F_a	Force between two current carrying wires [N]
F_b	Force between current carrying wire and permanent magnet [N]
f_m	Sum of the total magnetic force per volume [N/m^3]
H	Magnetic field strength [A/m]
h	Magnetic field strength scaling factor [-]
i	Current [A]
I_f	Free current [A]
J	Current density [A/m^2]
n	Number of turns [-]
N_a	Number of actuators [-]
P	Power dissipation [W]
p_w	Wind pressure [N/m^2]
Q	Dissipated heat [J]
S	Surface area [m^2]
V	Volume [m^3]

I. INTRODUCTION

Miniaturisation has been important to many of the technological advances that have occurred in the past years. Improvements in micro-fabrication techniques have enabled a reduction of the size of microelectronic components. Electromagnets dominate at the macro-scale, but less so at the smaller scale. When an electromagnetic actuator is reduced in size, numerous complexities emerge and there still is a need for further improvement of stroke length, power and manufacturing strategies. The scaling domain of the electromagnetic actuators as discussed in this paper will be mainly focused on the centimeter- to millimeter-scale region. Obviously, previous research that may be relevant to this project must be discussed precisely. A complete overview of miniaturisation of electromagnetic actuators, along with the evaluation of theory, and also evidence in the miniaturisation of the electromagnetic actuator domain must be presented. Results and conclusions from various scientific studies and textbooks will be evaluated and compared; disagreements and similarities that may appear in the context of multiple studies on scaling electromagnetic actuators will be elaborated upon. First, an investigation of the principles of the mechanical and electromagnetic domain will be undertaken in section II. Due to a broad range of scaling objectives for electromagnetic actuators, a separate section is devoted to the forces present in electromagnetic actuators regarding scaling, presented in section III. In this way, the state-of-the-art in this field is presented regarding actuators of which the configuration creates actuation based on dominant Lorentz and reluctance forces. Lastly, the findings regarding the utilisation of electromagnetic actuators in small-scale systems are assessed in a concluding section IV.

II. Fundamentals of electromagnetic actuation systems

The performance of an electromagnetic actuator is based on the magnetic field density that is present in the system. Therefore, to understand the output performances of scaling principles, it is necessary to understand the working principles first. In this section, the fundamentals of the electromagnetic actuator are described.

A. The essence of mechanical actuation

An electromagnetic actuator is defined as a device that can modify the mechanical state of a system with which it is connected [1]. The system establishes a flow of energy between an input port and an output port. Two conjugate variables will ultimately define the power exchange, at the input as well as the output ports. One is an effort, such as force or torque, and the other a flow such as velocity or current. The performance of the electromagnetic actuator translates in the output of the system. The output domain is mechanical energy, based on the two conjugates called velocity and force. Eventually, a small part of the input power will be dissipated into heat losses. A simplified representation of an actuator is illustrated in figure 1.

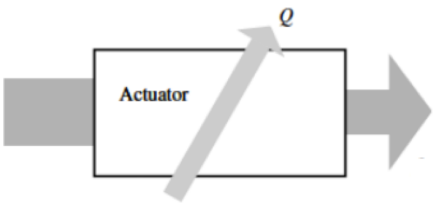

Fig. 1: Actuator unit concept [1]

The essential mechanism of an actuator is the transducer. The transducer converts different energy forms or different energy types within the same energy form (i.e. rotation to translation). Seven main energy domains are present [1] and conversion can be found between any two of these domains. The output of an electromagnetic actuator is the electromagnetic force and can be defined as a gradient of the mechanical energy of a system [2].

B. Electromagnetic force principle

Electromechanical transduction is the conversion of the electrical domain into the mechanical domain. Within these two domains, there are various transduction phenomena possible [1]. In the scope of this literature review, only the electromagnetic actuators are considered. The energy exchange between the paired domains of the electromagnetic actuator occurs in a controllable and predictable manner in such a way that the total force depends on the spatial distribution of currents, magnetic fields, electric fields, and material properties. Therefore, numerous actuator designs with different characteristics can be created [3]. Examples of macro applications are electro-motors, solenoid actuators and moving coil actuators. Even micro-applications use electromagnetic actuators, such as MEMS switches and relays.

The electromagnetic force is derived from the macroscopic formulation principles of electromagnetism and from the physics area that describes the phenomena, associated with electric and magnetic fields and their interaction [4]. The equations introduce the displacement field D, electric field E, magnetic field B, the differential vector element of surface area S (denoted as dS), electric current density J_f, magnetic flux Φ, permeability μ and the free current I_f. If free charge and mechanical deformations are disregarded, the behaviour of the actuator can be explained by Maxwell's equations 1 and the magnetic force density f_m in equation 2.

$$\oiint \vec{D} \cdot \ d\vec{S} = 0 \tag{1a}$$

$$\oiint \vec{B} \cdot \ d\vec{S} = 0 \tag{1b}$$

$$\oint \vec{E} \cdot d\vec{s} = -\frac{d\Phi}{dt} \tag{1c}$$

$$\oint \vec{H} \cdot d\vec{s} = I_{\mathrm{f}} \tag{1d}$$

$$\vec{f_m} = \vec{J_f} \times \mu\vec{H} - 1/2\vec{H} \cdot \vec{H}\nabla\mu \tag{2}$$

Exotic materials and fringing are not in the scope of this paper, which excludes the research of magnetostrictive and superconductor actuators. Within the given boundaries, three force types can be distinguished, which are present in electromagnetic actuators.

- **Lorentz force** Lorentz force is perpendicular to the magnetic flux lines of an externally applied field due to a current-carrying wire or permanent magnet.
- **Reluctance force** Reluctance force acts perpendicularly to the surface of materials with different permeability (air-gap, iron yoke), parallel to the magnetic flux lines.
- **Inductance force** Inductance force acts perpendicularly to the magnetic flux lines of a changing externally applied field strength; here the working principle is not immediately visible from the generalized force equation due to its dynamic nature [4]

It should be noted that in this paper, two actuator types will be explained based on a dominant force type. These force types are the Lorentz and reluctance forces. They represent the essence of most electromagnetic actuators. Therefore, the inductance force principle, also a dominant force, will not be explained in this literature review. Nevertheless, it will still be mentioned as an additional force when present.

The forces, pertaining to applications using electromagnetic actuators are based on generating a magnetic field density B. Two basic configurations are presented to describe different ways to generate a magnetic field. The first configuration generates a magnetic field due to a permanent magnet, and the system is thus based on the material properties of the permanent magnet used. The other configuration is the current-carrying wire. The configuration of the current-carrying wire is extended to a design of multiple current-carrying wires, a so-called coil. Therefore, it imitates a permanent magnet with a north and south pole between the two sides of a solenoid due to superposition principle 2.

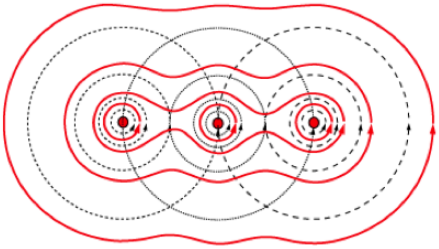

Fig. 2: Superposition principle of current carrying wires [5]

The magnetic flux density generated is still useless if it would remain inside the ferromagnetic yoke. Therefore, it is necessary to create a space called an air-gap. Inside this air-gap, an externally applied magnetic field will be created. This field will be of significant influence for the Lorentz and reluctance forces and consists of the vacuum permeability μ_0, the current density J, the cross-sectional area A_w and the length of the flux path d. The magnetic field in an air-gap B_g can be written as:

$$B_g = \frac{\mu_0 J A_w}{d} \tag{3}$$

The magnetic flux ϕ can be derived from the magnetic field density B and cross-section of the air-gap A_g. However, can also be written as a function of ampere-turns ni over the reluctance $\Re$ as:

$$\phi = BA_g = \frac{ni}{\Re} \tag{4}$$

At last, there is the reluctance $\Re$, which is an approximation of the dominant air reluctance assumed by Chapman et al. [6] and which consists of the length of the flux path d, the vacuum permeability μ_0 and cross-section A_g and can be seen as:

$$\Re = \frac{d}{\mu_0 A_g} \tag{5}$$

It is now clear how to calculate the magnetic density in general. Nevertheless, in order to apply this to a specific case, a distinction is required between two electromagnetic force principle models, the reluctance force and Lorentz force actuation models. These are explained and analytically reviewed for the topology of figure 3 and 5.

C. Conventional Lorentz force actuators

Actuators with dominant Lorentz forces are applied in high precision positioning systems due to the low mechanical stiffness between the stationary and moving part of the actuator. Figure 3 illustrates the working principle of a conventional Lorentz force actuator. The relation between force and current input is linear, which implies a better control of the system. However, the downside is a relatively modest force output to the current input ratio [5]. Therefore, this will limit the maximum acceleration and stroke range.

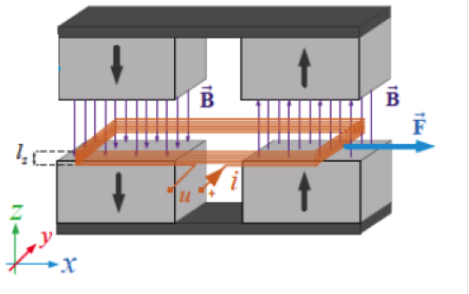

Fig. 3: Conventional Lorentz force actuator [2]

Regarding the Lorentz force principle, the generation of a magnetic field in an air-gap is illustrated in figure 4. It is possible to calculate the magnetic forces on a current-carrying wire based on interaction with a current-carrying coil or a permanent magnet. This force can be calculated from the derivation of the electromagnetic force law given in section II-B. To a certain degree the interacting force illustrated in figure 4 is the force on a moving particle or current in a wire segment with current i, length dl and magnetic field density B and can be seen as:

$$dF = idl \times B \tag{6}$$

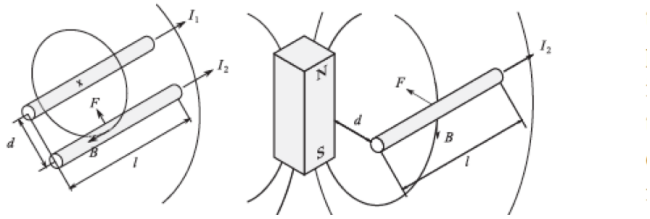

Fig. 4: Interaction of current carrying wires (left) and Interaction of a Permanent magnet with a current carrying wire (right) [7]

D. Conventional reluctance force actuators

An actuator can be designed in such a way that the reluctance force becomes the more dominant force. It is composed of a ferromagnetic core that is divided into two parts, the mover and stator. The coil is wound around the stator with a certain number of coil-turns illustrated in yellow in figure 5. If an electric current flows through the coil-turns, a magnetic field is created in both the inside of the ferromagnetic material and in the air-gap between the stator and the mover. It generates an attraction force of the iron mover towards the stator component.

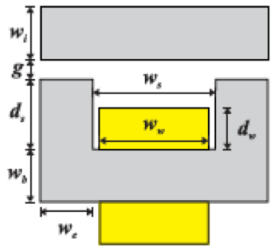

Fig. 5: Reluctance force actuator topology [8]

In contrast with the Lorentz actuator, the force of the reluctance actuator is non-linear to the current input. In general, at increased current levels, the force will change in a non-linear pattern due to different causes [5]. As mentioned in II, the reluctance force F_r performs perpendicularly to the surface of materials with different permeability (air-gap, iron core). This force runs parallel to the magnetic flux lines, and its magnitude is proportional to the squared current [5]. The reluctance force F_r consists of the air-gap l_g, ampere-turns ni, vacuum permeability μ_0 and the cross-section A_g and can be written as:

$$F_r = -(\frac{ni}{l_g})^2 \frac{\mu_0 A_g}{4} \tag{7}$$

At a certain current level, the magnitude of the force decreases when the displacement increases [5], which implies that conventional reluctance actuators are motion dependent.

III. Scaling Laws

The subject of scaling an electromagnetic actuator is central to this research project and thus calls for a precise theoretical overview. The objective of this section is to assess this research domain and critically integrate the multiple findings. One of the consequences of scaling is the implicit uncertainty of the output performance of the actuator. Knowledge on the behaviour of an actuator is indispensable for the design and optimization stages of electromagnetic actuator manufacturing. Studies, such as have been undertaken by Judy [9], have shown that some dimension domains are constrained by specific actuation principles. He has proven that the boundary ranges from 1 to 10 mm deflection are disadvantageous for magnetic actuation and thus utilisation is required. However, magnetic actuators have drawn attention in the lower domain due to their long-range force, large deflection and low power consumption. And, therefore new techniques and manufacturing methods in scaling do not match comfortably with the dimension domains as hypothesized by Judy [10].

A. General scaling fundamentals

It has been shown in figure 4 that electromagnetic actuator systems are primarily based on the interaction between elements that can generate magnetic fields. Scaling of these elements and their mutual interaction will lead to a clear insight into the fundamentals of electromagnetic actuator scaling. Cugat et al. [10] studied a comparison between the magnetic moment of a cylindrical magnet and a current-carrying coil of the same shape and size, as illustrated in figure 6. They argued that the magnetic moment of the magnet is proportional to its magnetization J and its volume V; here, J is a property and does not depend on a scaling factor. In this study they used a scale reduction factor of $1/k$ to enable their work on miniaturisation. The overall magnetic moment of the permanent magnet M_m then is scaled with a factor of $(1/k)^3$. The equivalent magnetic moment of the coil M_c is proportional to the total current i flowing inside the wire and to its surface and is substituted with current density J. Cugat et al. [10] concluded that the moment of the current-carrying coil then is scaled with $(1/k)^4$ as can be seen in the proportional relationship, presented in 8, whereas the magnetic moment M_m is only reduced by $(1/k)^3$ as a proportional relationship, as can be seen in relation 9. In order to maintain the same scaling reduction factor, the current density J must be increased and this will eventually lead to higher heat dissipation losses in the wires. Therefore, the outcome of this study implies the benefits of permanent magnets in smaller-scaled electromagnetic actuators. Unfortunately, for reluctance force actuators, permanent magnets could not be implemented based on their actuation principle, unless more promising complicated hybrid designs are used, as mentioned in the textbook by Schmidt, entitled 'The design of high performance mechatronics' [5].

$$M_c \propto i(1/k)^2 \propto J(1/k)^4 \tag{8}$$

$$M_m \propto J(1/k)^3 \tag{9}$$

A more general approach to scaling is conducted by Hsieh et al. [11] and Wood [12]. They both studied scaling laws based on mathematical foundations such as the Fourier analysis and boundary element methods to form suitable scaling rules for reducing the computational effort by a significant factor. Hsieh et al. [11] introduced a set of scaling

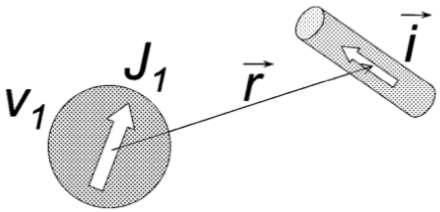

Fig. 6: Interaction between a permanent magnet and a current carrying wire [10]

relations for two scaled models of an electro-mechanical rail and armature system with the exact images of the temperature field and the stress field. They stated that the performance in one scaled model could be extrapolated to the other scaled model, which is illustrated in figure 7. This set of scaling relations is derived from the electromagnetic diffusion equation, the thermal diffusion equation, and the moment equation. The constraints of this set consist of the time scaling factor, which is the square of the geometric scaling factor; the current pulse shape is maintained, and the current amplitude is linearly proportional to the geometric scaling factor. Under these constraints, the scaled systems were validated and proven to be the exact images of the magnetic flux density, temperature and stress fields in the two scaled models just as had been hypothesized by Hsieh et al. [11].

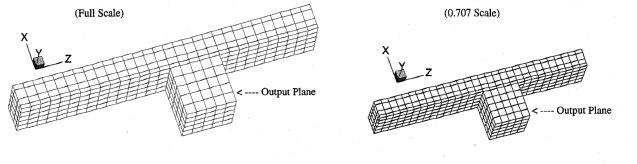

Fig. 7: Finite element mesh of the rail and armature [11]

Wood [12] also examined the scaling laws and referred to them as constant-energy scaling. He opted for a thorough examination of the scaling properties of electromagnetic and magnetic systems without the use of numerical methods. Linear electromagnetic systems were found by him to fit four dimensions of scaling within the design space. The quantities of the four dimensions of scaling are the spatial factor λ, temporal factor τ, the electric field e and magnetic field h. Next, non-linear magnetic systems as modelled by the Landau-Lifshitz-Gilbert equation can be scaled in two design dimensions. The two independent scale factors are the temporal scaling factor τ and the spatial scaling factor λ. Their objective was to state a set of scaling rules that preserves the energy barriers as well as the thermal field of the magnetic systems. If this requirement would be met adequately, the system may be scaled, be it in one dimension of design space only. All equations are derived from the set of Maxwell equations 1.

B. Lorentz force actuator scaling

Certain scaling laws, that were discussed in the previous section now firstly will be applied to a conventional Lorentz force actuator to assess the impact on the process of miniaturisation. Since only a limited number of relevant studies were found, it has been possible to gain a comprehensive insight into their content by presenting their actuation and performance in figure 8.

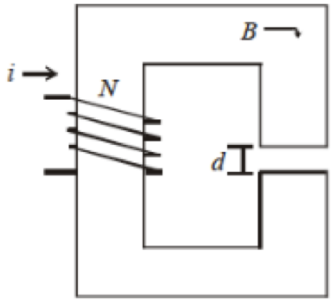

Fig. 8: Magnetic flux generated by a current carrying coil wound around a ferromagnetic yoke. The reluctance of the magnetic flux path is a combination of the reluctance of the air-gap and the ferromagnetic yoke [6]

Chapman et al. [6] examined the fundamental scaling issues in conventional Lorentz force actuators; the graph in figure 9 illustrates the relation between an air-gap and the energy density of a micro-scale actuator. The example given in graph 9 is for a variable air-gap d, several coils $n = 10$, current density J of 10^7 A/m and a chosen magnetic field density of 1 T. It is now possible to calculate the area for the wire placement of a Lorentz force actuator of figure 8. The area, which has been calculated, is minimal, while not even a fill factor has been applied. It shows that energy density in the air-gap is connected with the current density; this may well be a limiting factor in the scaling of an electromagnetic actuator.

Scaling is different when the magnetic field is generated by a permanent magnet. The generated magnetic field scales with a factor L^0 due to its constant magnetization related to its material properties [10]. Trimmer [13] looked into both cases. The force F_a is derived from the force equation 6. The force F_a consists of the vacuum permeability μ, line segment l, current i_1 of wire 1, current i_2 of wire 2 and the distance d between the centre of wire 1 and 2; this is illustrated on the left side of figure 4 and can be written as:

$$F_a = \frac{\mu_0 l i_1 i_2}{2\pi d} \tag{10}$$

In the second case, he substitutes wire 1 with a permanent

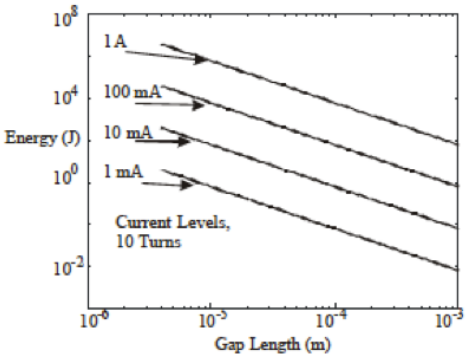

Fig. 9: Energy density as a function of gap-length considering constrained current with $n = 10$ [6]

magnet and then a force F_b is generated due to a permanent magnet and wire 2, as illustrated at the right side of figure 4. The force F_b consists of the wire current i_2, line segment l and the magnetic field density of the permanent magnet B as:

$$F_b = i_2 l \times B \tag{11}$$

Trimmer [13] thus has shown how the two-scale down in reaction to a single scale variable L, which represents the linear scale of the system. The outcome of scaling the forces, now – with the Lorentz force actuator – is different depending on the theoretical case that is being examined. For instance, a first case describes scaling of the force that is based on a constant current density, which implies a scale reduction factor of L^0 current density, assuming that the current $i = JA$ scales as L^2. In a second case, the heat dissipation rate per unit surface area of the wires is held constant. Then, according to Trimmer [13], the current density will scale as $\sqrt{L}$. In one more case, the temperature that the wire and the insulation can withstand will be constrained by a maximum value. This, with the balance of conductive heat dissipation and Joule heating [7], implies that the current scales as L^1. The different constraining forces and scaling laws, that have been discussed so far, can lead to different values of heat dissipation, transit times and accelerations [13] and can be seen in table 10.

Table 1 Force scaling law of magnetic actuators.

	current-current	current-magnet
$I \propto L^2$	L^4	L^3
$I \propto L^{1.5}$	L^3	$L^{2.5}$
$I \propto L^1$	L^2	L^2

Fig. 10: Lorentz force scaling laws according to Trimmer[13]

C. Reluctance force actuator scaling

Reluctance force actuators are a popular option for macro-scale applications due to their efficiency and high force densities. But, also, in the small micro-region of the MEMS applications, the reluctance force actuator is often used. However, for the centimeter-scale domain, there is insufficient knowledge on the possibilities of scaling with actuator integration, and therefore reluctance actuators are rarely selected. This gap in the literature has been studied to a certain extent by Nami et al. [14]. They investigated the design criteria for the reluctance force principle, which are examined in the macro-scale region and the micro-scale region. They analysed scaling for two reluctance force actuation types. In the one, motion creates changes in the gap length, in the other, motion changes the gap overlap area without separating the gap, like in rotatory driven electromagnetic actuators, presented in figure 8.

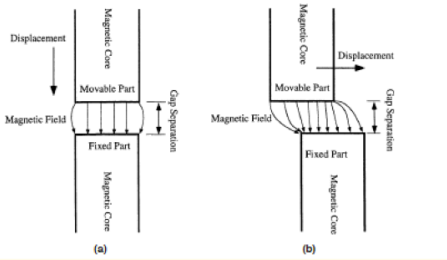

Fig. 11: Schematic diagram of the two different types of magnetic micro-actuators based on linear movement or rotary movement [14]

Chapman et al. [6] argued that most of the reluctance energy is contained in the air-gap and that reluctance of the core is often neglected. Nami et al. [14] wanted to correct this state of affairs. They implied that the total energy that is stored in a small-scale electromagnetic reluctance force actuator is proportional to the sum of energy which exists in the gap and the core. Since there are no strict dimensions set for the boundaries, it is necessary to size carefully the gap area as well as the initial gap separation. This, in order to satisfy the maximum force design criterion of magnetic micro-actuators. Nami et al. [14], however, admitted that it is difficult to determine whether or not the core reluctance influences substantially the total reluctance.

IV. Utilisation of Electromagnetic Actuators in Small-Scale Systems

Currently, studies in the limited field of electromagnetic actuators in centimeter-scale applications have resulted in impressive cases of single actuators or actuator arrays in distributed actuation systems, such as in medical, automotive and high tech applications. In this section, an examination and evaluation regarding the methodologies of these design-specific applications are introduced. For optimization of the electromagnetic actuator in these cases, one must take the constraints of the actual applications as a leading guide.

A. Adaptive deformable mirrors

Ground-based telescopes form a good example of the advantage that scaling offers for their performances. These telescopes namely require real-time corrections in order to suppress wave-front distortions. This requirement could be met by using a deformable mirror as is illustrated in 12. Hamelinck [15] pioneered with this research on small-scale electromagnetic actuators with high stroke resolutions for such applications.

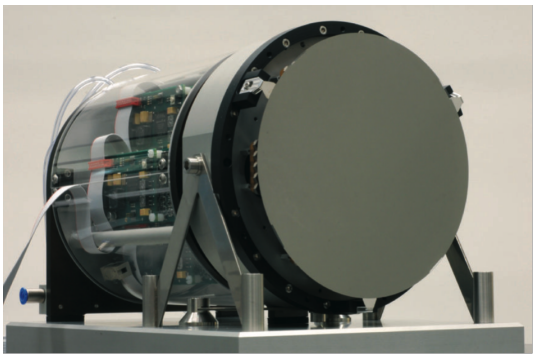

Fig. 12: Adaptive deformable mirror [15]

The challenges regarding deformable mirror applications consist of actuator scaling, distribution and stroke resolution in order to obtain the required performance criteria. The reluctance actuator is chosen for its high force-density and low energy dissipation. The cross-sectional view of the design is illustrated in figure 13 and consists of three reluctance actuators in an array formation. The actuators are attached to a standard base plate and connected to the deformable mirror via a rod. Each actuator consists of a permanent magnet, a surrounding coil, an air-gap, a ferromagnetic moving core, a membrane suspension, a second air-gap and a base plate. A permanent magnet, now, creates a static deflection of the membrane suspension. This is called the equilibrium position and thus, due to this static deflection, the magnetic force generated by the actuator could provide the necessary stroke in both directions in order to fulfil the requirements of the deformable mirror.

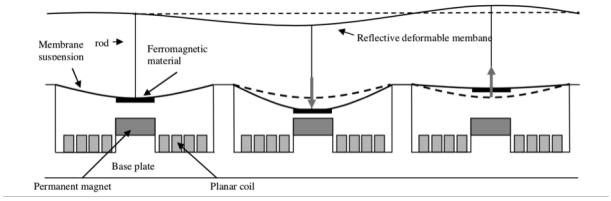

Fig. 13: schematic view of actuator array in the deformable mirror application [15]

The most important output variables regarding scaling are force, resolution, stroke and dissipation. He considers two cases to examine the possibilities of scaling. Firstly, the mirror face sheet thickness t_f is defined as the maximum inter actuator deflection that is caused by the gravitational acceleration term g. Sheet thickness, the second case, is determined by the maximum inter actuator deflection caused by wind pressure p_f. Both cases are related to the total actuator force F and the power dissipation P, but scale differently depending on the parameters. The two cases are specified in proportional relationship 12 and 13. The first case indicates the scaling laws for F and P when gravity determines the sheet thickness, including the aperture D_t, compression factor c_D, number of actuators N_a, wind pressure p_w and material properties E_f and ρ_f. It should be noted that the gravitational acceleration term g is not included in end relation 12, but is presented in the derivation steps given in the study of Hamelinck [15]. The scaling laws of the second case are given in proportional relationship 13 and include the parameters aperture D_t, compression factor c_D and wind pressure p_w.

$$P \propto F^2 \propto (\frac{D_t}{c_D})^8 \frac{1}{N_a^2} \frac{\rho_f^3}{E_f} \tag{12}$$

$$P \propto F^2 \propto (\frac{D_t}{c_D})^4 p_w^2 \tag{13}$$

B. Bone conduction transducers

Hearing aid applications are another field of research that requires small-scale electromagnetic actuator technology. The first hearing aid transducers were solely based on a microphone and an earphone (receiver) presented in figure 14. However, with the passing of time smaller hearing aid systems were demanded, and fortunately, with the development of better bone conduction techniques, size reduction was feasible. Bone conduction transducers are devices that transmit sounds through the bone of the skull and soft tissue. It transforms the electrical input into mechanical vibration. This paper investigates the potential of electromagnetic transducers to accomplish this process.

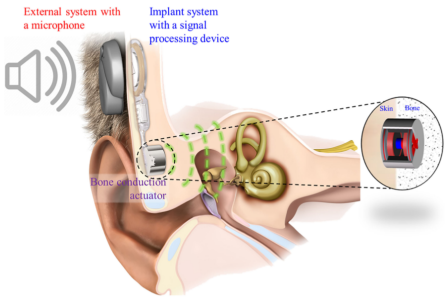

Fig. 14: Bone transducer [16]

The electromagnetic actuators that are used for hearing device applications are based on conventional Lorentz force and reluctance force actuators as illustrated in figure 15. In both designs, a vibrated spring suspension is inserted that connects the stator to the armature. However, trade-offs are to be taken into account. First, distortion

may occur due to deterioration of the electrical signal in the transducer during the electromechanical conversion. Non-linear distortion products, namely, have a significant influence on the mechanical vibratory output. In order to achieve the desired low level of distortion, a heavy high static flux is necessary. Secondly, the system requires a very stiff suspension in order to achieve a high static flux. Also, a heavy counter-weight mass is required to avoid reducing the low-frequency response. Therefore bone conduction systems with low distortion have inadequate frequency response. The opposite remains the same; a good low-frequency response suffers from high distortion.

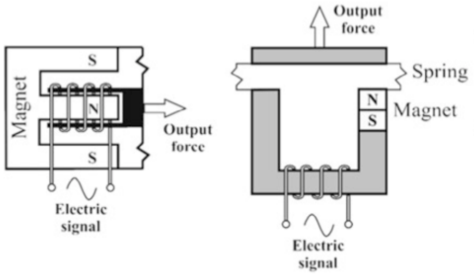

Fig. 15: Basic conventional electromagnetic actuators in bone conduction devices [17]

Hakansson [18] developed a novel bone transducer design to improve the performance of the electromagnetic actuator. He introduced a balanced suspension principle that is shown in figure 15 in a novel design. The novel design in figure 16 uses separate flux paths. This counterbalance of static forces may be achieved by applying a second air-gap. The transducer in figure 16 has circular symmetry and the static forces of the upper and lower gaps counteract due to their equal force magnitude in the opposite direction. In this way, both the distortion and the size of the transducer can be reduced.

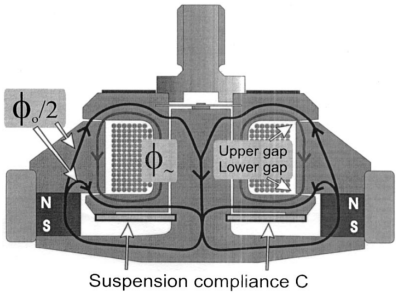

Fig. 16: Schematic view of the balanced electromagnetic separation transducer [18]

C. Synchronous linear and rotary systems

A third application is the synchronous reluctance motor (synRM) that is widely used in today's high-tech manufacturing and industrial use environments. The synRM is based on the reluctance force. An essential schematic representation is shown in figure 17 and consists of an iron rotor with different proportions of inductance along with both the d- and q-axis. The other part of the system is a stator with distributed winding to induce a magneto-motive force.

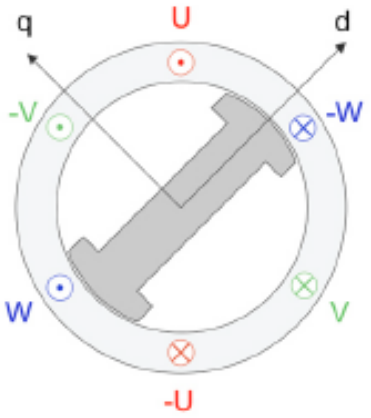

Fig. 17: Schematic view of synchronous reluctance motor [19]

Recent developments in power electronics, material science and micro-controllers have contributed to state-of-the-art electric motor technologies and enhanced the performance of the synRM. Numerous state-of-the-art investigations focus on performance optimization by rotor geometry, control strategy, and compare SynRM with similar machines such as synchronous permanent magnet systems and inductance machines. However, size and weight are currently standard limitations for these systems. Therefore, new methodologies are required for the estimation of electrical, mechanical and magnetic parameters which are essential for optimal performance of scaled designs. Taghavi et al. [20] established a flow diagram for the scaling procedure of a synRM. In the illustration of figure 18, the upper part consists of initial data and presents key parameters that will be used for the estimation of magnetic, geometric and electric parameters. The bottom part of the diagram gives the methodology that analyses the performance of the machine and relates to the obtained output. Finite element software is applied, and if the results do not satisfy the design requirements, the process will be repeated by updating the initial data input.

Schillingmann et al. [19] took a different approach and assigned parameters to the rotor design as is illustrated in figure 19. These parameters are required to find the number of slots for the given rotor geometry and, next, to

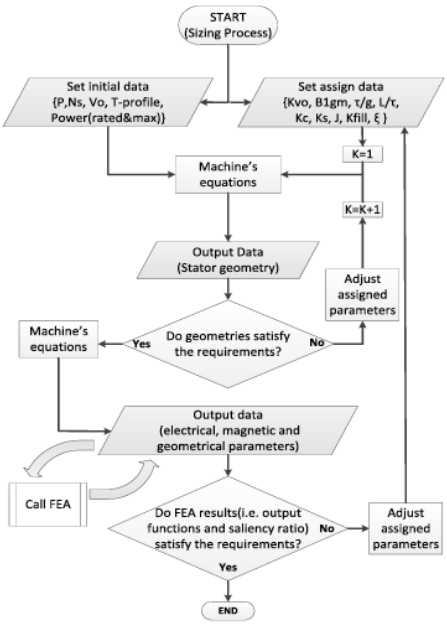

Fig. 18: Flow diagram of the synRM sizing procedure [20]

allow for multi-physics analysis of the mechanics. Finally, a synthesizing analysis of the electromagnetic and mechanical physics has been made. This synthesizing outcome yields a Pareto-optimum of one rotor radius as is illustrated in figure 20.

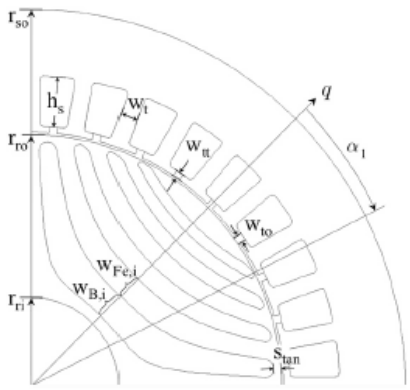

Fig. 19: Parameters rotor design [19]

V. Discussion

This paper has examined textbooks, scientific papers and doctoral theses to examine and to assess the available literature in the field of scaling electromagnetic actuators. The objective has been to establish a strong theoretical foundation for electromagnetic actuator miniaturisation. The following shortcomings and gaps in the literature have been observed:

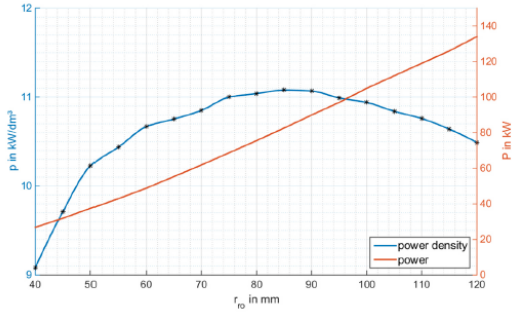

Fig. 20: Pareto-optimum of one rotor radius [19]

- It may be concluded that design specific electromagnetic actuators as can be seen in the applications discussed in section IV have insufficiently taken into account general scaling laws. System constraints and performance objectives mostly then define the methodology that has been applied.

- Feasibility studies regarding electromagnetic actuators scaling rarely have been undertaken. Chapman et al. [6], Nami et al. [14], and Trimmer [13] looked into conventional actuator topologies and their scaling characteristics. These studies in essence just introduced the theme of scaling; yet the theme of actuator feasibility calls for much further analysis.

- In-depth qualitative comparative scaling analysis for output forces that are present in conventional electromagnetic actuators as yet has not been studied in great depth. Applications in medical, automotive and high tech industry may benefit greatly from new insights in scaling analysis for miniaturisation of production processes.

VI. Conclusion

This review has examined the literature on the scaling of electromagnetic actuators in the sub centimeter- to millimeter-scale region. Rather than developing general miniaturisation of electromagnetic actuators, researchers mostly have used design specific cases. This is understandable since objectives can vary and lead to different scaling constraints. Also, the non-linearity in the reluctance force poses major challenges regarding the study of scaling effects. Therefore, performance behaviour and comparison of the actuation principles of electromagnetic actuators in centimeter-scale region till now has largely remained an unexplored scientific area. However, the utilisation of electromagnetic actuators that possess valuable properties may remove hurdles that currently hamper the use of the Lorentz force and reluctance force actuators in centimeter scale applications. More specifically, the themes of scaling limitations, of feasibility criteria and utilisation of electromagnetic actuators form the thrust of this research

project.

REFERENCES

[1] J. Pons, *Emerging Actuator Technologies*. 2005.

[2] A. Katalenic, *Control of reluctance actuators for high-precision positioning*. No. april, 2013.

[3] E. M. H. Kamerbeek, "Magnetic bearings," *Philips technical review*, 1983.

[4] L. Molenaar, *A novel planar magnetic bearing and motor configuration applied in a positioning stage*. PhD thesis, Delft University of Technology, 10 2000.

[5] R. M. Schmidt, G. Schitter, and J. van Eijk, *The design of high performance mechatronics*. 2011.

[6] P. L. Chapman and P. T. Krein, "Micromotor technology: Electric drive designer's perspective," *Conference Record - IAS Annual Meeting (IEEE Industry Applications Society)*, vol. 3, no. May, 2001.

[7] D. K. C. Liu, J. Friend, and L. Yeo, "A brief review of actuation at the micro-scale using electrostatics, electromagnetics and piezoelectric ultrasonics," *Acoustical Science and Technology*, vol. 31, no. 2, 2010.

[8] S. D. Sudhoff, G. M. Shane, and H. Suryanarayana, "Magnetic-equivalent-circuit-based scaling laws for low-frequency magnetic devices," *IEEE Transactions on Energy Conversion*, vol. 28, no. 3, 2013.

[9] J. W. Judy, "Microelectromechanical systems (MEMS): Fabrication, design and applications," *Smart Materials and Structures*, vol. 10, no. 6, 2001.

[10] O. Cugat, G. Reyne, J. Delamare, and H. Rostaing, "Novel magnetic micro-actuators and systems (MAGMAS) using permanent magnets," *Sensors and Actuators, A: Physical*, vol. 129, no. 1-2 SPEC. ISS., 2006.

[11] K. Hsieh and B. Kim, "One Kind Of Scaling Relations On Electromechanical Systems," *IEEE Transactions On Magnetics*, vol. 33, no. 1, 1997.

[12] R. Wood, "Scaling Magnetic Systems," *IEEE Transactions On Magnetics*, vol. 47, no. 10, 2011.

[13] H. Trimmer, "Microrobots and micromechanical systems," 1989.

[14] Z. Nami, C. H. Ahn, and M. G. Allen, "An energy-based design criterion for magnetic microactuators," *Journal of Micromechanics and Microengineering*, vol. 6, no. 3, 1996.

[15] R. Hamelinck, "Adaptive deformable mirror: based on electromagnetic actuators," 2010.

[16] D. H. e. a. Shin, "Design of a dual-coil type electromagnetic actuator for implantable bone conduction hearing devices.," *Official journal of the European Society for Engineering and Medicine*, pp. 445–454, 2019.

[17] M. Killion, A. Halteren, S. Stenfelt, and D. Warren, "Hearing aid transducers," pp. 59–92, 09 2016.

[18] E. Hakansson, "The balanced electromagnetic separation transducer a new bone conduction transducer," 2003.

[19] H. Schillingmann, C. Heister, and M. Henke, "Scaling process of synchronous reluctance machines for automotive applications," *2017 IEEE Transportation and Electrification Conference and Expo, ITEC 2017*, 2017.

[20] S. Taghavi and P. Pillary, "A sizing methodology of the Synchronous Reluctance Motor for Traction application," *IEEE Journal of Emerging and Selected Topics in Power Electronics*, vol. 2, 2014.

3

Paper 2: Evaluation of scaling effects in electromagnetic actuators

Developing a methodology to evaluate scaling effects in electromagnetic actuators

Dexter Thomas
Departement of Precision and Microsystems Engineering
Delft University of Technology
Mekelweg 2, 2628CD, Delft, the Netherlands

***Abstract*— The miniaturisation of electromagnetic actuators in a subcentimeter-scale region remains an ill-defined area in scientific research. Limited research has been done regarding effects for scaling. Predominantly, these studies focus on specific electromagnetic actuator designs. Therefore, this paper presents a methodology to evaluate scaling effects in two conventional actuator designs that exploit Lorentz and reluctance forces. A scaling factor is used in such a way that proportions remain equal while actuator size can be scaled through a single parameter. Actuator performance is studied with respect to magnetic core saturation, current limitations and air-gap variations. Therefore, the methodology consists of feasibility evaluation and comparative analyses between the two actuator systems. The analysis is based on quasi-static actuation. Therefore, dynamic actuator behaviour was not taken into account. Furthermore, finite element methods and experimental analyses are still required to get insight in the complex study of magnetic flux distribution, magnetic field density, and magnetic flux path.**

NOMENCLATURE

α	Dimension variable [m]
β	Dimension variable [m]
F	Magnetomotive-force [A]
μ_r	Relative magnetic permeability [-]
μ_r	Vacuum permeability [$\frac{H}{m}$]
Φ_g	Magnetic flux in air-gap [Wb]
Φ_w	Magnetic flux in coil [Wb]
ρ	Specific resistance of copper [Ωm]
ρ_{cu}	Copper density [$\frac{kg}{m^3}$]
ρ_{Fe}	Iron density [$\frac{kg}{m^3}$]
ρ_m	Magnet density [$\frac{kg}{m^3}$]
A_c	Cross-section coil area [m^2]
A_g	Cross-section gap area [m^2]
A_w	Cross-section wire area [m^2]
b_c	Width of cros-section coil area [m]
B_g	Magnetic field density in air-gap [T]
B_{gl}	Magnetic field density in air-gap of Lorentz force actuator [T]
B_{gr}	Magnetic field density in air-gap of reluctance force actuator [T]
B_{sat}	Magnetic field density saturation [T]
C	Actuation constant [-]
d_w	Wire diameter [m]
F_l	Lorentz force [N]
F_r	Reluctance force [N]
F_{rmax}	Maximum reluctance force [N]
FF	Fill factor round coil wires [-]
H_c	Coercivity [A/m]
h_c	Heigth of cross-section coil area [m]
i	Current [A]
J	Current density [A/m^2]
L	Self inductance [H]
l_g	Gap length [m]
l_{gm}	Minimal gap length [m]
l_s	Stroke length [m]
L_w	Total amount of wire length [m]
m_l	Mass Lorentz force actuator [kg]
m_r	Mass reluctance force actuator[kg]
n	Number of wires (coil turns) [-]
P_c	Dissipated heat in a copper wire [J]
R_{cu}	Copper resistance [Ω]
V_l	Volume Lorentz force actuator [m^3]
V_r	Volume reluctance force actuator [m^3]

I. INTRODUCTION

Future machines will require efficient, lighter and better-optimised actuators at smaller scale length. In systems with single actuation or distributed actuation, scaling is a crucial part of the design phase. On this subject, there is hardly any literature, while also no uniform scaling methodology is present at hand for conventional actuators. Katalenic [1] made an effort to evaluate the effects of scaling for actuator designs that take advantage of Lorentz and reluctance forces, but only achieved a scaling analysis based on actuator mass. In this report, I will present a study that investigates the effects of scaling Lorentz and reluctance actuators on their force performance and limitations regarding saturation and applied current. I take into account the effects of coil volume, fill factor, wire diameter, material properties and stroke lengths. This study does not consider any dynamic effects, exotic materials, Eddy currents or flux fringing. Therefore, two designs are chosen based on fixed configurations that utilise Lorentz and reluctance forces. These force principles are derived from equations, which are present in the textbook of Schmidt, entitled 'The design of high performance mechatronics' [2]. In addition, the design is parametrised using scaling factors such that proportions remain the same while the size of the actuators can be scaled through a single parameter. The scaling methodology allows evaluation of the feasibility of the systems and derivation of conclusions that may be

made by comparing the two actuators. This paper begins with the identification of the two systems in relation to their geometry and actuation principle in section II-A and II-B. Next, the systems are parameterised with a scaling variables α and β in section II-C. Then, a scaling analysis is given to explain how this methodology could be used to find the actuator performance and its limitations in section III. Thereafter, the results are interpreted in section IV. Lastly, a summary of the major steps of research is presented in a block diagram that gives a precise overview of the sequence of steps of the entire research process and is illustrated in figure 1.

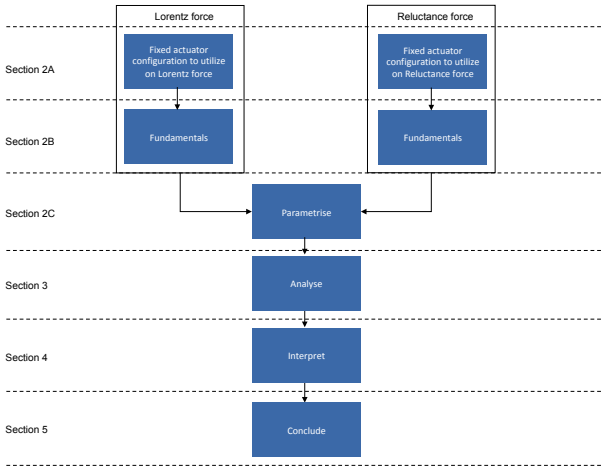

Fig. 1: Methodology flow diagram

II. Actuator Model, Fundamentals and Parametrisation

In order to evaluate scaling effects, it is first necessary to understand how actuators work and describe their behaviour in terms of parameters. Then their designs must be parametrized while allowing limitations of complexity during the evaluation of the design in the process of miniaturisation. Section II-A looks into the geometry, materials and actuation direction of actuators with an actuation principle based on a Lorentz and reluctance forces. Section II-B elaborates the electromagnetic forces derived from Maxwell's equations. Lastly, Section II-C describes the substitution of scaling parameters α and β in the geometry, force, mass and volume equations of actuator designs that use Lorentz and reluctance forces.

A. Actuator topology

The actuator configurations are named after the dominant force of each system and the view of both systems is given in side-perspective, as illustrated in figure 2 for Lorentz force actuation and figure 3 for reluctance force actuation. The configurations are fixed in order to illustrate the dominant force principle, while the other force does not play a role. Therefore, the performance of the actuator during miniaturisation is solely dependent on the configuration, materials and the input variables. This allows for comparison of both actuators. In figure 2 the stroke length is related to the translation of the current-carrying coil in the horizontal direction. Actuation of the current-carrying coil is created by the Lorentz force acting perpendicular to the magnetic flux lines of the permanent magnet.

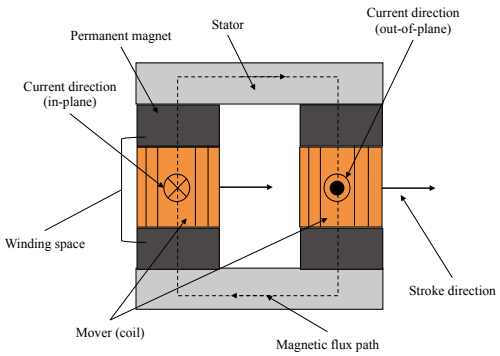

Fig. 2: Dominant Lorentz force in a fixed electromagnetic actuator configuration

For the Reluctance actuator, the stroke length is the distance of the mover to the stator as presented in figure 3. The reluctance force is an attraction force of the mover to the stator, where the force is perpendicular to the cross-section of the stator-legs and parallel to the magnetic flux path. The two actuation stroke lengths are taken into consideration during miniaturisation, as can be seen in section II-C.

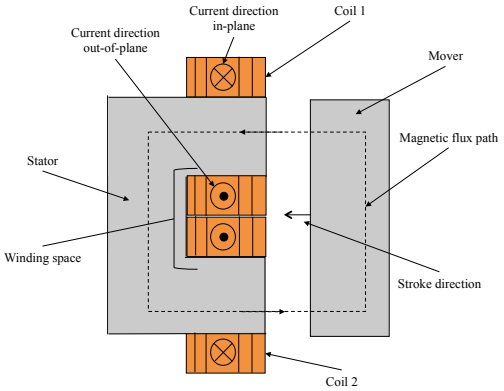

Fig. 3: Dominant reluctance force in a fixed electromagnetic actuator configuration

Representative materials and their respective properties are allocated to the various parts of the actuators illustrated in figure 2 and 3. Copper is indicated with an orange colour and has a density ρ_{cu}, a current density limit J_{cu} and wire diameter d_w. The light grey area is the ferromagnetic material iron with a density of ρ_{fe}. When iron is placed in a magnetic field it is strongly magnetized in the direction of the field and therefore often used in electromagnetic systems.

The Lorentz force actuator of figure 2 consists of additional permanent magnets indicated with a dark grey colour; these are not used in the design of the reluctance force actuator presented in figure 3. Its material is NdFeB with a density of ρ_{pm} and a coercivity H_c.

B. Fundamentals of electromagnetic actuators

In the actuator configurations of figures 2 and 3 the mechanical energy can be generated from and turned into magnetic and electrical energy. The outcome of this interaction between the electromagnetic and mechanical domain is called the electromagnetic force. The electromagnetic force takes place within the electromagnetic domain and interactions in this electromagnetic domain are described by Maxwell's equations [2]. In order to parameterise the actuator configurations of figures 2 and 3, it is necessary to understand their governing physics and formulate models that describe their dominant actuation force, while the other force does not play a role.

In their basic form, Maxwell's equations describe only the interaction of electric and magnetic fields and have to be expanded in order to take into account also the interaction of the electromagnetic domain and the mechanical domain. The general formula for the force exerted during motion of an electromagnetic actuator is F_g and consists of the input current i, the change of flux Φ_w and the self-inductance L as a function of the position x. This equation is derived from Hopkinson's law and indicates a simplified analytical model of magnetic circuits for approximate analysis of its magnetic properties [2] and can be written as:

$$F_g = ni\frac{\partial \Phi_w}{\partial x} - 0.5i^2\frac{dL(x)}{dx} \tag{1}$$

In this equation, the first term is the linear relation of the force to the current. This force is consistently present in an actuator when a current is applied. In the second term, the force is related to the squared current and is caused by the magnetic energy stored in the self-inductance L. The Lorentz force F_l of the Lorentz force actuator that has been presented in figure 2 consists of a turn n with a wire length l and can be described as:

$$F_l = 2lnB_g i \tag{2}$$

In the reluctance force actuator, there are no permanent magnets, which leads to another case. The flux Φ is only determined by the current and therefore directly related to the self-inductance L. Therefore, the reluctance force F_r exerted by the reluctance force actuator with cross-section A and magnetic permeability μ_0 presented in figure 3 can be described as:

$$F_r = \frac{A}{2\mu_0}B_g^2 \tag{3}$$

Furthermore, forces 2 and 3 are dependent on the magnetic flux Φ. This magnetic flux consists of two elements: the useful flux in the air-gap and the leakage flux, which is outside the scope of this paper. The equation for the magnetic flux density B_g is the flux Φ_g presented in the air-gap divided by the cross-section of the air-gap A_g and can be seen as:

$$B_g = \frac{\Phi_g}{A_g} \tag{4}$$

Equation 4 can be rewritten to express the magnetic field density for the two actuators of figure 2 and 3 individually. The magnetic density in the gap of the Lorentz actuator B_{gl} is generated by the coercive force H_c of a permanent magnet NdFeB as:

$$B_{gl} = 0.5\mu_0 H_c \tag{5}$$

The magnetic field density in the air-gap of the reluctance force actuator B_{gr} is generated by a current-carrying coil around the ferromagnetic yoke of the stator illustrated in figure 3 and is directly related to the ampere-turns per gap length ni and the air-gap l_g. The number of ampere-turns can also be described as the magnetomotive-force $\mathcal{F}$.

$$B_{gr} = \frac{\mu_0 ni}{2l_g} \tag{6}$$

And lastly, the heat dissipation of the wires in both systems is directly related to the coil volume. The coil volume is equal for both actuators presented in figure 2 and 3. The copper resistance $R_{cu} = \rho\frac{L_w}{A_w}$, where ρ is the copper resistivity, L_w the wire length and A_w the cross-section of the wire, is substituted in the dissipated heat equation $P = I^2R$ to derive the dissipated energy in the copper wires P_c in both actuators as:

$$P_c = R_{cu}i^2 = \rho\frac{L_w}{A_w}i^2 \tag{7}$$

C. Actuator parametrisation for miniaturisation

In order to study scaling effects on the actuators, it is in the first place necessary to describe the scaling of their configurations. Scaling parameters α and β are introduced in the Lorentz and reluctance force actuators of figure 2 and 3. The elimination of multiple parameters results in a fixed scaling model, which only depends on three elements: scaling factor α or β, the input current i, and material

properties. In order to define the relevant actuator volumes, the volume of the coil is also subjected to a scaling factor. Therefore, the coil volume scales proportionally to actuator volume as can be seen in figure 4 and 5.

1) Force scaling: Both actuator force equations 2 and 3 are constrained by the number of coil-turns in their configuration. It, therefore, is necessary to link also the number of coil-turns n to the dimension variable α or β. The cross-section A_c of both actuators equals the width b_c times the height h_c and illustrates the winding space in both actuators. In figure 4 and 5 the width b_c and height h_c for both actuators equal the given scaling parameter in width and height. Therefore, the cross-section of the wire area A_c equals α^2 in the Lorentz force actuator of figure 4 and β^2 in the reluctance actuator of figure 5. The fill-factor FF, which represents the ratio of the area of wires to the provided space consists of copper wires with a wire diameter d_w and can be written as:

$$FF = \frac{d_w^2 \frac{\pi}{4} n}{b_g h_g} \tag{8}$$

Commonly, a fill factor for round copper wires is estimated between 70% and 80% and for simplification the fill-factor FF for the link between the number of wires n, wire diameter d_w and scaling factor α or β, is chosen to be $\frac{\pi}{4}$. This relation for the Lorentz force actuator of figure 4 is written as:

$$n = \frac{\alpha^2}{d_w^2} \tag{9}$$

For the reluctance force actuator of figure 5 the scaling parameter β is substituted and can be seen as:

$$n = \frac{\beta^2}{d_w^2} \tag{10}$$

In order to get an expression of the force identified with miniaturisation, the scaling parameter has to be substituted in the equation for the magnetic flux density of equation 5 and 6 first. However, the magnetic field density B_{gl} generated by the permanent magnet of the Lorentz force actuator of figure 4 does not depend on miniaturisation. Therefore, no scaling parameter is present. Scaling parameter β and current density $J = \frac{i}{\pi(0.5 d_w)^2}$ are substituted in the magnetic flux density B_{gr} as follows:

$$B_{gr} = \frac{\mu_0 i}{2 l_g d_w^2} \beta^2 = \frac{\mu_0 J \pi}{8 l_g} \beta^2 \tag{11}$$

Furthermore, scaling parameter α is substituted in the Lorentz force equation 2 in addition to equation 5 and 9 and can be written as:

$$F_l = \frac{\mu_0 H_c}{d_w^2} \alpha^3 i = \frac{\mu_0 H_c J \pi}{4} \alpha^3 \tag{12}$$

At last, the reluctance force equation 3 can be derived from dimension variable β, equation 6 and 10 and can be written as:

$$F_r = \frac{\mu_0}{4 d_w^4} \beta^6 \frac{i^2}{l_g^2} = \frac{\mu_0 J^2 \pi^2}{64 l_g^2} \beta^6 \tag{13}$$

2) Mass and volume scaling: Moreover, equations for mass M and volume V are also linked to the same dimension parameter used in deriving the force equations 12 and 13. The mass of both systems is directly related to the material densities and the dimension variable as:

$$m_l = \alpha^3 (2\rho_{cu} + 3\rho_{Fe} + 2\rho_m) \tag{14}$$

$$m_r = \beta^3 (2\rho_{cu} + 8\rho_{Fe}) \tag{15}$$

The volume of both systems is derived from the actuator configurations of figure 4 and 5. The stroke length and air-gap are taken into account for the volume of the system. Therefore, the equations are only dependent on the dimension parameter and can be written as:

$$V_l = (27\alpha^3 + 9 l_g \alpha^2) \tag{16}$$

$$V_r = (24\beta^3 + 8 l_g \beta^2) \tag{17}$$

III. Scaling analysis

This section presents an analysis, which elaborates the consequences of miniaturisation of the actuators presented in figure 4 and 5. The volume of both actuators given with equation 16 and 17 with substituted scaling parameters α and β is varied for a range between 10^{-8} and $10^0 m^3$. Thereafter, the force performance is evaluated with respect to current i, stroke length l_s and saturation limitations.

A. Variables and parameters

For a precise comparison of both systems, the choice of design parameters related to the practical materials that are used to build electromagnetic actuators must be defined exactly. The wire diameter will be kept at $0.1mm$, the constant μ_0 at $4\pi 10^{-7}$ and the coercivity H_c of the permanent magnet NdFeB is $10^6 \frac{A}{m}$. The magnetic field density limit before saturation B_{sat} is kept at 2T. The current limit is set at the limit of the current density J for

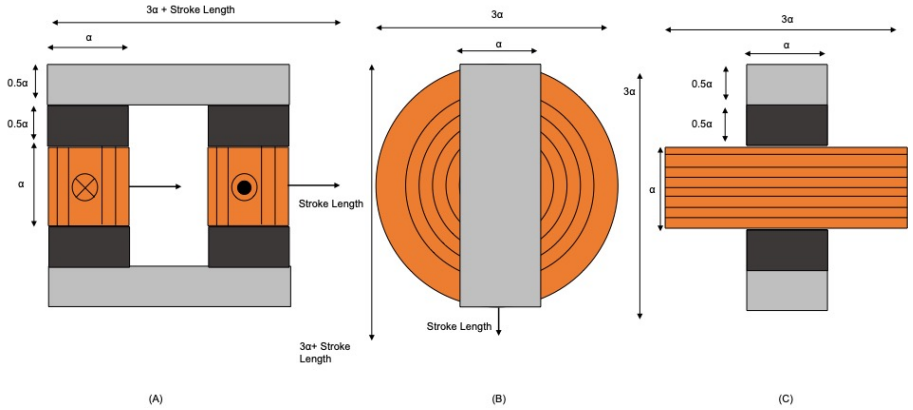

Fig. 4: Lorentz force actuator with substituted scaling parameter α. (A) Side view (B) Top view (C) Front view

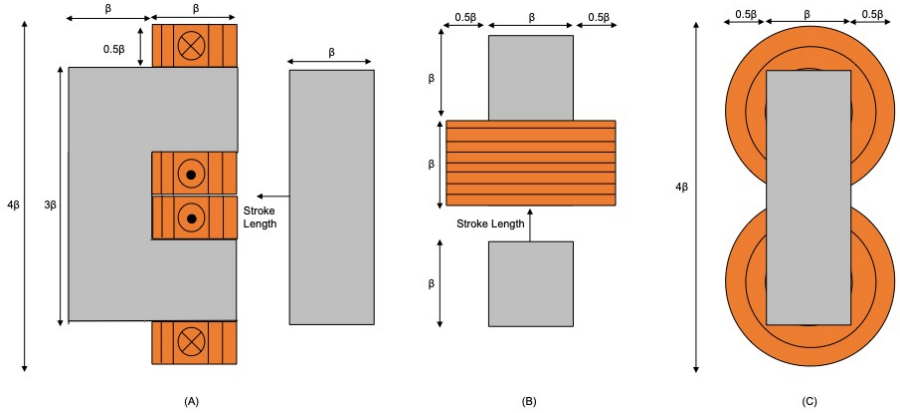

Fig. 5: Reluctance force actuator with substituted scaling parameter β. (A) Side view (B) Top view (C) Front view

a copper coil between $10 - 22\frac{A}{mm^2}$ and this implies of a maximum current range of $79 - 179mA$. The stroke length l_s indicates the deformation distance of the coil along the arrow, as is indicated in figure 4. For the reluctance actuator, the path of actuation is also presented with an arrow and implies that the mover moves towards the stator as can be seen in figure 5. It should be noted that the volume of the Lorentz force actuator given in equation 16 does not equal the volume of the reluctance actuator given with equation 17. Therefore, during miniaturisation, the scaling variable α will be larger compared to β for a given volume. In order to get a precise comparison of both systems with equal stroke length l_s scaling variable β and actuation constant C are used. Actuation constant C indicates the ratio between the stroke movement and the magnitude of the scaling parameter β during miniaturisation. Therefore, the stroke length l_s scales proportionally to the volume of the actuator. This distance l_s is the actuation constant C times the dimension variable β and is given for both systems as:

$$l_s = C\beta \tag{18}$$

In order to define the maximum force in both actuators for a stroke length l_s equation 18 has to be substituted in the force equation. In the scope of this report, no under-hung or over-hung of the coil is present in the Lorentz force actuator during actuation. Therefore, the Lorentz force of the actuator illustrated in figure 4 is constant over a certain range of l_s, which implies $\frac{dF}{dx} = 0$. For the reluctance force actuator presented in figure 5 the maximum reluctance force at the end of a stroke movement is expressed as F_{rmax} and consists of the substitution of equation 18 into equation 3 as:

$$F_{rmax} = \frac{\mu_0}{4d_w^4}\beta^6\frac{i^2}{l_g^2} = \frac{\mu_0 J^2\pi^2}{64l_g^2}\beta^6 = \frac{\mu_0 J^2\pi^2}{64C^2}\beta^4 \tag{19}$$

The actuation constant C is 0.1 for further analysis. This is a reasonable assumption for the ratio between the stroke movement and the magnitude of scaling parameter β.

B. Maximum achievable force per volume

In this section, the maximum force output for a volume range between 10^{-8} and $10^0 m^3$ is given in graph 6. A comparison is made between the Lorentz force and the reluctance force actuator. The reluctance force actuator is studied in an open position. Therefore, the force of equation 19 equals the attraction force of the mover to

the stator with a gap value l_s as can be seen in figure 5. In graph 6 the preferable actuator is given for specific scale regions. Since the current i and actuation constant C can influence the performance of both actuators, a vertical line is presented in graph 6 to indicate the intersection point.

Firstly the correct values of α and β are required for this comparison. Given the value for the volume, the two dimension-variables α and β can be derived from equations 16 and 17. Given the fixed geometries in the x,y and z-directions and having calculated α and β, it is now possible to identify the size of the actuator at smaller volumes as well as the related maximum achievable force. Now as an example of shifting the intersection point the current is increased with $100mA$ in graph 7. Shifting of the old intersection indicated with the dotted vertical line to the left is due to its steeper slope. One observes that the reluctance actuator in comparison with the Lorentz force actuator benefits more from such an increase of current.

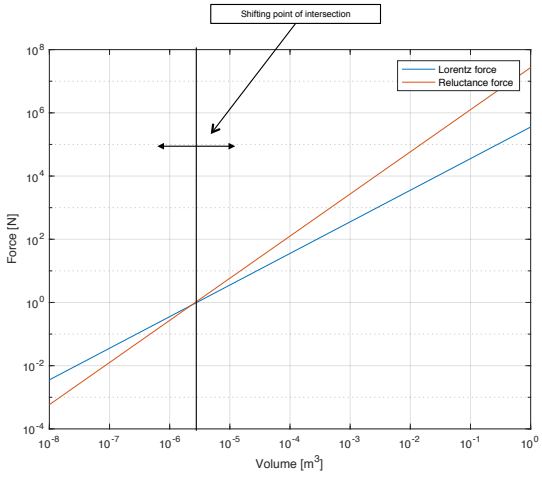

Fig. 6: Force per volume Lorentz and reluctance force actuator: maximum force with shifting point of intersection

Also, as an example, the point of intersection may be shifted by altering the actuation constant C. Increasing constant C to 0.15 indicates an increase of stroke length l_s. It should be noted that the Lorentz force is constant over a range of l_s. Therefore, it is not influenced by different values of C. However, the maximum achievable force of the reluctance force actuator will decrease as can be seen in A of figure 8. The opposite happens when the stroke length is decreased to $C = 0.05$, meaning that the stroke length is only one-twentieth of variable β. The maximum obtainable force would be higher due to a smaller gap distance as presented in B of graph 8.

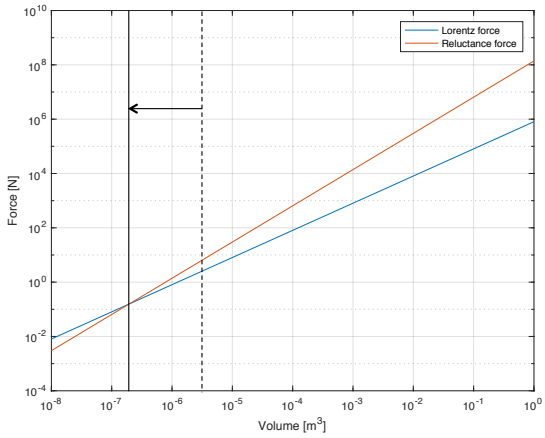

Fig. 7: Force per volume Lorentz and reluctance force actuator: maximum force with shifted point of intersection due to current increase

C. Gap limitation in reluctance force actuators

In this section, only the reluctance force actuator is examined, because the Lorentz force actuator does not exhibit a varying air-gap l_g. The force performance F_{rmax} of the reluctance actuator is limited by two factors. Firstly, there is the limitation of current input i due to the heat dissipation inside the coil. If the dissipation is too large the coil will melt. Secondly, the current limitation is not exceeded, yet the iron stator can be saturated. In figure 9 it is shown how the reluctance force reaches its saturation limit as is indicated by the dotted line. After this point, the reluctance force system is not capable of coping with the maximum current input. The desired stroke length l_s then can not be obtained and thus would the expected maximum force be lower than the red curve in figure 9 indicates.

D. Mechanical work for a single stroke in a reluctance force actuator

In order to see how much mechanical work has been done in a system, the area under the curve in a force-displacement graph has to be calculated. An analysis has been conducted to acquire the magnitude of the Lorentz force and the reluctance force to achieve a given stroke displacement. The volumes V_l and V_r are $1mm^3$,$1cm^3$ and $1dm^3$. The stroke length magnitude then consists of a minimum value of the air-gap l_{gm} between the stator and mover of the reluctance force actuator in figure 5. This minimum value is set to be one-twentieth of scaling parameter β in order to avoid high force values near closed air-gap values. The maximum value of the stroke length equals l_s and therefore equation for the displacement of the stroke length l_{s2} can be written as:

$$l_{s2} = (C - 1/20)\beta \tag{20}$$

This illustrates a stroke length of 0.05β for a chosen C of 0.1 and is given in graph 10. The blue line indicates

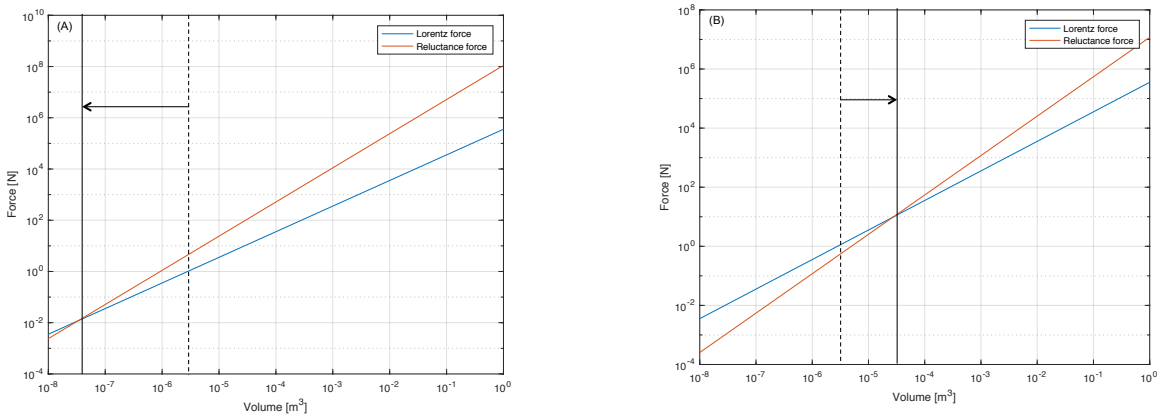

Fig. 8: Force per volume Lorentz and reluctance force actuator: Maximum force with varying actuation constant C. (A) $C = 0.05$ (B) $C = 0.15$

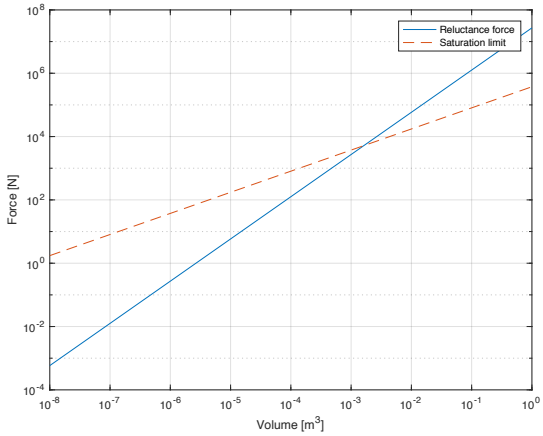

Fig. 9: Force per volume reluctance force actuator: saturation limit

the Lorentz force for a current input of $179mA$. The value of the input current implies the upper boundary of the maximum current as mentioned in section III-A. The red line indicates the reluctance force for a current input of $179mA$, be it at a fastly reducing output force. The outcome of the mechanical work under the solid region of the curve line is given in list below:

1) The mechanical work for a volume of $1mm^3$
   a) W_{lor} = 1.4e-8J
   b) W_{rel} = 4.8e-9J
2) The mechanical work for a volume of $1cm^3$
   a) W_{lor} = 1.4e-4J
   b) W_{rel} = 4.8e-4J
3) The mechanical work for a volume of $1dm^3$
   a) W_{lor} = 1.4J
   b) W_{rel} = 48J

E. Dissipation

In small systems, heat dissipation becomes a critical issue. Heat dissipation in electromagnetic actuators is the heat transfer of the current-carrying wires to the surrounding objects and environment. In this project, a fixed wire-diameter d_w, as well as a constant copper resistance ρ, have been adopted as assumptions. Therefore, the dimensions of the coil area A_c could only influence the number of coils n. This lead to the conclusion that the scaling variables α and β are directly related to the number of coils n. The amount of dissipated energy in a reluctance force actuator is relatively higher as can be seen in figure 11 which is related to the higher ratio of coil-volume to actuator volume of the reluctance force actuator in comparison to the Lorentz force actuator.

IV. Discussion

In this research project, a methodology has been developed for two electromagnetic actuators with designs that make use of Lorentz and reluctance forces, in order to identify scaling effects. Currently, different scaling principles are mostly design-specific and insufficient attention is given to general scaling principles. The undertaking of a feasibility study and the application of comparative analysis to conventional electromagnetic actuators may yield benefits to advance development and the utilisation of these electromagnetic actuators in complex systems.

One of the most critical aspects of an electromagnetic actuator is the relation between the current input and the actuator performance. In this study, the wires, coil area and materials are specified and related to the same scaling parameter of the configuration and therefore also affected by miniaturisation. It is assumed that the relative permeability μ_r of the copper material, the permanent magnet and air components are all equal to 1; in accordance with a value that assumed in numerous studies and textbooks in this

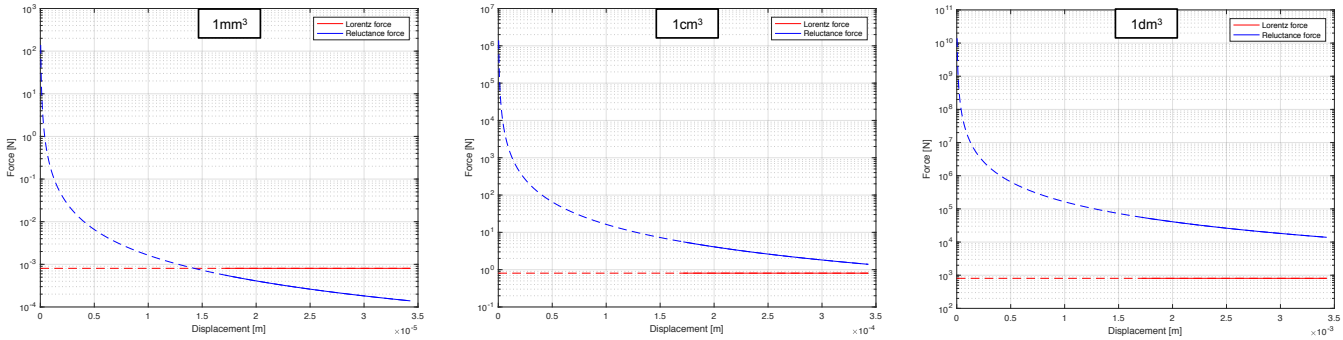

Fig. 10: Force per displacement for an actuation stroke in a Lorentz force and reluctance force actuator, whereas the solid part of the curve indicates the actuation displacement. Actuator volume of 1 cubic millimeter (left), actuator volume of 1 cubic centimeter (middle), actuator volume of 1 cubic decimeter (right)

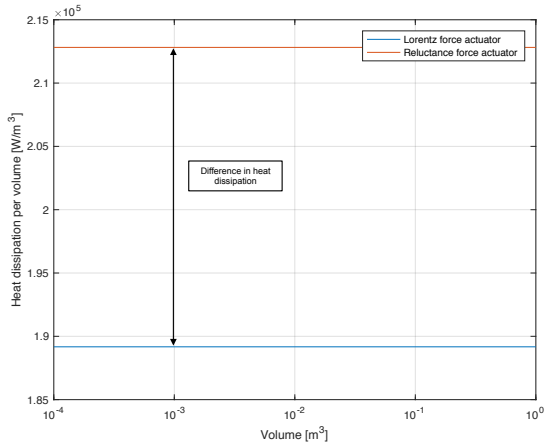

Fig. 11: Heat dissipation in a Lorentz and a reluctance force actuator

field [2]. Also, the coercivity H_c of the NdFeB permanent magnet in the Lorentz force actuator and the saturation limit B_{sat} in the iron parts of the reluctance actuator remain constant during the scaling analysis. Regarding the system, it is assumed that there are no mechanical deformations during actuation, nor fluctuations over time of the input current.

The stroke limit is dependent on the range of length l_s and must be kept within the limiting boundaries of both actuators. For a Lorentz force actuator, it has been assumed that $\frac{dF_l}{dx} = 0$, which implies that the force remains constant during actuation. However, phenomena like coil over-hung and under-hung can greatly affect the force performance of a Lorentz force actuator and may reduce output forces F_l. Another assumption is that both systems are considered as quasi-static actuators. And therefore hysteresis will not be taken into account because no significant frequency changes in the magnetic domain of the ferromagnetic stator are considered. The magnetic flux density distribution is assumed homogeneous throughout the magnetic circuit of both actuators; Eddy currents are not taken into consideration, neither is the unwanted fringing of the magnetic flux examined in this study, both imply major analytical hurdles, therefore also finite element analyses would have to be examined. Our approach to develop a methodology to evaluate scaling effects is restricted to only two conventional actuator configurations. Subsequent research might focus on the introduction of more scaling variables, such as implementing different scaling variables along the x,y and z-axis. New insights then may be gained on design optimization concerning the trade-off of between the magnetomotive-force $\mathcal{F}$ and the saturation limit B_{sat}.

V. Conclusion

In this research paper, dimensional scaling effects regarding the performance of the Lorentz and reluctance actuator have been examined. Deeper insight thus could be acquired into the feasibility and performance of two distinct design configurations. This methodology could be highly relevant in furthering the utilisation of electromagnetic actuators in complex systems. For instance, this scaling study shows the force-displacement performance of a Lorentz force and reluctance force actuator for equal actuator volume, the input current of $178mA$ and a stroke of l_{s2}. Results clearly show that if actuator volume is adjusted, actuator preference regarding mechanical energy may differ. Already beforehand decisions can be made which reduce time-consuming element analyses or processes of actuator performance feasibility for further investigation. Given the scope of this research project, aspects of magnetic flux could not be taken into account. Further steps in research on utilisation of electromagnetic actuators in the centimeter-scale region would need to include finite element modulation and extensive additional experimental analysis.

References

[1] A. Katalenic, *Control of reluctance actuators for high-precision positioning*. No. april, 2013.

[2] R. M. Schmidt, G. Schitter, and J. van Eijk, *The design of high performance mechatronics*. 2011.

4

Paper 3: Activating metamaterials with electromagnetic actuators

Active metamaterials: unit cells for tunable damping

Dexter Thomas
Departement of Precision and Microsystems Engineering
Delft University of Technology
Mekelweg 2, 2628CD, Delft, the Netherlands

***Abstract*— The novel scientific field of mechanical metamaterials refers to artificial structures and their mechanical properties, which are a function of their meso-scale geometry as well as their unit cell structure. Therefore, an artificial combination of properties can be created which is infeasible when the common materials are considered on their own. Metamaterials are constrained in that the mechanical properties are tailored yet fixed. However, after activation metamaterials can be controlled and mechanical properties could be influenced. Such active metamaterials with properties like tunable damping and stiffness, as well as lightweight structures, could enable a host of novel applications, which might benefit greatly from tunable mechanical properties. In this study, an innovative metamaterial cell is examined with respect to controlled damping. A demonstrator is realised in order to experimentally investigate its behaviour under mechanical loading. The outcome of Coulomb damping for an unit cell showed a value of 1.2e-2J per cycle at 24V. Thereby, a damping ratio of 0.34 between damped and stored energy has been verified. This project holds strong promise for the feasibility of tuning damping in centimeter-scale unit cells.**

NOMENCLATURE

δ_{yy}	Total deformation in y-direction $[m]$
η	Loss factor $[-]$
F	Magnetomotive force [At]
μ_0	Vacuum permeability $[H/m]$
μ_f	Friction constant $[-]$
Ψ	Damping coefficient $[-]$
θ	Angle of diagonal beam with y-axis $[^\circ]$
ε	Strain ratio in y-direction $[-]$
ξ	Damping ratio $[-]$
A_1	Cross section diagonal beam $[m^2]$
A_2	Cross section vertical beam $[m^2]$
A_g	Cross section magnetic density field area $[m^2]$
b	Depth unit cell $[m]$
B_g	Magnetic field density $[T]$
d_m	Diameter electromagnetic actuator $[m]$
E_1	Young's modulus diagonal beam $[Pa]$
E_2	Young's modulus vertical beam $[Pa]$
F_e	Applied force $[N]$
F_f	Friction force between actuator and plate $[N]$
F_m	Magnetic attraction force $[N]$
I	Area moment of inertia $[m^4]$
i	Electrical input current $[A]$
l_g	Air-gap length $[m]$
l_s	Sliding distance $[m]$
L_y	Total unit cell length in y-direction $[m]$
M	Bending moment $[Nm]$
n	Number of wire-turns $[-]$
t_1	Thickness diagonal beam $[m]$
t_2	Thickness vertical beam $[m]$
U_d	Dissipated energy during cyclic motion $[J]$
U_e	Elastic strain energy $[J]$
U_s	Stored energy during loading $[J]$
W_f	Work done by friction $[J]$

I. INTRODUCTION

Mechanical metamaterials refer to a domain of artificial structures and belong to the family of metamaterials. The concept of a metamaterial has been extended from electromagnetics and acoustics to the field of mechanics. Metamaterials have material properties which are related to the unit cell structure instead of the composition [1], [2]. Artificial metamaterial structures, therefore, can exhibit exotic properties. Structures such as auxetic materials have a negative Poisson's ratio [3]. Other structures can express a vanishing shear modulus such as in pentamode structures [4],[5] or have a negative compressibility [6]. The analysis of a unit cell from a mechanical engineering perspective is related to the stiffness, rigidity and compression of a structure. In a metamaterial unit cell, these three components are linked to 4 elastic constants [7]: Young's modulus E, shear modulus G, bulk modulus K and Poisson's ratio ν. These constants are core elements of the design principles for mechanical metamaterial structures.

Unfortunately, metamaterials are constrained in that the mechanical properties are precisely defined and fixed; alteration of these properties simply is not feasible. However, if activated, metamaterials can be controlled and mechanical properties can be influenced with resulting variable properties. Therefore, one aims at achieving the benefits of conventional mechanical properties such as high damping properties. For example, materials like 3M VEM viscoelastic damping polymer materials exhibit loss factors η up to 1.1 and are used in vibration damping devices. However current devices have shortcomings in impact resistance, rapid attenuation and lack of local damping capabilities [8], [9]. Metamaterials, which could exhibit tunable damping and adjustable stiffness, can adapt to rapid variations in externally applied loads, can have quick control response, as well as can consists of a lightweight structure. High-tech, automotive and aerospace industries could greatly benefit from tunable mechanical properties in

morphing, dynamic and vibrational isolation applications [10].

In the current literature, one finds a small number of reports towards activation of metamaterials. Poon et al. [11] investigated achievable tunable stiffness properties with phase-changing unit cells. These unit cells consist of silicone rubber spheres with integrated gallium cores. Multiple unit cells form a cubic lattice at meso-scale level. Heating the core and thereby melting the gallium creates a stiffness reduction in the lattice of the cubic structure. They successfully demonstrated a concept design with a stress-strain behaviour consisting of a rate of 3.7 times increasing stiffness at 7% strain. But such active metamaterials have a limited response time due to liquefaction and solidification limits. Numerous studies on self-folding origami structures can be classified as efforts towards making active metamaterial structures. Overvelde et al. [12] studied mechanical metamaterials whose shape, volume and stiffness can be controlled with the use of pressurized air-pockets in the hinges of the metamaterial unit cell structure. They connected unit cells in order to form a periodic structure, which generates an extruded cube. Different stress-strain behaviour for different orientations during uni-axial compression was found by them. They, also, reported limitations concerning activation reported and tunability of the unit cells. Other activation principles in origami structures have been studied by Li et al. [13]. They investigated morphing and stiffness variation in active origami metamaterials unit cells. They created five different unit cell configurations each with an effective stiffness characteristic. These different configurations are the result of the relationship between the internal fluid volume and the structure deformation of kinematic folding techniques. They realised an adaptive fluidic origami demonstrator concept but reported limited performance in variable stiffness and the unit cells structures were too complex for scaling. Hagpanah et al. [14] investigated damping in mechanical metamaterial structures. They demonstrated a concept design based on locking-mechanisms consisting of electromagnets and screw pins. They achieved a gradual stress drop of 3KPa, which then lead to constant force behaviour with a resolution of 0.1KPa. Their prototypes suffered from performance degradation during miniaturisation, as well as form difficult to control continuous behaviour.

Another method of activating metamaterials is the integration of smart materials. These active composites convert energy between electrical and mechanical domains and can be divided into two categories according to Kornbluh et al. [10]. The first group is using the material in structures as active components. These are intrinsically adaptive materials and change of external stimuli can alter their mechanical properties; these include materials such as shape memory alloys, thermal elastomers and various ionic gels. The second group consists of materials which act as energy transducers in order to modulate the properties. Examples include dielectric elastomers, piezoelectric materials or magnetostrictive materials. Smart material utilisation is limited by challenges caused by integration, performance and robustness. Active composites need external stimuli for proper functioning, and as a result integration into complex structures and activating them locally can become difficult. Most of these applications do not possess the inherent range that is required at a meso-scale level. They also lack robustness in dynamic structures since the specific placement prevents proper functioning. Lastly, certain intrinsic materials such as liquid crystal elastomers or mechano-chemical gels are sensitive to changes in temperature and are therefore neither chemically nor environmentally sufficient stable. In conclusion, it may be stated that composites are currently insufficiently developed to permit for implementation in mechanical metamaterials.

While smart materials make steady progress, already at present, activation of mechanical metamaterials can be achieved by exploiting electromagnetic actuators. Conventional electromagnetic actuators, namely, are well known for macro-scale applications due to their efficiency and high force densities; yet, they are less adopted in the subcentimeter-scale region. The few use cases of application in the centimetre-scale region are deformable mirrors for adaptive optics [15] and hearing aid devices [16], [17].

This research project presents an active metamaterial unit cell design in order to bring forward metamaterial lattices with a local tunable damping coefficient. Electromagnetic tuning, namely, provides a range material damping from near-perfect elastic till damped behaviour. The modelling of this design for achieving the desired metamaterial stiffness profile as well as the realisation of damping capabilities is explained in section II. Next, a cell prototype is constructed and the experimental setups are explained in section III. Then, in section IV, follow the research outcomes with measurements of force-displacement behaviour, loss-storage ratio, and tunability of the latter. The results are further elaborated and discussed in section V.

II. Cell analysis

The main objective of this research project is to succeed in creating an active mechanical metamaterial unit cell. This study exploits electromagnetic actuators as activators. The focus is on the utilisation of reluctance actuators to realise active damping that, in real-time, is electrically controlled. This requires a design that effectively assesses how reluctance actuators function in order to create a tunable damping cell. First, the electromagnet of the proposed cell is introduced in section II-A. Next, the design and actuation principle are introduced in section II-B. And lastly section II-C gives a comprehensive definition of how the design can be modelled to achieve the desired metamaterial stiffness profile as well as the resolution of damping capabilities.

A. Electromagnetic actuator

Miniaturisation of electromagnetic actuators in the subcentimeter-scale region only has been researched in a limited manner, and scaling has not been investigated in a uniform format. Mostly, miniaturisation has been explored for specific actuator configurations [18], [19], [20]. The electromagnetic force present in such actuators is derived from the macroscopic formulation principles of electromagnetism and from physics phenomena, which are associated with electric and magnetic fields and their interaction [21]. It is well known that scaling of electromagnetic actuators with respect to these forces does not behave in a linear manner. This characteristic implies that in the cubic centimeter region conventional actuators, which use Lorentz forces are inferior to those that exploit reluctance forces. The selected design of the reluctance force actuator for our study is presented in A of figure 1. The direction of the force when activated is an attractive force towards the stator. This force is triggered by a current flow in the coil of the electromagnet as can be seen in B of figure 1.

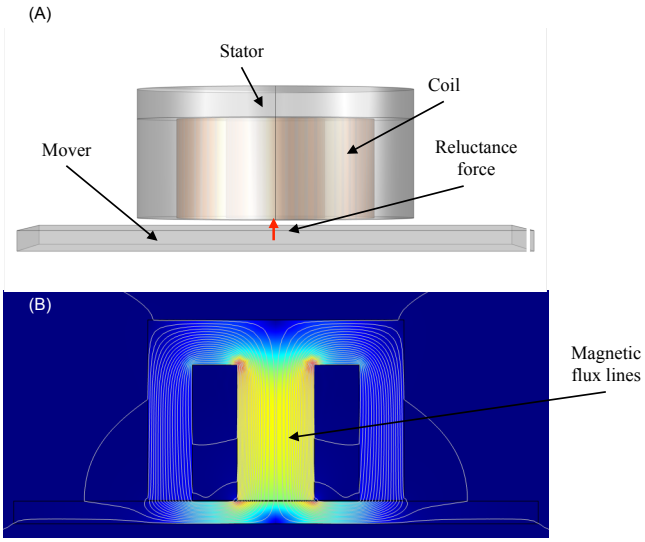

Fig. 1: Reluctance force actuator. (A) Design and force direction between stator and mover, (B) Finite element analysis of reluctance force actuator with generated magnetic flux inside the coil

B. Cell design and actuation

This research project proposes a unit cell design for tunable damping in mechanical metamaterials. The design is shown in figure 2 and consists of 4 nodes linked together with 4 flexural beams under a 90° angle. Two support beams are attached to the west and east node of the unit cell and are used to support the reluctance actuator of figure 1. Under uni-axial deformations in the vertical or horizontal direction, the flexures behave symmetrically and deform equally. Therefore, under compressive strain, loading would create a bending moment in the flexural beams of the lattice structure. The selected reluctance force actuator consists of a stator and a mover segment. In our design, the stator is fixed to the west node, whereas the mover is fixed to the east node. When voltage is applied, magnetic field B is generated and the stator pulls the mover with a force. Again, under uni-axial deformations in the vertical or horizontal direction, a sliding movement of the stator over the mover component is induced. This sliding deformation generates a dry friction component also called Coulomb damping.

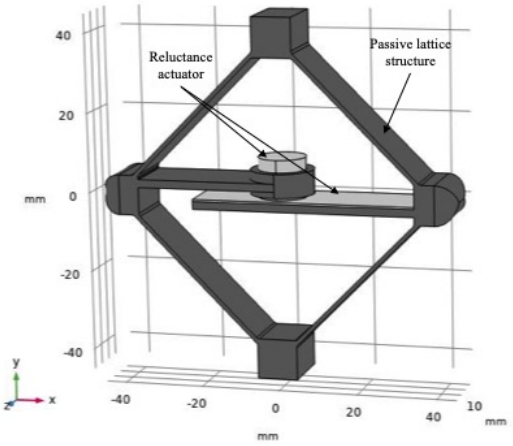

Fig. 2: Proposed cell design for controllable damping in active mechanical metamaterials

C. Modelling

Modelling is required to achieve the desired metamaterial stiffness profile and the resolution of the damping capability. First, section II-C.1 describes the parameters used in the unit cell design of figure 2. Thereafter, section II-C.2 addresses elastic behaviour and section II-C.3 studies the damping portion in the cell. These analytical models are based on the principles of strain energy and dissipated energy respectively. Further investigations regarding yield limitations are given in a finite element analysis, which furthermore permits examination of the design in terms of elasticity and plastic deformations. Lastly, to characterize damping performance, the ratio between dissipated energy U_d and stored energy U_s in section II-C.4 is calculated.

1) Parametrisation: The design introduced in section II-B, and in figure 2 is parametrised as shown in figure 3. The depth of the structure b, the thickness t_1,t_2 and the lengths L_1,L_2 are related to the beam structure of the cell. The flexures form a square geometry with a 45° angle regarding the vertical axis. The cross-sections of the flexures are $A_1 = t_1 b$ and $A_2 = t_2 b$. The lattice structure has a uniform Young's modulus E. The area moment of inertia for the beam structure is given with $I = \frac{bt^3}{12}$. The total length of the unit cell in the y-direction l_y is derived with the equation:

$$L_y = 2(L_1 cos(\theta) + L_2) \tag{1}$$

And the deformation in the y-direction is δ_{yy}. Therefore, the strain ratio of the unit cell can be written as:

$$\varepsilon_u = \frac{\delta_{yy}}{L_y} \tag{2}$$

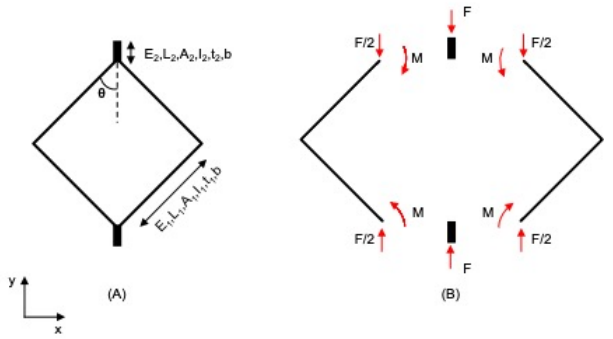

Fig. 3: Lattice structure schematic. (A) Parameters, (B) Free body diagram

2) Elastic strain energy calculation: A bending moment M created by an external force and applied to the unit cell generates strain energy in the beam flexures of the structure; this can be seen as:

$$M = -\frac{1}{4}FL1sin(\theta) \tag{3}$$

Deformation along the y-axis δ_{yy} is a function of the geometry parameters and the applied force F presented in figure 3. This function is explained in the support manual of the study by Haghpanah et al [14] and can be seen as:

$$\delta_{yy} = \frac{F}{b}\left(\frac{2}{E_2 * (\frac{t2}{L2})} + \frac{cos(\theta)^2}{E_1(\frac{t_1}{L_1})} + \frac{sin(\theta)^2}{E_1(\frac{t_1}{L_1})^3}\right) \tag{4}$$

Both, equation 3 and 4, are used to derive the elastic strain energy U_e. This equation is a function of the geometry parameters, the applied force F and the internal moment M. The first two parts of the equation represent the axial strain energy along the y-axis and the last part of the equation is the bending strain energy generated by a bending moment and can be seen as:

$$U_e = \frac{L_2F^2}{E_2A_2} + \frac{L_1cos^2(\theta)F^2}{2E_1A_1} + \int_0^{L_1} \frac{2(M+(F/2)xsin(\theta))^2}{E_1I_1}dx \tag{5}$$

In the unit cell design of figure 2, the strain energy stored in the lattice during a loading cycle is $U_s = U_{e1} + U_{e2}$. It consists of compressive loading U_{e1} and stretching U_{e2}.

To compensate for the shortcomings of the analytical model, a finite element model has been analysed to take into account the deformation behaviour as seen in figure 4;

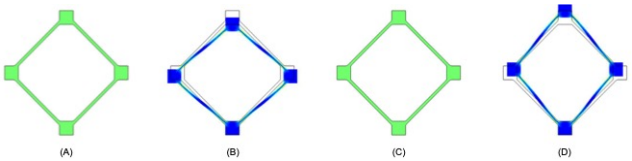

Fig. 4: Lattice structure during cyclic motion. (A) Undeformed, (B) Compressed, (C) Undeformed, (D) Stretched

It indicates the yield stress during deformation.

3) Coulomb damping calculation: The controllable damping in our active metamaterial cell design is realised through Coulomb friction, which is regulated by a voltage that is applied to the reluctance actuator. The coil consisting of ni ampere-turns inside the actuator generates a magnetic field B. Together with magnetic permeability μ_0, and cross-section A_g and a roughly constant air-gap l_g this magnetic field will yield a reluctance force F_r. This is a derivative of the Maxwell equations [22] and can be written as:

$$F_m = (\frac{ni}{l_g})^2\frac{\mu_0 A_g}{4} \approx \frac{B_g^2 A_g}{\mu_0} \tag{6}$$

The resulting damping force F_f in our cell design is the result of contact friction between the stator and mover as presented in figure 1. Therefore, the force F_f depends on the force of the magnet F_m and the friction coefficient μ_f as:

$$F_f = \mu_f F_m \tag{7}$$

In the prototype, when deformed, the stator and mover move in opposite-direction at a specified distance $l_s = 4\delta_{yy}$ as can be seen in figure 2 and the resulting dissipated energy W_F can be seen as:

$$W_f = F_f l_s \tag{8}$$

4) Damping coefficient: The demonstrator is a combination of the electromagnet (Coulomb damping) and lattice structure (stored strain energy). In order to characterise damping performance a damping coefficient Ψ is introduced. This is a ratio between dissipated energy U_d and stored energy U_s over a single cycle of periodic deformation and can be written as:

$$\Psi = \frac{U_d}{U_s} \tag{9}$$

The damping coefficient Ψ can be linked to related damping factors. In order to compare the damping coefficient in terms of the loss factor η, a multiplication of 2π is necessary. Furthermore, the level of damping relative

to the critical damping given with damping ratio ξ [23], equals the damping coefficient Ψ over 4π.

III. Materials and methods

In this section the procedure to realise an active unit cell and the investigation of components of which the active unit cell consists are studied. First, the metamaterial unit cell is developed in section III-A. Then follows the construction of the unit cell lattice, where the assembly, structure and material are of great importance for the amount of stored strain energy as is described in section III-A.1. Next, the synthesis of the electromagnet and the electrical steel sheet – called stator and mover – serves to dissipate energy in the unit cell and is given in section III-A.2.

Experimental validation, given in section III-B aims at measuring stress-strain behaviour, loss-storage ratio and tunability of the latter. Section III-B.1 explains the experimental setup for measuring force-displacement curves and energy dissipation under quasi-static deformations. Section III-B.2 then specifies the composition for experimentally testing the active unit cell under cyclic motions of compressive and stretching deformations that includes the use of a tensile bench framework. All the obtained data will be processed and plotted in a computational environment and further evaluated in the results section.

A. Realisation of a tunable active unit cell

The methodology of obtaining an active unit cell is of great importance to understand the impact of the behaviour of the system on its tunability. Therefore, a distinction is made between the metamaterial structure and the actuator. The fabrication steps are elaborated for each component starting with the passive structure in section III-A.1 and the electromagnet in section III-A.2.

1) Manufacturing of the passive structure: Our metamaterial unit cell structure exhibits the desired elastic behaviour as described in figure 4 and accommodates the actuator in figure 2 of section II-B. As a result, the cell structure should only exhibit elastic behaviour with the desired stiffness and without viscoelasticity. For practical efficiency, we use additive manufacturing to assemble our unit cells. The analytical modelling of section II-C has served to decide on a fitting material and a flexure thickness for the stiffness profile, while finite element analysis is used to keep deformations below plasticity.

For manufacturing of the unit cell, we use Prusa i3 MK3S and Prusa SL1 printers. The first is a fused deposition modelling 3D printer using a continuous filament of a thermoplastic material. This enables printing of PLA (polylactic acid), ABS (Acrylonitrile butadiene styrene), PETG (polyethylene terephthalate glycol) and Flex (flexible rubbers). The latter is a printer based on the MSLA (proprietary liquid crystal mask technology) printing process. MSLA utilises an LED array as its light source together with a mask to shape the printed image. No filament is used and the common print materials at our disposal are UV sensitive liquid resins.

The lattice of the 90mm unit cell with the design of figure 2 is printed with a filament of PLA. This material exhibits a 1.2 g/cm^3 and a flexural strength of 95MPA. The strain break at resistance is 160%. The unit cell dimensions include a height and width of 90mm. The depth is constrained to the diameter of the reluctance actuator as will be explained in the following section III-A.2 to fit inside the unit cell, which is 16mm. The surface of the support beam attached to the right node of the unit cell - as can be seen in figure 2 - equals the surface of the electrical sheet material A of figure 6. The thickness t of the flexures is 1mm and the realised unit cells are illustrated in Figure 7. For the integration of the electromagnetic actuator - see figure 1 - a clamping component of the flex45 material has been used.

The miniaturised lattice structure is scaled with a factor 1:2 and is printed with a Prusa SL1 printer due to its higher resolution. The mechanical properties of the resin are closely related to PLA and ABS material with a bulk modulus of 2.7GPa. The unit cell dimensions include a height and width of 45mm. The depth is also constrained to the diameter of the reluctance actuator as will be explained in the following section III-A.2, which is 8mm. The thickness t of the flexures are 0.5mm. Due to its scaled size and limited space for fitting a clamped system, a design similar to an u-shape has been printed instead. This clamping design tolerates a modest portion of bending for clamping the magnet and leaves it fixed without the necessity of adding fitting components. The assembled unit cells are illustrated in B of figure 7.

2) Reluctance actuator: Our unit cell design 2 utilises a reluctance force to achieve tunable damping as can be seen in section II-C.4. This permits direct control of friction force F_r. In this study, the actuator consists of a commercial stator and a manufactured electrical steel mover.

The electromagnetic actuators - see figure 5 - are used to accommodate the dissipated energy component. The electromagnetic actuator is activated with a power supply and regulating the input feed then can alter the magnitude of the attraction force.

The mover can be seen in the design which is pictured in A of figure 1 in section II-A. This mover has been laser-cut from a 0.5mm thick electrical steel plate with high magnetic permeability illustrated in figure 6. Electrical steel has been chosen as the material because of its low resistance to conduct magnetic fields. Therefore, an attraction force is generated between the electromagnet and electrical steel

sheet due to the magnetic flux which has been created inside the core of the current-carrying coil and this flow path through the mover has been simulated in B of figure 1.

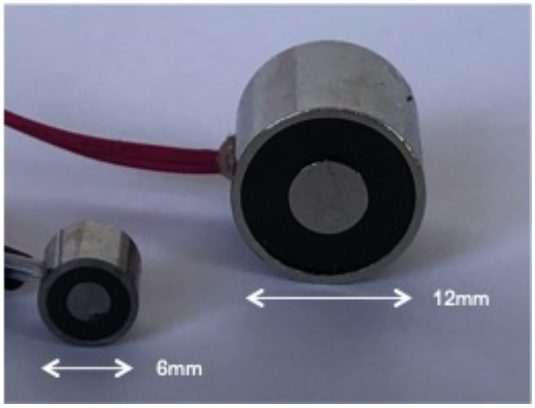

Fig. 5: Electromagnetic actuators

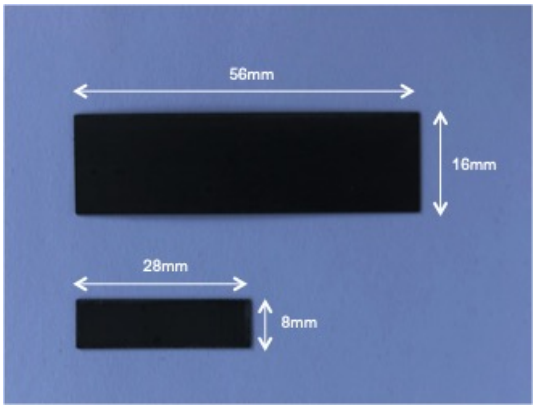

Fig. 6: Electrical steel sheets that serve as movers for actuators in figure 5

B. Experimental validation

The main objective of experimentally validating the active unit cell is to indicate the tunable damping behaviour in practice. The first experiment measures the force-displacement curves for the passive lattice structure as a result of external applied deformations. Thereafter, the second experiment measures tunability of the dissipated energy in response to sliding deformation of the reluctance actuator. Lastly, the whole active unit cell is being measured during cyclic loading. For these experiments we use a quasi-static setup with low strain rates as discussed in section III-B.1 and a setup that includes a vertical tensile bench in section III-B.2.

1) Experimental setup for quasi-static deformations: An experimental arrangement for measuring stress-strain curves and energy dissipation under quasi-static loading deformations is shown in the diagram of 8; the manner in which this setup can be applied is shown in figure 9. The setup consists of stationary and mobile portions. The stationary part consists of the aluminium framework, whereas the mobile part consists of a motorised stage and accommodates the force sensor. During the experiments, the specimen is attached to the mobile stage. This part is connected with a force sensor on one end, and the stationary framework on the other end. The force sensor is powered by a low-profile stage with ball-screw drives. Motorised stage control inputs and sensor outputs are connected to a USB-6215 multifunction DAQ device that allows controlling the experiments in a PC with a Labview environment. A transistor and a second USB-6215 multifunction DAQ device have been placed between the power-supply and electromagnet and is a requirement for controlling the electromagnetic actuator with a secondary Laptop with Labview environment.

The setup in figure 9 is being used to conduct experiments to characterise the behaviour of the individual components of the unit cell. Firstly, experiments measure the elastic strain energy stored in the unit cell structure with, as yet, no activation. In figure 9 the passive structure is placed in the dashed squared box. Now, the lattice structure is clamped at the south node of the model, whereas the north node is attached to the force sensor with a M3 lead-screw. The clamped lattice is constrained to 1 DOF along the axis of the translation stage.

In the second experiment, the same setup is used. However, the friction force during sliding deformation was tested. The electromagnet – integrated into a harness as is illustrated in figure 10 - is attached to the force sensor of the setup in the dashed squared box in figure 9. The additional power-supply control presented in diagram 8 is used to control the electromagnet. In order to prevent overheating of the coil wires in the electromagnet when active, a Labview interface with a pulse width modulation script was operated in order to regulate the electromagnetic actuator for the entire duration of the experiment.

2) Experimental setup for cyclic loading measurements: The last experimental setup measures the behaviour of the active unit cell under cyclic loading and is presented in the diagram of figure 11. Since the unit cell is a combination of the passive structure and the reluctance actuator, this experiment is the final stage of this study. Now, both behaviours are studied collectively and initiate electrical control of dissipated energy during cyclic motion.

In this experiment, a setup as is illustrated in figure 12 is used. The unit cell is clamped at the south and north nodes of the lattice. The test setup consists of an integrated force sensor in the moving part of the upper clamp, a power supply, control interface and a clamping stator. All data that have been extracted are presented in 3 columns displacement (m), time (s) and force (N). The text files have been transferred to Excel files and can be read with

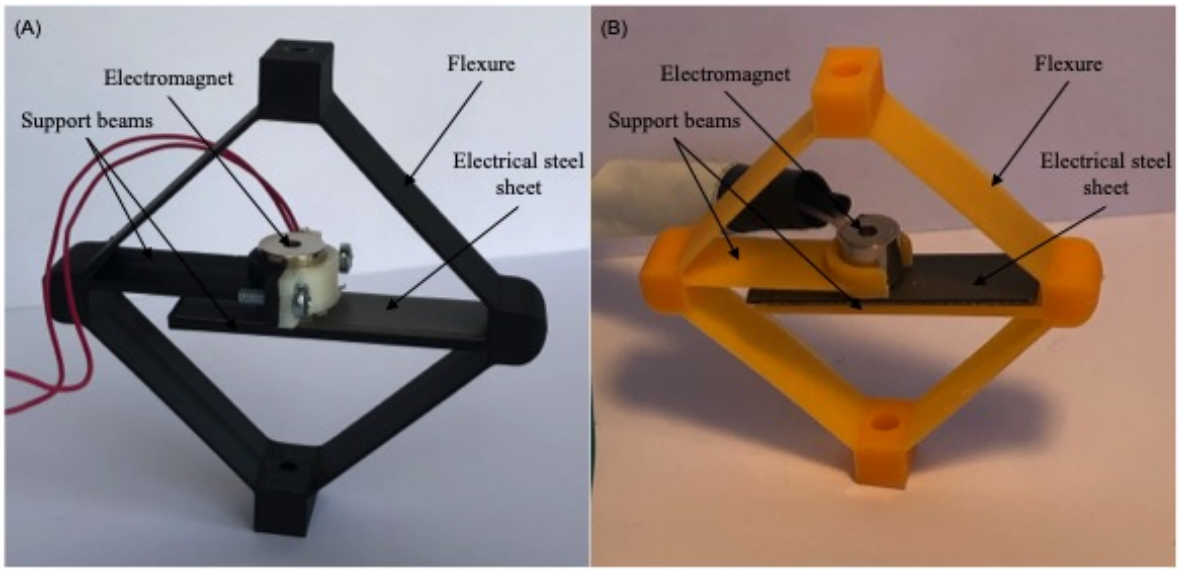

Fig. 7: Realisation of the active damping unit cell of figure 2. (A) 90mm unit cell, (B) 45mm unit cell

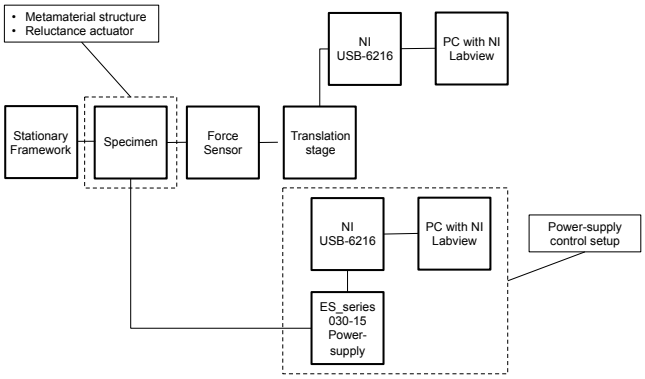

Fig. 8: Block diagram of experimental set-up for quasi-static loading measurements

a MATLAB script for further evaluation in the following section on the results of our project.

IV. Results

A. Passive lattice structure

In order to measure the stored strain energy in the flexures of the lattice structure, external loading is applied in uni-axial direction. The following experiment is conducted by using the quasi-static deformation measurement set-up III-B.1 as can be described in section III-B with the passive structure as a specimen. The strain rate is kept at 20mm/min and the resulting force-deformation curves for both unit cells – see figure 7 - are plotted in figure 13.

The experimentally tested range of the 90mm unit cell is ±10mm and for the 45mm unit cell ±5mm and is indicated with dots. Also visible in figure 13 are the theoretically estimated force-displacement curve that is specified with the dashed line, and the behaviour that is modelled in a finite element analysis and is indicated with a solid line. An effective modulus E_{eff} is substituted in both – the

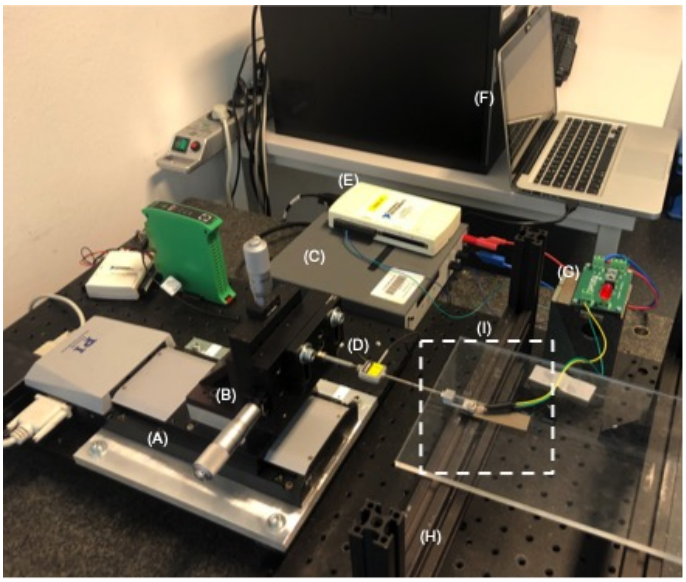

Fig. 9: Experimental setup for quasi-static deformations. (A) Translation stage, (B) Second translation stage, (C) Power-supply, (D) Force sensor, (E) USB-6215, (F) Laptop, (G) Transistor, (H) Aluminium framework, (I) Specimen positioning

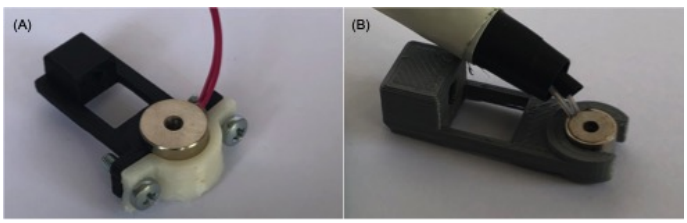

Fig. 10: Harness for measuring friction force created by the reluctance actuator. (A) Harness used for 10N electromagnet, (B) Harness with clamp used for 1N electromagnet

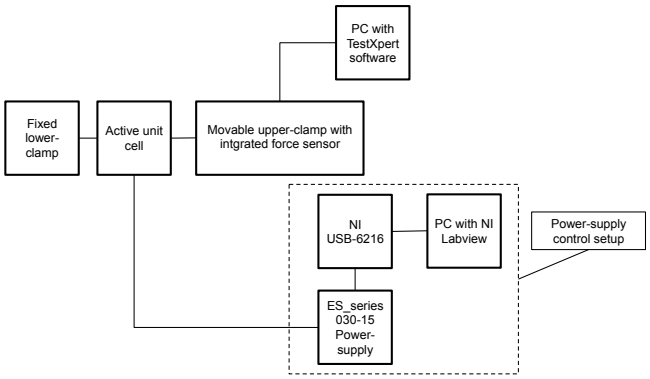

Fig. 11: Block diagram of experimental set-up for testing cyclic loading measurements

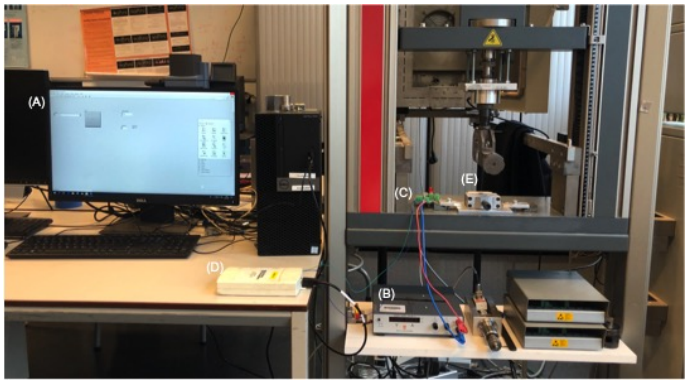

Fig. 12: Experimental setup for cyclic loading measurements. (A) Force sensor, (B) Power supply, (C) Control interface, (D) Clamping stage

theoretical and the finite element analysis – in order to simulate the passive lattice structure. The magnitude of the effective stiffness E_{eff} is 5.6 GPa for the 90mm unit cell and 1.9 GPa for the smaller 45mm cell. The measured stored energy during loading of the lattice structure is the surface area under the stiffness line of figure 13. Therefore, the experimentally tested elastic strain energy is 3.5e-2J for the 90mm lattice and 3.1e-3J for the small lattice.

B. Reluctance actuator

The following results are established using the quasi-static deformation measurement set-up presented in figure III-B.1 and described in section III-B at a strain rate of 20mm/min. This time the specimens are the 10N and 1N reluctance force actuators, which are presented in figure 5. The amount of dissipated friction energy is measured during a back and forth sliding movement of 5mm for the 10N reluctance force actuator and 2.5mm for the 1N actuator. The first experiment consists of sliding over an electrical steel sheet and in the second setting, the electrical steel sheet is covered with a thin film of Teflon (PTFE). The electromagnets are clamped in the harness as is illustrated in figure 10 and they are attached to the force sensor as can be seen in figure 9. The resulting force-displacement curves are indicated in figure 14. A number of measurements for damping have been

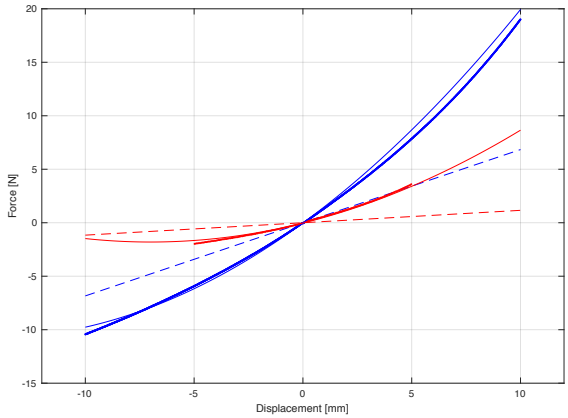

Fig. 13: Force over displacement. Blue line indicates the 90mm unit cell behaviour during experimental testing, red line indicates the 45mm unit cell behaviour during experimental testing, dashed line indicates the behaviour during finite element simulation

undertaken at 4 V increments. The friction force is obtained from the force average and illustrated in a force-voltage graph with interval steps of 4V. The friction force is derived from the force average of both reluctance actuators - see figure 15- and results show maximum friction force of 0.59N for the 10N and 0.27N for the 1N electromagnet.

C. Active unit cells

A third category of experiments uses the experimental setup III-B.2 that was described in section III-B at strain rate of 80mm/min. The experiments are conducted for single cyclic motion and with voltage inputs at 4V increments. Figure 16 illustrates the force-displacement behaviour of the large assembled active unit cell. This cell consists of the 10N reluctance actuator as the stator and an electrical steel sheet without Teflon as the mover. The experiment illustrated in figure 17 is conducted with the 45mm unit cell, and consists of the 1N reluctance actuator. The surface area equals the dissipated friction energy during motion of the actuator. The incremental increase in dissipated energy is shown for an incremental voltage increase. The dissipated energy range for a 10N magnet is 1.0e-3 - 1.2e-2J for a 0V-24V input and the smaller 1N electromagnet is limited due to ohmic heating and has a dissipation of 6.1e-4 - 4.1e-3J at 0-16V input.

The ratio of damped energy over the stored energy during loading is shown in section II-C. Figure 18 illustrates the damping ratio of the 90mm and 45mm cell for incremental values of 4V. This implies increasing dissipated friction energy. The friction energy is the surface area of figure 16 and 17. The stored energy during loading is given in the surface area under the stiffness lines in figure 13. The equation for this ratio is given in section II-C.4. The damping ratio for the active unit cell is given for a 5mm deformation at 0-24V. The damping ratio for the scaled

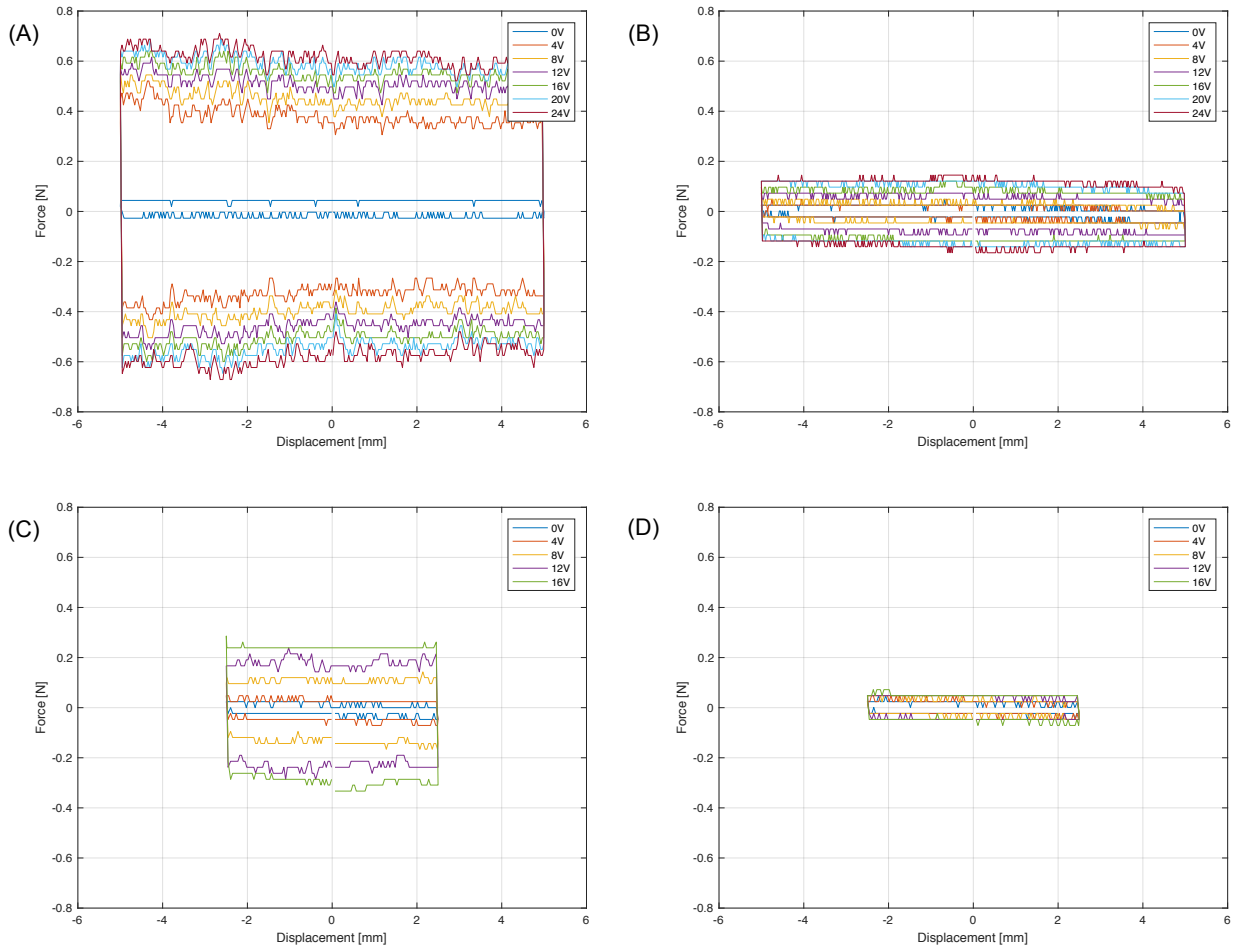

Fig. 14: Friction force per displacement. (A) 10N reluctance force actuator over electrical iron sheet , (B) 10N reluctance force actuator over electrical iron sheet with Teflon layer, (C) 1N reluctance force actuator over electrical iron sheet , (D) 1N reluctance force actuator over electrical iron sheet with Teflon layer

active unit cell is given for 2.5mm deformation at 0-16V.

Viscoelastic damping effects could occur during increasing velocities. Therefore, the active unit cell is subjected to an increasing rate of deformation ranging from 60-140mm/min at 24V and displayed in graph 19. The amount of dissipated energy, which is indicated by the surface area of the loop, remains predominantly equal. Therefore the unit cell does not exhibit any motion resistance due to viscous effects in the lattice structure as these are negligible.

V. Discussion

A. Passive lattice structure

Small errors in 3D-printing result in extensive performance deviations. Tolerances, imperfect structure and infill, caused by 3D printing, can induce significant differences of stored energy in the metamaterial structure in practice. A bulk modulus, therefore, cannot be applied, and thus an effective modulus E_{eff} has been established with a finite element simulation. This modulus has been substituted in both - theoretical and finite element analysis - given in figure 13 to simulate the force-displacement behaviour of the passive structure. Shortcomings of the used equation 5 [14] have resulted in a discrepancy of force-displacement behaviour with respect to the behaviour experimentally tested, see again figure 13. Therefore, the analytical model is insufficient to model the experimental behaviour.

Next, stretching and compression generate a marked difference in force magnitude, as is evident between the first and third quadrant of figure 13. A greater force has to be applied to stretch the lattice for the same deformation length in contrast to compressing the lattice. This phenomenon is a consequence of the configuration of the lattice, which can be seen in figure 2.

Lastly, the finite element analysis confirms that plastic deformation does not occur. The displacements of δ_{yy}=5mm for the 90mm unit cell result in stresses of 42MPa and 37MPa for stretching and compression, both of which are below the yield for PLA. The scaled lattice structure displays the same topology, while the parameters were scaled with a factor 1:2. The material used is a resin

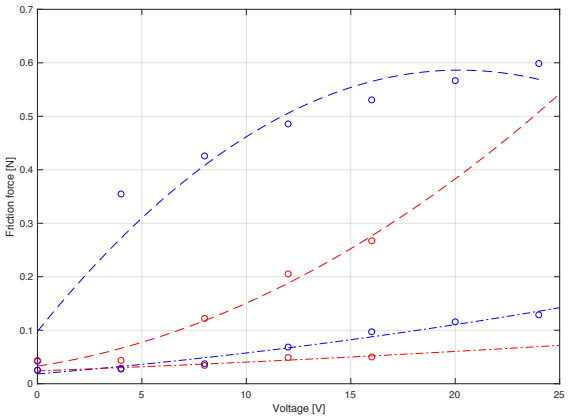

Fig. 15: Friction force per voltage. The blue dotted line indicates friction force for 10N reluctance force actuator over the electrical iron sheet with Teflon layer, the blue dashed-dotted line indicates friction force for 10N reluctance force actuator over the electrical iron sheet, the red dotted line indicates friction force for 1N reluctance force actuator over the electrical iron sheet with Teflon layer, the red dashed-dotted line indicates friction force for 1N reluctance force actuator over electrical iron sheet

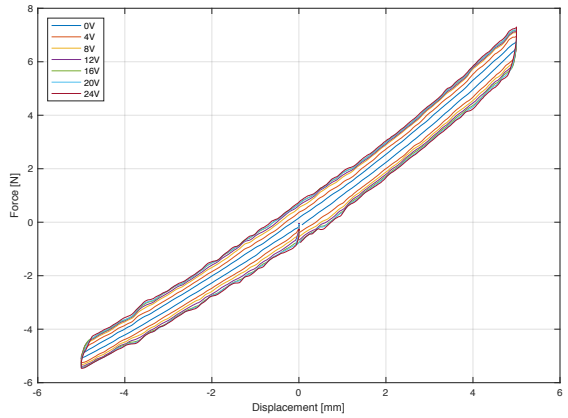

Fig. 16: Force per displacement behaviour of the active 90mm active unit cell for increments of 4V

material instead of PLA. The finite element analysis showed that strains of δ_{yy}=2.5mm result in stresses of 13MPa and 12MPa for stretching and compression, both of which are below the yield for a resin of 34 MPa.

B. Reluctance actuator

While Teflon tape helped to tune the friction force, it is a contribution of both the increased air-gap (i.e. due to tape thickness) and friction coefficient (Teflon-iron VS iron-iron). The maximum normal force is being achieved in the absence of an air-gap between the mover and stator, and depends on the reluctance actuator. An increase of the friction force requires very thin and coarse contact–surfaces; decreasing the voltage range and increasing the resolution for the friction force can be attained by surface coating and modifying the thickness of the Teflon tape.

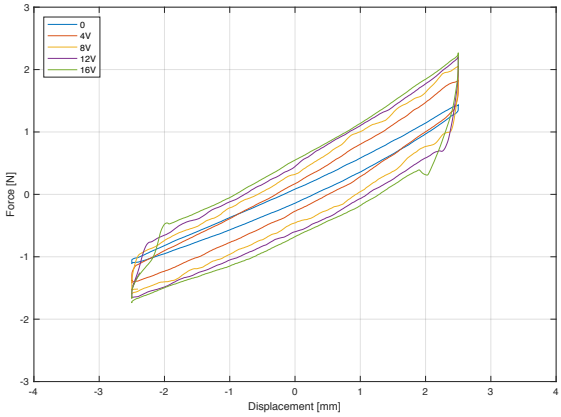

Fig. 17: Force per displacement behaviour of the active 45mm active unit cell for increments of 4V

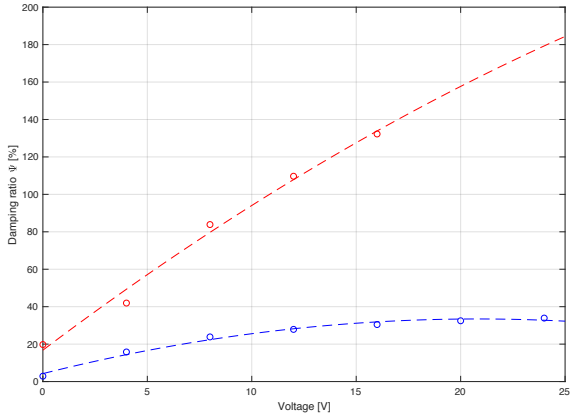

Fig. 18: Damping ratio per voltage. The 90mm assembled unit cell for increments of 4V is presented with the blue dotted line and the 45mm assembled unit cell for increments of 4V is presented with the red dotted line

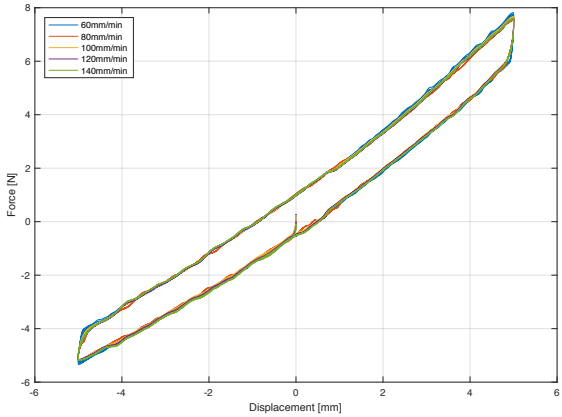

Fig. 19: Force-displacement behaviour of 90mm unit cell with increasing deformation velocity at 24V input voltage

The reluctance and friction forces as given respectively in equations 6 and 7 should have scaled quadratically with increasing current. This, however, did not happen according to the curves of figure 15. Firstly, we hypothesize that the cause is due to resistive heating in the electromagnetic actuator. Resistive heating decreases the input current and, therefore, the magnetomotive force $\mathcal{F} = ni$. Small electromagnetic actuator volume involves excessive heat dissipation, and therefore, in future research minimization of Joule heating in the actuator may be attained through optimising the choice of contact materials. Secondly, the influence of magnetic core saturation that affect the actuator performance outcome. The larger the current that passes through the wire coil, the more the magnetic domains align and the stronger the resulting magnetic field; ultimately all domains align and saturation follows. The magnitude of the reluctance force and thus friction force is further limited by the size of the actuator, since its small core becomes magnetically saturated. Therefore, detailed friction force coefficients cannot be indicated properly.

C. Active unit cell

The ratio between the dissipated Coulomb damping and the stored energy is given with equation 9. This ratio is given in figure 18 for both the 90mm unit cell and 45mm unit cell. Results show that the downscaled 45mm cell attains a higher damping ratio than the larger 90mm unit cell.

The explanation lies with three factors. Firstly, the material of the scaled lattice is made of less stiff material, which causes softening of flexures. Therefore, less energy can be stored in the flexures. Secondly, bending energy does not scale linearly because of the flexure thickness. The strain equation 5 equals the stored energy in the unit cell and the last part of the equation is the strain energy in the bending moment of the flexure. Therefore the stored energy decreases more rapidly with smaller values of t. Lastly, in figure 17 one observes how applied forces with voltage inputs of 12V and 16V induce exceptional behaviour in the force-displacement curve of the 45mm unit cell. Stick-slip occurs which is visible at the maximum displacement of ±2.5mm. This phenomenon is a result of the change of deformation direction, which induces static friction boundaries that exceed flexural stiffness.

VI. Conclusion

This paper has introduced the first-ever metamaterial cell design for controlled damping. Its behaviour has been modelled, a proof-of-principle demonstrator has been built, and the cell has been tested experimentally with regard to its behaviour under mechanical loading. Elastic and damping behaviour has been modelled separately, while the demonstrator has been examined under cyclic loading. The theoretical analysis predicts a positive result with respect to the damping ratio for the behaviour of active unit cells. Thereafter, in practice, the unit cell was produced by 3D-printing, for which commercially available reluctance actuators were utilised in order to create electrically controlled damping.

Test-results did indicate a tunable damping coefficient in the unit cell for cyclic deformation. It has been shown that for a unit cell, of 90mm with a 10N reluctance force magnet, the maximum tunable damping is 1.2e-2J for a single cycle with a deformation range of 5mm. The stored energy during this motion is 3.5e-2J. Altogether, this will lead to a maximum damping ratio up to 34%. The 45mm unit cell with the 1N reluctance force magnet can achieve 4.1e-3J damping for a cyclic deformation of 2.5mm. Since the flexures are less stiff, the implication is that stored energy amounts to 3.1e-3J and damping range up to 132%.

Tolerances, imperfections and fill during 3D-printing of the passive structure restrained modelling of this force-displacement behaviour. A material bulk modulus cannot be used, therefore an effective stiffness modulus E is required. For both, the 90mm unit cell and the 45mm unit cell, a finite element analysis was conducted. Estimating an effective modulus E_{eff} of 5.6GPa for the 90mm unit cell and 1.9GPa for the 45mm unit cell. Simplifications due to analytical formulas have generated a discrepancy between theoretical and experimental results. However, the FEM results in the behaviour of the passive structure were similar to the experimentally validated force-displacement of the passive structure.

More detailed knowledge regarding friction force and decreasing the range of voltage and increasing friction force resolution can be achieved by optimization of thickness and coarse contact surfaces. Furthermore, the friction force should scale quadratically with input current, however, this is not visible in the results. It is due to resistive heating or saturation of the electromagnetic stator. As a result, detailed electromagnetic performance simulations are falling short in this thesis. Because simulations require knowledge about magnetomotive-force and actuator configuration and off-the-shelve components, regrettably do not generate this kind of information. Further research, therefore, is necessary for the analysis of performance.

Lastly, the resulting damping ratio of the 90mm unit cell is lower than for the 45mm unit cell. This is related to the miniaturisation effects of the unit cell. The damping ratio Φ can be altered with the degree of softness of flexures, actuator performance and dimension parameters. Further research on the combined scaling effects of a passive structure and actuator could yield deeper insight into the scaling of this damping ratio.

In conclusion, this study has extended the novel scientific field of metamaterials with the introduction of an active unit cell along with controlled damping. This shapes the

foundation for exciting topics regarding controlled vibration isolation in mechanical metamaterial unit cell structures.

REFERENCES

[1] A. A. Zadpoor, "Mechanical meta-materials," *Mater. Horiz.*, vol. 3, pp. 371–381, 2016.

[2] J. Surjadi, L. Gao, H. Du, X. Li, X. Xiong, and N. Fang, "Mechanical metamaterials and their engineering applications," *Advanced Engineering Materials*, 01 2019.

[3] K. Evans and A. Alderson, "Auxetic materials: Functional materials and structures from lateral thinking!," *Advanced Materials - ADVAN MATER*, vol. 12, pp. 617–628, 05 2000.

[4] M. Kadic, T. Bückmann, N. Stenger, M. Thiel, and M. Wegener, "On the practicability of pentamode mechanical metamaterials," *Applied Physics Letters*, vol. 100, no. 19, p. 191901, 2012.

[5] J. Christensen, M. Kadic, O. Kraft, and M. Wegener, "Vibrant times for mechanical metamaterials," *MRS Communications*, vol. 5, no. 3, p. 453–462, 2015.

[6] Z. Nicolaou and A. Motter, "Mechanical metamaterials with negative compressibility transitions," *Nature materials*, vol. 11, pp. 608–13, 05 2012.

[7] X. Yu, J. Zhou, H. Liang, and L. Wu, "Mechanical metamaterials associated with stiffness, rigidity and compressibility: A brief review," *Progress in Materials Science*, vol. 94, 12 2017.

[8] T. Mizuno, T. Toumiya, and M. Takasaki, "Vibration isolation system using negative stiffness," *JSME International Journal Series C*, vol. 46, pp. 807–812, 09 2003.

[9] M. Haberman, C. Seepersad, and P. Wilson, "Vibration damping and isolation using negative stiffness structures," *The Journal of the Acoustical Society of America*, vol. 138, pp. 1920–1920, 09 2015.

[10] R. Kornbluh, H. Prahlad, R. Pelrine, S. Stanford, M. Rosenthal, and P. Guggenberg, "Rubber to rigid, clamped to undamped: Toward composite materials with wide-range controllable stiffness and damping," *Proceedings of SPIE - The International Society for Optical Engineering*, vol. 5388, 07 2004.

[11] R. Poon and J. B. Hopkins, "Phase-changing metamaterial capable of variable stiffness and shape morphing," *Advanced Engineering Materials*, vol. 21, p. 1900802, 2019.

[12] J. Overvelde, T. de Jong, Y. Shevchenko, S. Becerra, G. Whitesides, J. Weaver, C. Hoberman, and K. Bertoldi, "A three-dimensional actuated origami-inspired transformable metamaterial with multiple degrees of freedom," *Nature Communications*, vol. 7, 03 2016.

[13] S. Li and K.-W. Wang, "Fluidic origami: A plant-inspired adaptive structure with shape morphing and stiffness tuning," *Smart Materials and Structures*, vol. 24, 10 2015.

[14] B. Haghpanah, H. Ebrahimi, D. Mousanezhad, J. Hopkins, and A. Vaziri, "Programmable elastic metamaterials," *Advanced Engineering Materials*, vol. 18, pp. n/a–n/a, 10 2015.

[15] R. Hamelinck, "Adaptive deformable mirror : based on electromagnetic actuators," 2010.

[16] D. Shin, K. Seong, E. s. Jung, J.-H. Cho, and K.-Y. Lee, "Design of a dual-coil type electromagnetic actuator for implantable bone conduction hearing devices," *Technology and Health Care*, vol. 27, pp. 1–10, 04 2019.

[17] B. Håkansson, "The balanced electromagnetic separation transducer: A new bone conduction transducer," *The Journal of the Acoustical Society of America*, vol. 113, pp. 818–25, 03 2003.

[18] A. Katalenic, "Control of reluctance actuators for high-precision positioning," no. april, p. 150, 2013.

[19] P. L. Chapman and P. T. Krein, "Micromotor technology: Electric drive designer's perspective," *Conference Record - IAS Annual Meeting (IEEE Industry Applications Society)*, vol. 3, no. May, 2001.

[20] H. Trimmer, "Microrobots and micromechanical systems," 1989.

[21] L. Molenaar, *A novel planar magnetic bearing and motor configuration applied in a positioning stage*. PhD thesis, Delft University of Technology, 10 2000.

[22] R. M. Schmidt, G. Schitter, and J. van Eijk, *The design of high performance mechatronics*. 2011.

[23] F. Orban, "Damping of materials and members in structural mechanics," 1968.

5

Conclusions

This project has focused on active metamaterials with utilisation of centimeter-scale electromagnetic actuators. Research on active metamaterials is hardly found in the current literature; the complex design structures and difficult actuation principles may explain this phenomenon. Adaptive composites show promising features as active components, but are currently not suitable for implementation in mechanical metamaterials. While smart materials make steady progress, already at present, activation of mechanical can be achieved by exploiting electromagnetic actuators. The challenge when exploiting electromagnetic actuators in metamaterials is posed by the complex process of miniaturisation. Therefore, a thorough investigation of efforts towards making miniature electromagnetic actuators is conducted. The synthesizing finding is that downscaling is investigated in a small number of studies and that electromagnetic actuators are hardly available as actuators in the subcentimeter-scale region. In this project I have developed an analytical approach to scaling effects of electromagnetic actuators in order to gain insight into electromagnetic actuators and their properties when scaled in this volume range. Furthermore, I have chosen to develop a proof-of-principle metamaterial cell for active damping by utilising reluctance actuator as tunable Coulomb dampers that can be electrically regulated to change the magnitude of dissipated energy. A preliminary cell design was used and commercially available actuators have been integrated. Additive manufacturing of the structure is chosen for practical efficiency. Thereafter the assembled demonstrator has been analysed and validated with respect to performance behaviour, tunability and miniaturisation. The most important conclusions of this work now are summarized.

- **Scaling effects** It became clear that the analysis - see chapter 3 - regarding miniaturisation effects in Lorentz and reluctance force actuators with fixed configurations can give deeper insight into the feasibility and the performance of two distinct design configurations during scaling. Namely, the force per volume behaviour can estimate when actuator volume is modified with a single parameter from cubic centimeter to millimeter range.
- **Active unit cell design** This study proposes an active metamaterial unit cell design with utilisation of centimeter-scale electromagnetic actuators. This is a novel concept because a unit cell design has been developed that possesses the required metamaterial stiffness profile as well as tunable damping capabilities. It was found that the unit cell effectively behaves to allow for the reluctance actuator to create coulomb damping.
- **Metamaterial lattice structure** It was found that the unit cell possesses the ability to store energy in the lattice structure. The strain energy is stored in the flexures during deformation due to its elasticity. Experimental validation with cyclic loading in uni-axial direction resulted in elastic strain energies. The 90mm unit cell can store 3.5e-2J for loading deformations of 5mm. Whereas the 45mm unit cell can achieve 3.1e-3J for 2.5mm deformations.
- **Integration and utilisation of reluctance force actuators as coulomb dampers** The research confirmed that reluctance force actuators, if electrically controlled, could alter the dissipated energy in the unit cell. Firstly, friction forces were measured during a back and forth sliding movement of the 10N

and 1N reluctance force actuator and showed maximum friction forces of 0.59N and 0.27N respectively. Test-results indicate that for a unit cell, 90mm with a 10N reluctance force actuator, the dissipated energy ranges from 1e-3J to 1.2e-2J for a single cycle with a deformation similar to that of the passive structure. The 45mm unit cell with a 1N reluctance force actuator can achieve damping from 6.1e-4J to 4.1e-3J for cyclic deformations of 2.5mm.

- **Tunable damping ratio in the active unit cell** The presence of a tunable damping coefficient in the unit cell has been experimentally verified. This ratio is the combined behaviour of the dissipated Coulomb damping and the stored energy. The electrically controlled reluctance actuator can be used to change the dissipated energy in the unit cell, resulting in a tunable damping ratio. The 90mm and 45mm unit cell can achieve ratios ranging from 3% and 20% up to 34% and 132% respectively.

6

Recommendations

Our project provides a number of leads for further research in the field of activating metamaterials with utilisation of electromagnetic actuators. Key themes of our project each offer a further perspective.

- **Scaling effects** The analysis presented in chapter 3 has constrained the configurations of actuator design with a single scaling parameter. However, if this would be extended with additional scaling parameters in actuator configuration, specific optimization solutions for actuator designing may be found. Trade-off between the magnetomotive-force, wiring space and the length of the flux path, which are all dimension constraints, could improve optimization of actuator performances.
- **Active unit cell design** The design has been modelled with a FEM analysis and has produced the predicted results in the experiments for the metamaterial structure. Further research in FEM analysis could give insight in the stored energy in the unit cell related to design parameters.
- **Realisation** Additive manufacturing of the passive structure has been a suitable option for printing metamaterials. However tolerances, imperfections and fill during 3D-printing restrained modelling of the force-displacement behaviour of the metamaterial structure.
- **Modelling** Bulk stiffness is not included in a unit cell structure when modelled. Therefore, an effective modulus E_{eff} has to be estimated in a finite element analysis. Simplifications in analytical modelling of complex structures have resulted in discrepancy between the analytical and finite element model. Therefore further research in finite element analysis is advised.
- **Utilisation of the reluctance force actuator** Friction force testing has been conducted and imply that the maximum friction force is achieved for the highest voltage input and if the air-gap is close to zero. While Teflon tape helped to tune the friction force, it must be realised that it has an impact on both, the air-gap and friction coefficient. Therefore, friction force cannot be indicated properly. More detailed information regarding friction force, as well as, decrease of the friction force resolution, can be achieved by optimization of thickness/coarse contact surfaces.
- **Reluctance actuator performance** The friction force, induced by a reluctance force, should scale quadratically with input current. However, the results do not underscore this outcome. Our hypothesis points at either resistive heating or saturation of the electromagnetic stator as possible causes for this discrepancy. Detailed electromagnetic performance simulations have not been possible due to limited knowledge of actuator specifications for off-the-shelve components, which leads to less detailed simulations of the electromagnetic actuator.
- **Damping coefficient** Damping coefficient Φ scales non-linear when the active unit cell is miniaturised. Further research is necessary to address this problem which results from scaling the metamaterial structure and the actuator simultaneously.

A

Matlab code - Chapter 3

```
% Force per volume of Lorentz and reluctance force actuator with
 shifting point of intersection (figure 6,7,8)

close all
clear all
clc

%Parameters
H_c = 1000*10^3; %Coercivity [A/m]
mu_0 = 4*(pi)*10^-7; %Vacuum permeability [H/m]
d_w = 0.1*10^-3; %Wire diameter [m]
J_dens = 1*10^7; %Current density [A/m^2]
I_lim = 0.079; %Current [A]
V1=[10^-8 10^-7 10^-6 10^-5 10^-4 10^-3 10^-2 10^-1 10^0]; %
 Reluctance actuator volume [m^3]


% Calculation of the Lorentz force
f1 = @(V1) ((V1)/27.9).^(1/3); %alpha
y1=f1(V1);
Fl =(mu_0*H_c*((y1.^3))*I_lim)/(d_w^2); %Lorentz force [N]


% Calculation of the Reluctance force
for i=1:length(V1)
    C = 0.1; %Actuation constant C (Values: 0.05,0.1,0.15)
    f2(i)=((V1(i))/(24+(8*C)))^(1/3); %Scaling parameter beta
    l_g(i) = C*f2(i); % Stroke length l_s
    Fr(i)= (mu_0*(I_lim^2)*(f2(i).^6))./
(4*(d_w^4)*(l_g(i).^2)); %Reluctance force [N]
end


figure
loglog(V1,Fl,V1,Fr)
grid on
legend({'Lorentz force','Reluctance force'})
xlabel('Volume [m^{3}]')
ylabel('Force [N]')

% Force per volume of reluctance force actuator - saturation limit
 (figure 9)

close all
clear all
clc

H_c = 1000*10^3; %Coercivity [A/m]
mu_0 = 4*(pi)*10^-7; %Vacuum permeability [H/m]
d_w = 0.1*10^-3; %Wire diameter [m]
J_dens = 1*10^7; %Current density [A/m^2]
I_lim = 0.079; %Current [A]
```

```
B_lim = 2;
V1=[10^-8 10^-7 10^-6 10^-5 10^-4 10^-3 10^-2 10^-1 10^0]; %
 Reluctance actuator volume [m^3]


%Calculation of the reluctance force
for i=1:length(V1)
    C = 0.1; %Actuation constant C
    f2(i)=((V1(i))/(24+(8*C)))^(1/3); %Scaling parameter beta
    l_g(i) = C*f2(i); %ls
    Fr(i)= (mu_0*(I_lim^2)*(f2(i).^6))./(4*(d_w^4)*(l_g(i).^2));
end

%Reluctance force with saturation line, which implies the force
 limited by saturation
for i=1:length(V1)
    C = 0.1; %Actuation constant C (Values: 0.05,0.1,0.15)
    f2(i)=((V1(i))/(24+(8*C)))^(1/3); %Scaling parameter beta
    l_glim(i) = (mu_0*(f2(i)^2)*I_lim)/(2*B_lim*(d_w^2)); %gap limit
 by saturation
    Flim(i)= (mu_0*(I_lim^2)*(f2(i).^6))./
(4*(d_w^4)*(l_glim(i).^2)); % force limit by saturation
end


figure
loglog(V1,Fr,V1,Flim,'--')
grid on
legend({'Reluctance force','Saturation limit'})
xlabel('Volume [m^{3}]')
ylabel('Force [N]')


% Force per displacement for a Lorentz and reluctance force actuator -
 Calculation of mechanical work per stroke displacement (figure 10)

close all
clear all
clc

%variables
H_c = 1000*10^3; %[A/m] Coercivity
mu_0 = 4*(pi)*10^-7; %[H/m] Vacuum permeability
d_w = 0.1*10^-3; %[m] Wire diameter
J_dens = 1*10^7; % [A/m^2] Current density
I_low = J_dens*(pi*((0.5*d_w)^2)); % Assumed lower  boundary limit
I_lim = 0.179; % Assumed upper boundary limit
V1=[10^-6]; %Volume (Values: 10^-9, 10^-6, 10^-3) [m^3]


for i=1:length(V1)
    C = 0.1; %Actuation constant C (Values: 0.05,0.1,0.15)
    f2(i)=((V1(i))/(24+(8*C)))^(1/3); %Scaling parameter beta
    l_s(i) = C*f2(i); % stroke length
```

```
end

% Reluctance force during displacement gaplength l_s
l_gh1 = 0;
l_gh2 = l_s;
dx = l_gh2/1000;
dx2 = (l_gh2-(f2/20))/1000;
x2=[l_gh1:dx:l_gh2];
x3=[(f2/20):dx2:l_gh2]; % stroke displacement
F_rel = (mu_0*(I_lim^2)*(f2^6))./(4*(d_w.^4)*(x2.^2));
F_rel2 = (mu_0*(I_lim^2)*(f2^6))./(4*(d_w.^4)*(x3.^2));

% Calculation Lorentz force
f1 = @(V1) ((V1)/27.9).^(1/3);
y1=f1(V1); %alpha
Fl =(mu_0*H_c*((y1.^3))*I_lim)/(d_w^2);
Fl_calc = Fl*ones(size(x3));


figure

semilogy(x3,Fl_calc,'r');
hold on
semilogy(x3,F_rel2,'b');
hold on
semilogy(x2,Fl*ones(size(x2)),'--r');
hold on
semilogy(x2,F_rel,'--b');
grid on
legend({'Lorentz force','Reluctance force'})
xlabel('Displacement [m]')
ylabel('Force [N]')


% Calculation of mechanical work; Surface area under force-
displacement curve
area_1 = trapz(x3,F_rel2);
area_2 = trapz(x3,Fl_calc);

% Heat dissipation in Lorentz force and reluctance force actuators
 (figure 11)

close all
clear all
clc


%Parameters
H_c = 1000*10^3; %Coercivity [A/m]
mu_0 = 4*(pi)*10^-7; %Vacuum permeability [H/m]
d_w = 0.1*10^-3; %Wire diameter [m]
J_dens = 1*10^7; %Current density [A/m^2]
I_lim = J_dens*(pi*((0.5*d_w)^2)); %Current limitation
Res_cu = 1.68*10^-8; %Resisivity copper [ohm*m]
```

```
B_g = 2; %Saturation limit B_sat

F=0.1135; %Force limit regarding saturation limitations
V1=[10^-4 10^-3 10^-2 10^-1 10^0];%Volume range
f1 = @(V1) ((V1)/27.9).^(1/3); %alpha, gap of 0.1*alpha
f2 = @(V1) ((V1)/24.8).^(1/3); %beta gap of 0.1*beta
y1=f1(V1); %alpha
y2=f2(V1); %beta

l_g = 0.1*y2; %Gaplength l_s
beta_lim = (2*B_g*l_g*(d_w^2))/(mu_0*I_lim); %limit van beta op
 respectivelijk [10^-4 10^-3 10^-2 10^-1 10^0]


% Calculating the dissipated heat per volume
p1 = ((Res_cu)*16*(y1.^3)*(I_lim^2))/(pi*(d_w^4));
p2 = ((Res_cu)*16*(y2.^3)*(I_lim^2))/(pi*(d_w^4));


semilogx(V1,p1./V1,V1,p2./V1)
grid on
legend({'Lorentz force actuator','Reluctance force actuator'})
xlabel('Volume [m^{3}]')
ylabel('Heat dissipation per volume [W/m^{3}]')
```

Published with MATLAB® R2017b

B

Matlab code - Chapter 4

```
% Cell analysis - modeling elastic strain energy

close all
clear all
clc

syms x L
system_dependent('setround', 0)

% Parameters
L = 20; %[mm] Length of vertical/horizontal beam
L_1 = sqrt(2*L^2); %[mm] Length of diagonal beam
L_2 = 5; %[mm] Lenght block
t_1 = 0.5; %[mm] Thickness beam
t_2 = 5; %[mm] Width block
B = 8; %[mm] Depth unit cell
E = 1900; % [MPA = N/mm^2]Emodulus
theta = 45; % [degrees] Angle with vertical axis
delta_y = 10;  %[mm] Total deformation in y-direction
l_g1 = 0; % Lower boundary integral
l_g2 = L_1; % Upper boundary integral

A_1 = B*t_1; %[N/mm^2] Cross-section beam
A_2 = B*t_2; %[N/mm^2] Cross-section Block
I_1 = (B*(t_1^3))/12; % [mm^4] Area moment of inertia
L_y = 2*(L_1*cos(theta)+L_2); %[mm]Total length in y direction

% Strain energy
a = 2/(E*(t_2/L_2));
b = (cos(theta)^2)/(E*(t_1/L_1));
c = (sin(theta)^2)/(E*((t_1/L_1)^3));
F = (B*delta_y)/(a+b+c); %[N] Force

M = -(1/4)*F*L_1*sin(theta); %[nmm] Internal moment
d = (L_2*F^2)/(E*A_2); %[nmm] Axial strain energy
e = (L_1*(F^2)*cos(theta)^2)/(2*E*A_1); %[nmm] axial strain energy
fun = @(x) (2*(M+(F/2)*x*sin(theta)).^2)/(E*I_1); % Bending strain
 energy equation
U_m = integral(fun,l_g1,l_g2); % Bending strain energy
U_t = d+e+U_m;  %Total strain energy (compressive or stretching
 strain)

% Strain energy 90-mm and 45-mm passive structure (figure 13)

close all
clear all
clc

% Read Excel experimentl results 90-mm passice structure:
U = readtable('Test1cm.xlsx');
x_1 = table2array(U(:,2))*(-0.001); % Displacement
y_1 = table2array(U(:,4))+0.09; % Force
```

```
V = readtable('Test-1cm.xlsx');
x_2 = table2array(V(:,2))*(-0.001); % Displacement
y_2 = table2array(V(:,4))-0.08; % Force


figure

% Experimental 90-mm:
plot(x_1,y_1,'.b');
hold on
plot(x_2,y_2,'.b');
hold on

% Read Excel experimentl results 45-mm passice structure:
Y = readtable('6_5mm.xlsx');
x_3 = table2array(Y(:,2))*(-0.001); % Displacement
y_3 = table2array(Y(:,4)); % Force

Z = readtable('6_m5mm.xlsx');
x_4 = table2array(Z(:,2))*(-0.001); % Displacement
y_4 = table2array(Z(:,4)); % Force


% Theoretical results 90-mm unit cell:
xzz = [-10 -5 -2.5 0 2.5 5 10];
x_e = xzz.';
yzz = [-6.840 -3.418 -1.709 0 1.709 3.418 6.840];
y_e = yzz.';

plot(x_e,y_e,'--b');
hold on

% Theoretical results 45-mm unit cell:
xyy = [-10 -5 -2.5 0 2.5 5 10];
x_f = xyy.';
yyy = [-1.160 -0.579 -0.290 0 0.290 0.579 1.160];
y_f = yyy.';

plot(x_f,y_f,'--r');
hold on

% Experimental 45-mm:
plot(x_3,y_3,'.r');
hold on
plot(x_4,y_4,'.r');
hold on


% COMSOL results 90-mm unit cell:
x0_e = [-8.19 -5.06 -2.37 -1.55 -0.76 5 8.92 9.28 9.62 9.95 10.24];
x_de = x0_e.';
y0_e = [-9.1 -6 -3 -2 -1 8 17 18 19 20 21];
y_de = y0_e.';
```

```
fd = fit(x_de,y_de,'poly2');
plot(fd,'b') %x_de,y_de);
hold on

% COMSOL results 45-mm unit cell:
x0_c = [-4.14 -3.25 -2.55 -1.88 -1.38 -0.89 -0.44 0.42 0.81 1.18 1.88
 2.2 2.51 3.34 4.49 4.88];
x_dc = x0_c.';
y0_c = [-1.6 -1.3 -1.05 -0.8 -0.6 -0.4 -0.2 0.2 0.4 0.6 1 1.2 1.4 2 3
 3.4];
y_dc = y0_c.';

fc = fit(x_dc,y_dc,'poly2');
plot(fc,'r')%,x_dc,y_dc,'xk');

grid on
xlabel('Displacement [mm]')
ylabel('Force [N]')
xlim([-12,12]);



% Friction force per displacement (figure 14)

% 10N reluctance force actuator over electrical iron sheet (Figure
 14.A)
close all
clear all
clc

% Read Excel experimental results:
T = readtable('10N_0V.xlsx'); %0V
x = table2array(T(:,2))*0.001;
y = table2array(T(:,4))-0.03;

U = readtable('10N_4V.xlsx'); %4V
x_2 = table2array(U(:,2))*0.001;
y_2 = table2array(U(:,4))-0.03;

V = readtable('10N_8V.xlsx'); %8V
x_3 = table2array(V(:,2))*0.001;
y_3 = table2array(V(:,4))-0.03;

W = readtable('10N_12V.xlsx'); %12V
x_4 = table2array(W(:,2))*0.001;
y_4 = table2array(W(:,4))-0.03;

X = readtable('10N_16V.xlsx'); %16V
x_5 = table2array(X(:,2))*0.001;
y_5 = table2array(X(:,4))-0.03;

Y = readtable('10N_20V.xlsx'); %20V
x_6 = table2array(Y(:,2))*0.001;
```

```
y_6 = table2array(Y(:,4))-0.03;

Z = readtable('10N_24V.xlsx'); %24V
x_7 = table2array(Z(:,2))*0.001;
y_7 = table2array(Z(:,4))-0.03;


figure;
plot(x,y,x_2,y_2,x_3,y_3,x_4,y_4,x_5,y_5,x_6,y_6,x_7,y_7);
legend({'0V';'4V';'8V';'12V';'16V';'20V';'24V'})
grid on
xlabel('Displacement [mm]')
ylabel('Force [N]')
xlim([-6,6]);


% 10N reluctance force actuator over electrical iron sheet with
% Teflon layer (Figure 14.B)
close all
clear all
clc

% Read Excel experimental results:
T = readtable('TM0 copy.xlsx'); %0V
x = table2array(T(:,2))*0.001;
y = table2array(T(:,4));

U = readtable('TM4 copy.xlsx'); %4V
x_2 = table2array(U(:,2))*0.001;
y_2 = table2array(U(:,4));

V = readtable('TM8 copy.xlsx'); %8V
x_3 = table2array(V(:,2))*0.001;
y_3 = table2array(V(:,4));

W = readtable('TM12 copy.xlsx'); %12V
x_4 = table2array(W(:,2))*0.001;
y_4 = table2array(W(:,4));

X = readtable('TM16 copy.xlsx'); %16V
x_5 = table2array(X(:,2))*0.001;
y_5 = table2array(X(:,4));

Y = readtable('TM20 copy.xlsx'); %20V
x_6 = table2array(Y(:,2))*0.001;
y_6 = table2array(Y(:,4));

Z = readtable('TM24 copy.xlsx'); %24V
x_7 = table2array(Z(:,2))*0.001;
y_7 = table2array(Z(:,4));



figure;
```

```
plot(x,y,x_2,y_2,x_3,y_3,x_4,y_4,x_5,y_5,x_6,y_6,x_7,y_7);
legend({'0V';'4V';'8V';'12V';'16V';'20V';'24V'})
grid on
xlabel('Displacement [mm]')
ylabel('Force [N]')
xlim([-6,6]);
ylim([-0.8,0.8]);


% 1N reluctance force actuator over electrical iron sheet (Figure
 14.C)
close all
clear all
clc

% Read Excel experimental results:
T = readtable('0V_I.xlsx'); %0V
x = table2array(T(:,2))*0.001;
y = table2array(T(:,4))-0.05;

U = readtable('4V_I.xlsx'); %4V
x_2 = table2array(U(:,2))*0.001;
y_2 = table2array(U(:,4))-0.05;

V = readtable('8V_I.xlsx'); %8V
x_3 = table2array(V(:,2))*0.001;
y_3 = table2array(V(:,4))-0.05;

W = readtable('12V_I.xlsx'); %12V
x_4 = table2array(W(:,2))*0.001;
y_4 = table2array(W(:,4))-0.05;

X = readtable('16V_I_2.xlsx'); %16V
x_5 = table2array(X(:,2))*0.001;
y_5 = table2array(X(:,4))-0.05;



figure;
plot(x,y,x_2,y_2,x_3,y_3,x_4,y_4,x_5,y_5);
legend({'0V';'4V';'8V';'12V';'16V'})
grid on
xlabel('Displacement [mm]')
ylabel('Force [N]')
xlim([-6,6]);
ylim([-0.8,0.8]);


% 1N reluctance force actuator over electrical iron sheet with (Figure
 14.D)
% Teflon layer
close all
clear all
clc
```

```
% Read Excel experimental results:
T = readtable('0V_T.xlsx'); %0V
x = table2array(T(:,2))*0.001;
y = table2array(T(:,4))-0.026;

U = readtable('4V_T.xlsx'); %4V
x_2 = table2array(U(:,2))*0.001;
y_2 = table2array(U(:,4))-0.026;

V = readtable('8V_T.xlsx'); %8V
x_3 = table2array(V(:,2))*0.001;
y_3 = table2array(V(:,4))-0.026;

W = readtable('12V_T.xlsx'); %12V
x_4 = table2array(W(:,2))*0.001;
y_4 = table2array(W(:,4))-0.026;

X = readtable('16V_T.xlsx'); %16V
x_5 = table2array(X(:,2))*0.001;
y_5 = table2array(X(:,4))-0.026;



figure;
plot(x,y,x_2,y_2,x_3,y_3,x_4,y_4,x_5,y_5);
legend({'0V';'4V';'8V';'12V';'16V'})
grid on
xlabel('Displacement [mm]')
ylabel('Force [N]')
xlim([-6,6]);
ylim([-0.8,0.8]);

% Friction force per voltage (Figure 15)

close all
clear all
clc

% Increments of 4V (X-axis)
x0 = [0 4 8 12 16 20 24];
x11 = x0.';
x02 = [0 4 8 12 16];
x2 = x02.';

% Friction force average - results from figure 14 (Y-axis)
F = [0.0421 0.35470167 0.42588333 0.48576833 0.53065167 0.56663
 0.59867167]; % frictionforce 12mm iron
Fz = F.';
F2 = [0.02525 0.0274 0.0373 0.0685 0.0972 0.1157
 0.1287]; %frictionforce 12mm teflon
F22 = F2.';
F_2 = [0.0435 0.0437 0.1220 0.2053 0.2671]; %friction force 6mm iron
F_22 = F_2.';
```

```
F2_2 = [0.0251 0.0288 0.0342 0.0490 0.0500]; %friction force 6mm
 teflon
F2_22 = F2_2.';


figure

% Curve fitting
fc = fit(x11,Fz,'poly2');
plot(fc,'--b');
hold on
fc2 = fit(x11,F22,'poly2');
plot(fc2,'--b');
hold on
fc3 = fit(x2,F_22,'poly2');
plot(fc3,'--r');
hold on
fc4 = fit(x2,F2_22,'poly2');
plot(fc4,'--r');
hold on

% Result points
scatter(x11,Fz,'b');
hold on
scatter(x2,F_22,'r');
hold on
scatter(x2,F2_22,'r');
hold on
scatter(x0,F2,'b')


grid on
xlabel('Voltage [V]')
ylabel('Friction force [N]')
ylim([0, 0.7])

% Force per displacement of the 90-mm active unit cell for increments
 of 4V (figure 16)

close all
clear all
clc

% Read Excel experimental results:
T = readtable('dexter test 1 sept.9.xlsx','Range','A100:G1700'); %0V
x = table2array(T(:,4))*-1;
y = (table2array(T(:,3))*-1)+0.6;

T_1 = readtable('dexter test 1
 sept.10.xlsx','Range','A100:G1720'); %4V
x_1 = table2array(T_1(:,4))*-1;
y_1 = (table2array(T_1(:,3))*-1)+0.6;
```

```
T_2 = readtable('dexter test 1
 sept.11.xlsx','Range','A100:G1730'); %8V
x_2 = table2array(T_2(:,4))*-1;
y_2 = (table2array(T_2(:,3))*-1)+0.6;

T_3 = readtable('dexter test 1
 sept.12.xlsx','Range','A100:G1700'); %12V
x_3 = table2array(T_3(:,4))*-1;
y_3 = (table2array(T_3(:,3))*-1)+0.6;

T_4 = readtable('dexter test 1
 sept.13.xlsx','Range','A100:G1730'); %16V
x_4 = table2array(T_4(:,4))*-1;
y_4 = (table2array(T_4(:,3))*-1)+0.6;

T_5 = readtable('dexter test 1
 sept.14.xlsx','Range','A100:G1700'); %20V
x_5 = table2array(T_5(:,4))*-1;
y_5 = (table2array(T_5(:,3))*-1)+0.6;

T_6 = readtable('dexter test 1
 sept.15.xlsx','Range','A100:G1710'); %24V
x_6 = table2array(T_6(:,4))*-1;
y_6 = (table2array(T_6(:,3))*-1)+0.6;



figure;
plot(x,y,x_1,y_1,x_2,y_2,x_3,y_3,x_4,y_4,x_5,y_5,x_6,y_6);
legend({'0V','4V','8V','12V','16V','20V','24V'})
grid on
xlabel('Displacement [mm]')
ylabel('Force [N]')

% Force per displacement of the 45-mm active unit cell for increments
 of 4V (figure 17)

close all
clear all
clc

% Read Excel experimental results:
T = readtable('dexter test 8 sept.1.xlsx','Range','A300:G1150'); %0V
x = table2array(T(:,4))*-1;
y = (table2array(T(:,3))*-1)+0.06;

T_1 = readtable('dexter test 11
 sept.1.xlsx','Range','A300:G1150'); %4V
x_1 = table2array(T_1(:,4))*-1;
y_1 = (table2array(T_1(:,3))*-1)+0.06;

T_2 = readtable('dexter test 11
 sept.2.xlsx','Range','A300:G1150'); %8V
x_2 = table2array(T_2(:,4))*-1;
```

```
y_2 = (table2array(T_2(:,3))*-1)+0.06;

T_3 = readtable('dexter test 11
 sept.3.xlsx','Range','A300:G1150'); %12V
x_3 = table2array(T_3(:,4))*-1;
y_3 = (table2array(T_3(:,3))*-1)+0.06;

T_4 = readtable('dexter test 11
 sept.4.xlsx','Range','A300:G1150'); %16V
x_4 = table2array(T_4(:,4))*-1;
y_4 = (table2array(T_4(:,3))*-1)+0.06;



figure;
plot(x,y,x_1,y_1,x_2,y_2,x_3,y_3,x_4,y_4);
legend({'0','4V','8V','12V','16V'})
grid on
xlabel('Displacement [mm]')
ylabel('Force [N]')
xlim([-4,4])
ylim([-3,3])

% Damping ratio (figure 18)

close all
clear all
clc

% Increments of 4V (X-axis)
x = [0 4 8 12 16 20 24];
x00 = x.';
x_2 = [0 4 8 12 16];
xqq = x_2';

% Stored energy during compression and stretch of ±5mm - results of
 figure
% 13
S = 0.0189 + 0.0159;
% Stored energy during compression and stretch of ±2.5mm - results of
 figure
% 13
S_2 = 0.0017 + 0.0014;

% Dissipated energy 10N electromagnet during single cycle with 5mm
 deformation
D = [1.0e-3 5.5e-3 8.3e-3 9.7e-3 1.06e-2 1.13e-2 1.18e-2];
% Dissipated energy 1N electromagnet during single cycle with 2.5mm
 deformation
D_2 = [6.1287e-4 1.3e-3 2.6e-3 3.4e-3 4.1e-3];

% Damping ratio
P = D/S;
P_2 = D_2/S_2;
```

```
figure

plot(x,(P*100),'ob');
hold on
plot(x_2,(P_2*100),'or')
hold on

% Curve fitting
FF = (P*100);
FFZ = FF.';
fc = fit(x00,FFZ,'poly2');
plot(fc,'--b');
hold on
FF1 = (P_2*100);
FFZ1 = FF1.';
fc1 = fit(xqq,FFZ1,'poly2');
plot(fc1,'--r');


grid on
xlim([0,25]);
ylim([0,200]);
xlabel('Voltage [V]')
ylabel('Damping ratio \Psi [%]')

% Force per displacement of 90-mm active unit cell with increasing
 deformation velocity at 24V input (figure 19)

close all
clear all
clc

% Read Excel experimental results:
T = readtable('dexter test 4 sept.1.xlsx'); %60mm/min
x = table2array(T(:,4))*-1;
y = table2array(T(:,3))*-1;

T_2 = readtable('dexter test 1 sept.15.xlsx'); %80mm/min
x_2 = table2array(T_2(:,4))*-1;
y_2 = (table2array(T_2(:,3))*-1)+0.9;

T_3 = readtable('dexter test 4 sept.2.xlsx'); %100mm/min
x_3 = table2array(T_3(:,4))*-1;
y_3 = table2array(T_3(:,3))*-1;

T_4 = readtable('dexter test 4 sept.3.xlsx'); %120mm/min
x_4 = table2array(T_4(:,4))*-1;
y_4 = table2array(T_4(:,3))*-1;

T_5 = readtable('dexter test 4 sept.4.xlsx'); %140mm/min
x_5 = table2array(T_5(:,4))*-1;
y_5 = table2array(T_5(:,3))*-1;
```

```
figure
plot(x,y,x_2,y_2,x_3,y_3,x_4,y_4,x_5,y_5)
legend({'60mm/min','80mm/min','100mm/min','120mm/min','140mm/min'})
grid on
xlabel('Displacement [mm]')
ylabel('Force [N]')
```

Published with MATLAB® R2017b

C

Technical specifications

C.1. Electromagnets

C.1.1. 10N electromagnet

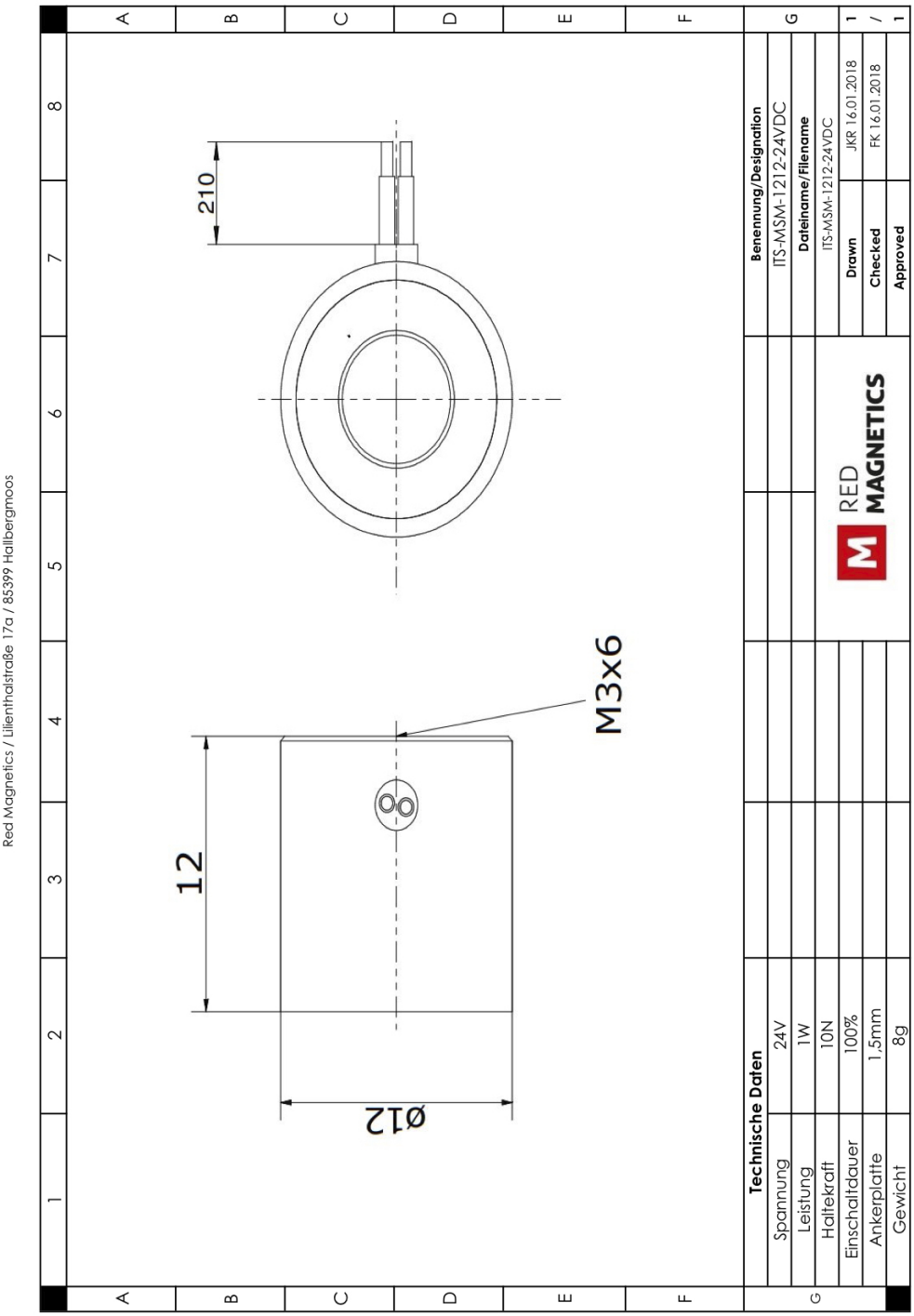

C.1.2. 1N electromagnet

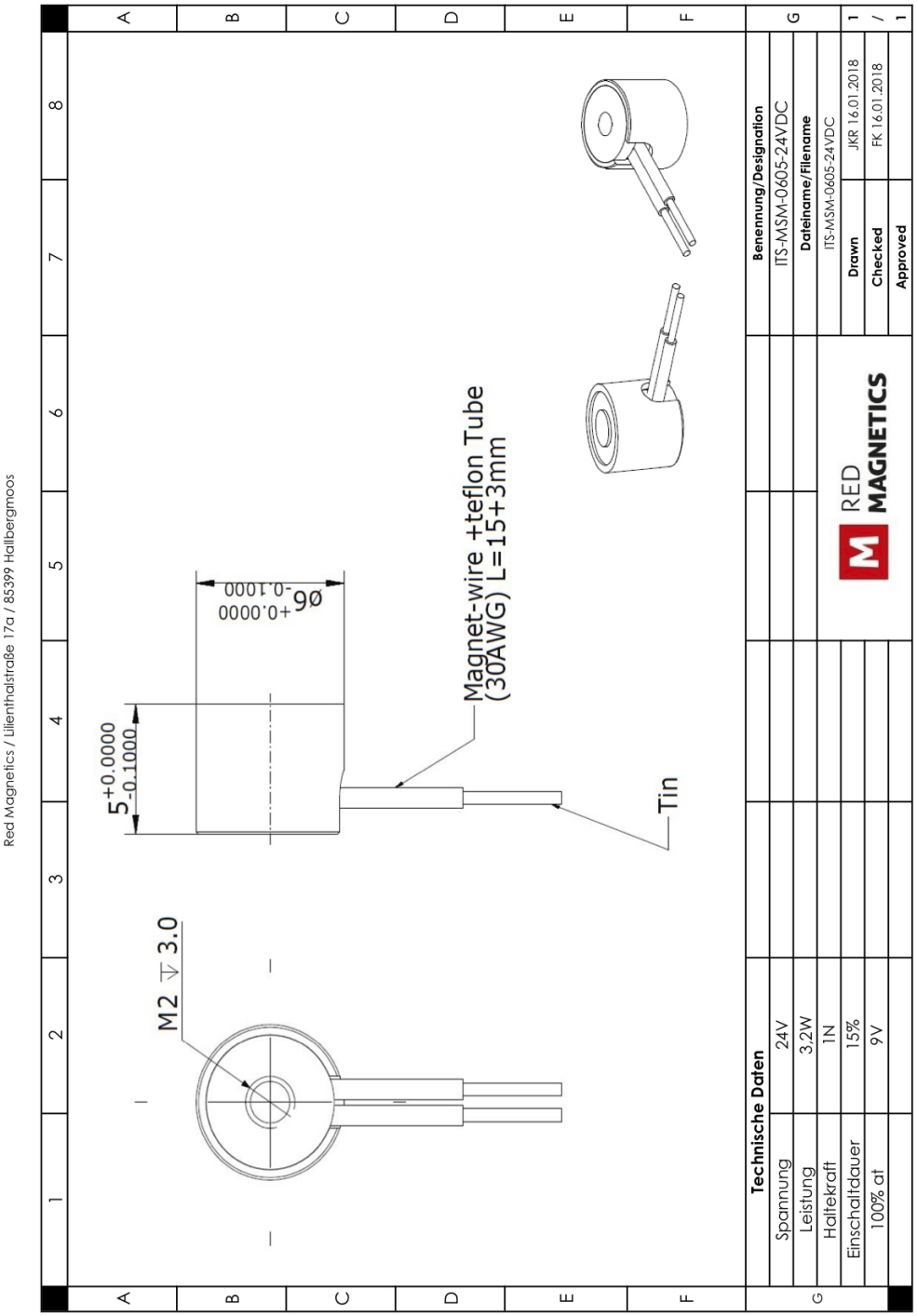

C.2. Experimental setup

C.2.1. Futek load cell

FUTEK
ADVANCED SENSOR TECHNOLOGY, INC.

MODEL LSB200
Miniature S-Beam Jr. Load Cell

FEATURES

- Up to 10 times the overload protection
- Overload is available in Tension and Compression
- Light weight
- Notable nonlinearity
- Loads up to 100 lb (445 N)
- Miniature size

Active end

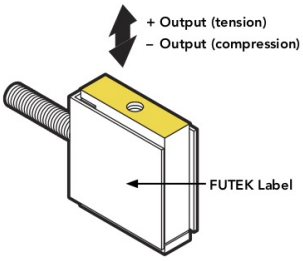

SPECIFICATIONS	
PERFORMANCE	
Nonlinearity	±0.1% of RO
Hysteresis	±0.1% of RO
Nonrepeatability	±0.05% of RO
ELECTRICAL	
Rated Output (RO)	See chart on third page
Excitation (VDC or VAC)	10 max
Bridge Resistance	See chart on third page
Insulation Resistance	≥500 MOhm @ 50 VDC
Connection	#29 AWG, 4 conductor, spiral shielded silicone cable, 5 ft [1.5 m] long
Wiring Code	WC1
MECHANICAL	
Weight (approximate)	0.3 oz [9 g]
Safe Overload	1000% of RO 200% tension only (50–100 lb)
Material	Aluminum (10 g–10 lb), stainless-steel (25–100 lb)
IP Rating	IP40
TEMPERATURE	
Operating Temperature	-60 to 200°F [-50 to 93°C]
Compensated Temperature	60 to 160°F [15 to 72°C]
Temperature Shift Zero	±0.01% of RO/°F [0.018% of RO/°C]
Temperature Shift Span	±0.02% of Load/°F [0.036% of Load/°C]
CALIBRATION	
Calibration Test Excitation	5 VDC
Calibration (standard)	5-pt Tension
Calibration (available)	Compression

Sensor Solution Source
Load · Torque · Pressure · Multi-Axis · Calibration · Instruments · Software

www.futek.com

RoHS · ANSI Z540-1 · ISO 17025 · ISO 9001 · ISO 13485 · U.S. Manufacturer

C.2.2. PI low profile translation stage

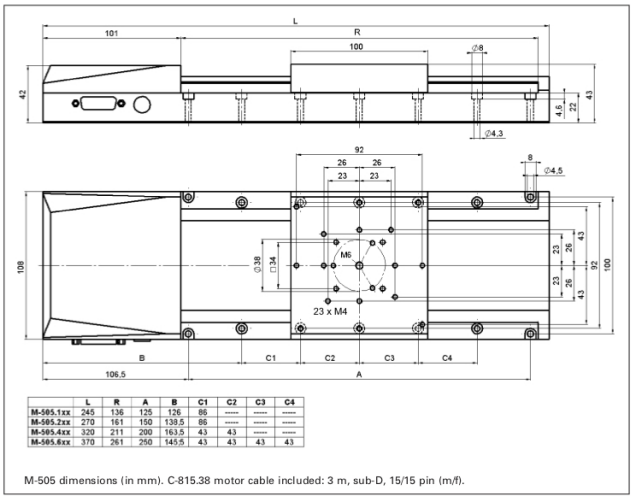

	L	R	A	B	C1	C2	C3	C4
M-505.1xx	245	136	125	126	86	-----	-----	-----
M-505.2xx	270	161	150	138.5	86	-----	-----	-----
M-505.4xx	320	211	200	163.5	43	43	-----	-----
M-505.6xx	370	261	250	145.5	43	43	43	43

M-505 dimensions (in mm). C-815.38 motor cable included: 3 m, sub-D, 15/15 pin (m/f).

Technical Data

Models	M-505.1PD	M-505.1DG	M-505.1S2	M-505.2PD	M-505.2DG	M-505.2S2	M-505.4PD	M-505.4DG	M-505.4S2	M-505.6PD	M-505.6DG	M-505.6S2	Units#
Travel range	25	25	25	50	50	50	100	100	100	150	150	150	mm
Design resolution	0.25	0.017	0.05	0.25	0.017	0.05	0.25	0.017	0.05	0.25	0.017	0.05	µm
Min. incremental	0.25	0.05	0.1	0.25	0.05	0.1	0.25	0.05	0.1	0.25	0.05	0.1	µm
Unidirectional	0.25	0.1	0.1	0.25	0.1	0.1	0.25	0.1	0.1	0.25	0.1	0.1	µm
Bidirectional	1	1	1	1	1	1	1	1	1	1	1	1	µm
Accuracy per 25 mm	1	1	1	1	1	1	1	1	1	1	1	1	µm
Straightness	1	1	1	1	1	1	1	1	1	1	1	1	µm
Flatness	1	1	1	1	1	1	1	1	1	1	1	1	µm
Pitch (θ_Y)	50	50	50	50	50	50	50	50	50	50	50	50	µrad
Yaw (θ_Z)	50	50	50	50	50	50	50	50	50	50	50	50	µrad
Max. velocity	50	3	10	50	3	10	50	3	10	50	3	10	mm/s
Max. normal	100	100	100	100	100	100	100	100	100	100	100	100	kg
Max. push/pull force	50 / 50	50 / 50	50 / 50	50 / 50	50 / 50	50 / 50	50 / 50	50 / 50	50 / 50	50 / 50	50 / 50	50 / 50	N
Max. lateral force	200	200	200	200	200	200	200	200	200	200	200	200	N
Encoder resolution	4000	2048	-	4000	2048	-	4000	2048	-	4000	2048	-	counts/rev.
Motor resolution	-	-	20,000**	-	-	20,000**	-	-	20,000**	-	-	20,000**	steps/rev.
Ballscrew pitch	1	1	1	1	1	1	1	1	1	1	1	1	mm/rev.
Gear ratio	-	(28/12)^4 :1 ≈29.6:1	-	-	(28/12)^4 :1 ≈29.6:1	-	-	(28/12)^4 :1 ≈29.6:1	-	-	(28/12)^4 :1 ≈29.6:1	-	
Nominal motor power	17*	3	- **	17*	3	- **	17*	3	- **	17*	3	- **	W
Motor voltage	24	12	24 **	24	12	24 **	24	12	24 **	24	12	24 **	V
Weight	1.5	1.5	1.5	1.8	1.8	1.8	2.5	2.5	2.5	3.2	3.2	3.2	kg
Body material	Al	Al	Al	Al	Al	Al	Al	Al	Al	Al	Al	Al	
Recommended motor controller	C-843, C-848, C-862	C-843, C-848, C-862	C-600, C-630	C-843, C-848, C-862	C-843, C-848, C-862	C-600, C-630	C-843, C-848, C-862	C-843, C-848, C-862	C-600, C-630	C-843, C-848, C-862	C-843, C-848, C-862	C-600, C-630	

* ActiveDrive™ (integrated PWM servo-amplifier), 24 V power supply included;
** 2-phase stepper, 24 V chopper voltage, max. 0.8 A / phase, 20,000 microsteps with C-600, C-630 controllers
# See page 7-106 for notes and explanations.

C.2.3. Zwick/Roell load frame

Zwick / Roell — Technical details
Materials testing machine — 1 2 3

Technical data

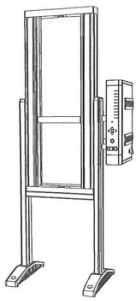

Type ..... Materials testing machine

Load frame

Test load in tensile/compression ..... 5 kN
Height:
- Load frame height ..... 1,699 mm
- with support profiles ..... 1,814 mm to 2,714 mm

Width:
- Load frame width ..... 680 mm
- with support profiles ..... 856 mm
- with electronics ..... 1,045 mm

Depth:
- Load frame depth ..... 256 mm
- with support profiles ..... 700 mm

Test area height w.o. accessories:
- Lower test area ..... 1,445 mm
- Upper test area (supplementary crosshead is necessary) ..... 1,430 mm

Test area width ..... 440 mm

Weight:
- With electronics console ..... 160 kg
- With typical accessories, approx. ..... 190 kg

Space requirements:
- Pure contact area ..... 106 cm²
- Load frame, base area ..... 5,564 cm²

Specific floor loading:
- Related to the typical accessories ..... 1.79 kg/cm²
- With 50% safety ..... 2.69 kg/cm²

Floor loading:
- Related to the typical accessories ..... 0.03 kg/cm²
- With 50% safety ..... 0.05 kg/cm²

Finish ..... RAL 7011 and RAL 7038
Ambient temperature ..... + 10 °C to + 35 °C
Humidity ..... 20 % to 90 %
Noise level ..... 67 dB(A)

Drive system

Crosshead speed ..... 0.0005 to 3,000 mm/min
Accuracy of the set speed ..... 0.03 % of V_{nom}
Drive system's travel resolution ..... 0.041 μm
Positioning, repetition accuracy (w.o. reverse of direction) ..... < 1.0 μm
Maximum test frequency ..... 0.5 Hz

C.2.4. Zwick/Roell load cell

Zwick / Roell

Zwick
Materialprüfung

Zwick GmbH & Co.KG · August-Nagel-Str. 11 · D-89079 Ulm

Kalibrierschein / *Calibration Certificate*

Kunde *Customer*	**Technische Universiteit Delft**	Ergebnisdatei *Result file*	**182823.kal**
Prüfer *Tester*	**Mohn**	Temperatur *Temperature*	**24.0 °C**
Kalibrierdatum *Date of calibration*	**22.07.2008**	AB-Nr. der Maschine *Machines AB no.*	**2152437**
Typ des Kraftaufnehmers *Type of load cell*	**KAF-TC**	Werk-Nr. der Maschine *Serial no. of the machine*	**182822**
Werk-Nr. Kraftaufnehmer *Load cells serial number*	**182823**	Anzeige *Display*	**PC**
Nennkraft *Nominal force*	**1000.000 N**	Auflösung a der Maschine *Machines resolution a*	**0.42% bei 0.2% FN**

Verwendete Gebrauchsnormale und Prüfgeräte:
Working standards and test devices used:

Belastungskörpersatz Nr.02
Digitalkompensator DK 38, Nr. 53374
Kraftaufnehmer 2kN, Nr. 102130042

Wir bestätigen hiermit, daß der oben beschriebene Kraftaufnehmer kalibriert wurde.
Die gemessenen Werte der Kraftmesseinrichtung liegen innerhalb der zulässigen Abweichungen nach DIN EN ISO 7500-1. Die jeweilige Messunsicherheit ist mit zweifacher Standardabweichung bei jeder Stufe angegeben. Die Kraftmesseinrichtung kann in den geprüften Meßbereichen wie folgt eingesetzt werden:

We hereby confirm that the above named load cell has been calibrated.
The force measurement devices measured values are within the permissilble tolerances according to DIN EN ISO 7500-1
The measuring uncertainity is given at each step considered with a double standard deviation. The force measurement device can be put to use as follows in the tested measurement ranges.

DIN EN ISO 7500-1 Klasse 1 (2.00 N ... 1.00 kN)
DIN EN ISO 7500-1 Klasse 0.5 (10.00 N ... 1.00 kN)

Für die Einhaltung der angemessenen Frist zur Wiederholung der Kalibrierung ist der Benutzer verantwortlich. Wir verweisen auf die Norm DIN 51220 und auf die speziellen Prüf- und Kalibriernormen.

The user is responsible for keeping to an appropriate deadline for the repetition of calibration.
We draw standard DIN 51220, and the special test and calibration standards to you attention

Dies ist ein elektronisch erstelltes Dokument, welches ohne Unterschrift gültig ist
This is an electronically created documnet and is therefore valid without signature.

Seite / *Page* **1/2**

Zwick GmbH & Co.KG
August-Nagel-Str. 11 · D-89079 Ulm
Registergericht Ulm HRA 1980
Telefon +49 (0)7305/10-0
Telefax +49 (0)7305/10-200
Hotline +49 (0)7305/10-225
www.zwick.de · mail: info@zwick.de

Commerzbank AG, Ulm
(BLZ 630 400 53) 9 294 109
S.W.I.F.T.-Code COBADEFF 630
IBAN DE15 6304 0053 0929 4109 00
Sparkasse Ulm (BLZ 630 500 00) 79 756
Postbank Stuttgart (BLZ 600 100 70) 6137-708
USt-IdNr: DE 147 043 343

Geschäftsführer:
Dr. Jan Stefan Roell · Michaela Ganser

pers. haftende Gesellschafterin:
Zwick Verwaltungsgesellschaft mbH, Ulm
Registergericht Ulm HRB 4361
Steuer-Nr. 88014/75003

Zwick / Roell

Zwick
Materialprüfung

Zwick GmbH & Co.KG · August-Nagel-Str. 11 · D-89079 Ulm

Ergebnisse Zug / *results tensile :*

wahrer Wert *real Value*	Maschinenanzeige *Machine display*	relative Anzeigeabweichung *rel. accuracy*	relative Wiederholpräzision *rel. repeatability*	relative Umkehrspanne *rel. reversibility*	relative Messunsicherheit rel. uncertainity
2.000 N	1.999 N	-0.05 %	0.24 %	-0.04 %	0.35 %
5.000 N	4.999 N	-0.02 %	0.05 %	-0.07 %	0.23 %
10.000 N	9.990 N	-0.10 %	0.03 %	-0.07 %	0.21 %
20.000 N	20.006 N	0.03 %	0.03 %	-0.02 %	0.20 %
50.000 N	50.015 N	0.03 %	0.01 %	-0.01 %	0.20 %
100.000 N	100.040 N	0.04 %	0.01 %	0.00 %	0.20 %
99.907 N	100.000 N	0.09 %	0.28 %	-0.39 %	0.20 %
199.980 N	200.000 N	0.01 %	0.39 %	-0.02 %	0.26 %
400.200 N	400.000 N	-0.05 %	0.09 %	0.06 %	0.12 %
599.920 N	600.000 N	0.01 %	0.02 %	0.03 %	0.12 %
799.830 N	800.000 N	0.02 %	0.09 %	-0.07 %	0.12 %
1.000 kN	1.000 kN	-0.01 %	0.07 %	-0.01 %	0.12 %

Ergebnisse Druck / *results compression :*

wahrer Wert *real Value*	Maschinenanzeige *Machine display*	relative Anzeigeabweichung *rel. accuracy*	relative Wiederholpräzision *rel. repeatability*	relative Umkehrspanne *rel. reversibility*	relative Messunsicherheit rel. uncertainity
2.000 N	2.004 N	0.21 %	0.33 %	-0.53 %	0.37 %
5.000 N	5.005 N	0.11 %	0.18 %	-0.18 %	0.25 %
10.000 N	10.009 N	0.09 %	0.06 %	-0.09 %	0.21 %
20.000 N	20.029 N	0.14 %	0.06 %	-0.03 %	0.21 %
50.000 N	50.023 N	0.05 %	0.04 %	0.01 %	0.20 %
100.000 N	100.020 N	0.02 %	0.02 %	0.01 %	0.20 %
100.400 N	100.000 N	-0.40 %	0.40 %	-0.06 %	0.27 %
200.180 N	200.000 N	-0.09 %	0.25 %	0.04 %	0.17 %
400.250 N	400.000 N	-0.06 %	0.11 %	0.10 %	0.12 %
600.040 N	600.000 N	-0.01 %	0.07 %	0.10 %	0.12 %
800.540 N	800.000 N	-0.07 %	0.01 %	-0.03 %	0.12 %
999.900 N	1.000 kN	0.01 %	0.04 %	0.05 %	0.12 %

Ergebnisdatei *Result file* **182823.kal**

Seite *Page* **2/2**

Zwick GmbH & Co.KG
August-Nagel-Str. 11 · D-89079 Ulm
Registergericht Ulm HRA 1980
Telefon +49 (0)7305/10-0
Telefax +49 (0)7305/10-200
Hotline +49 (0)7305/10-225
www.zwick.de · mail: info@zwick.de

Commerzbank AG, Ulm
(BLZ 630 400 53) 9 294 109
S.W.I.F.T.-Code COBADEFF 630
IBAN DE15 6304 0053 0929 4109 00
Sparkasse Ulm (BLZ 630 500 00) 79 756
Postbank Stuttgart (BLZ 600 100 70) 6137-708
USt-IdNr: DE 147043343

Geschäftsführer:
Dr. Jan Stefan Roell · Michaela Ganser

pers. haftende Gesellschafterin:
Zwick Verwaltungsgesellschaft mbH, Ulm
Registergericht Ulm HRB 4361
Steuer-Nr. 88014/75003

Bibliography

[1] Johan Christensen, Muamer Kadic, Oliver Kraft, and Martin Wegener. Vibrant times for mechanical metamaterials. *MRS Communications*, 5(3):453–462, 2015. doi: 10.1557/mrc.2015.51.

[2] Ken Evans and Andrew Alderson. Auxetic materials: Functional materials and structures from lateral thinking! *Advanced Materials - ADVAN MATER*, 12:617–628, 05 2000. doi: 10.1002/(SICI)1521-4095(200005)12:93.0.CO;2-3.

[3] Babak Haghpanah, Hamid Ebrahimi, Davood Mousanezhad, Jonathan Hopkins, and Ashkan Vaziri. Programmable elastic metamaterials. *Advanced Engineering Materials*, 18:n/a–n/a, 10 2015. doi: 10.1002/adem.201500295.

[4] Muamer Kadic, Tiemo Bückmann, Nicolas Stenger, Michael Thiel, and Martin Wegener. On the practicability of pentamode mechanical metamaterials. *Applied Physics Letters*, 100(19):191901, 2012. doi: 10.1063/1.4709436. URL `https://doi.org/10.1063/1.4709436`.

[5] Roy Kornbluh, Harsha Prahlad, Ron Pelrine, Scott Stanford, Marcus Rosenthal, and Philip Guggenberg. Rubber to rigid, clamped to undamped: Toward composite materials with wide-range controllable stiffness and damping. *Proceedings of SPIE - The International Society for Optical Engineering*, 5388, 07 2004. doi: 10.1117/12.548971.

[6] Suyi Li and Kon-Well Wang. Fluidic origami: A plant-inspired adaptive structure with shape morphing and stiffness tuning. *Smart Materials and Structures*, 24, 10 2015. doi: 10.1088/0964-1726/24/10/105031.

[7] Zachary Nicolaou and Adilson Motter. Mechanical metamaterials with negative compressibility transitions. *Nature materials*, 11:608–13, 05 2012. doi: 10.1038/nmat3331.

[8] Johannes Overvelde, Twan de Jong, Yanina Shevchenko, Sergio Becerra, George Whitesides, James Weaver, Chuck Hoberman, and Katia Bertoldi. A three-dimensional actuated origami-inspired transformable metamaterial with multiple degrees of freedom. *Nature Communications*, 7, 03 2016. doi: 10.1038/ncomms10929.

[9] Ryan Poon and Jonathan B. Hopkins. Phase-changing metamaterial capable of variable stiffness and shape morphing. *Advanced Engineering Materials*, 21:1900802, 2019.

[10] Xianglong Yu, Ji Zhou, Haiyi Liang, and Lingling Wu. Mechanical metamaterials associated with stiffness, rigidity and compressibility: A brief review. *Progress in Materials Science*, 94, 12 2017. doi: 10.1016/j.pmatsci.2017.12.003.

[11] Amir A. Zadpoor. Mechanical meta-materials. *Mater. Horiz.*, 3:371–381, 2016. doi: 10.1039/C6MH00065G. URL `http://dx.doi.org/10.1039/C6MH00065G`.